

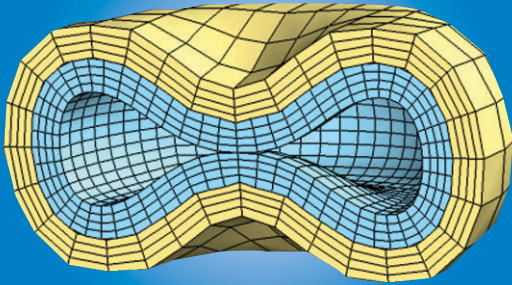
FY03

UCRL-TR-203694

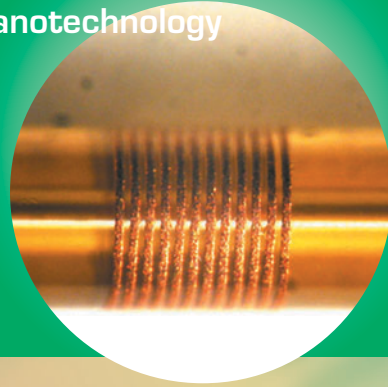
Engineering Technology Reports

Technology Base

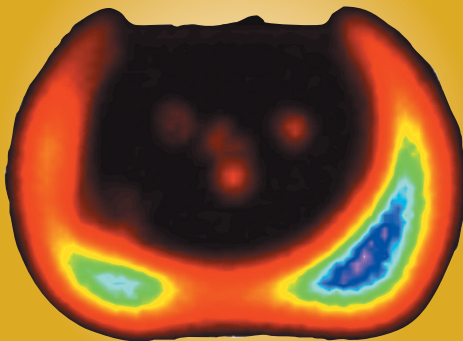
Computational Engineering



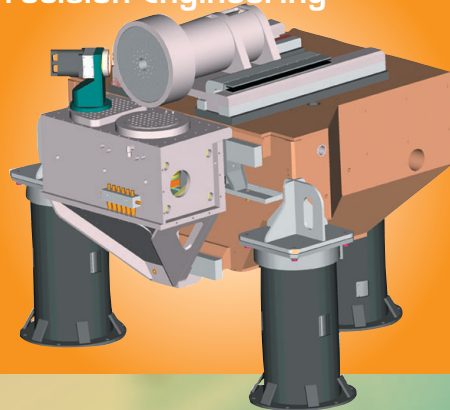
Microtechnology and Nanotechnology



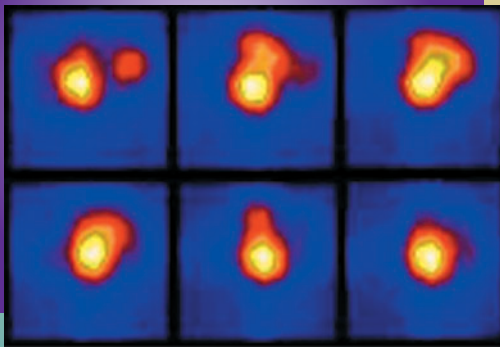
Nondestructive Characterization



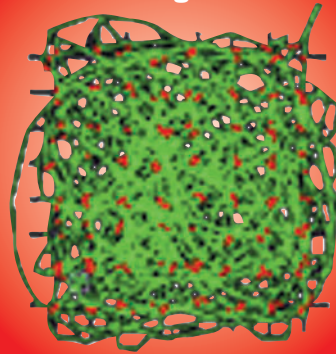
Precision Engineering

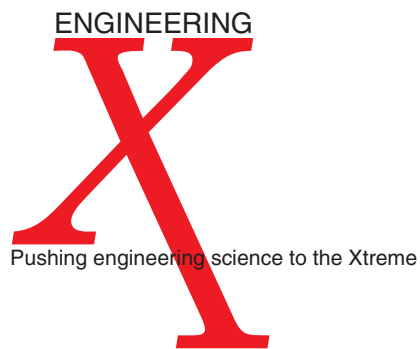


Complex Distributed Systems



Other Technologies





Acknowledgments

Scientific Editing

Camille Minichino

Graphic Design

Irene J. Chan

Art Production/Layout

Jeffrey Bonivert

Debbie A. Marsh

Kathy J. McCullough

Cover:

Graphics representing technology-base projects from Engineering's five Centers and other technologies.

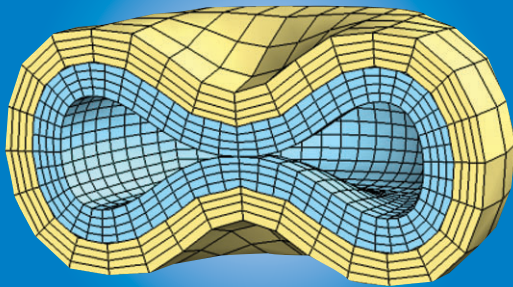
FY03

UCRL-TR-203694

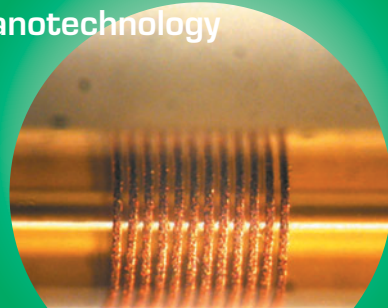
Engineering Technology Reports

Technology Base

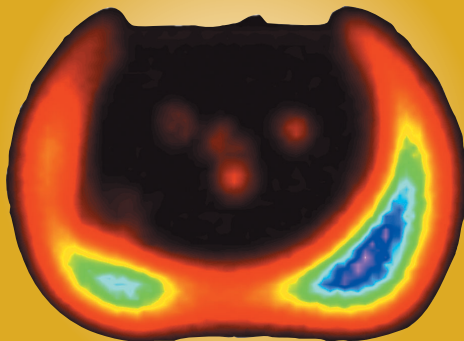
Computational Engineering



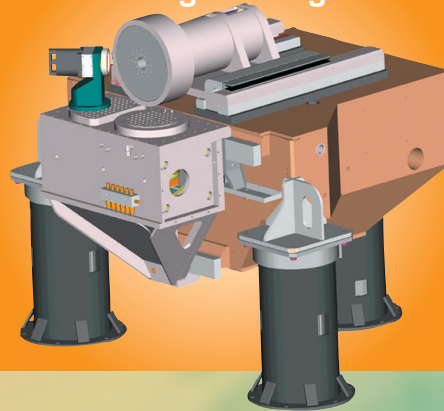
**Microtechnology and
Nanotechnology**



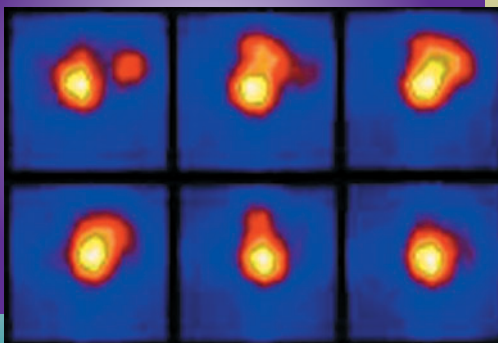
Nondestructive Characterization



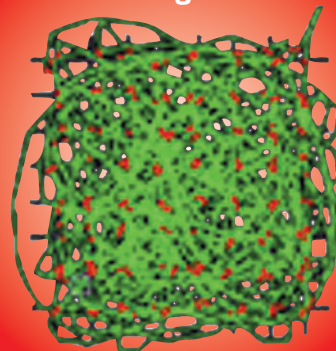
Precision Engineering



**Complex Distributed
Systems**



Other Technologies



Introduction

Steven R. Patterson	v
---------------------	---

Center for Computational Engineering

Capability Enhancements in NIKE3D

M. A. Puso	3
------------	---

Continuum-Mechanics-Based Simulations of Biomolecules

C. L. Lee; N. C. Perkins, S. Goel [University of Michigan]	4
--	---

E3D Modifications

D. H. Chambers, K. A. Fisher, S. K. Lehman, G. H. Thomas, S. C. Larsen	5
--	---

Electromagnetic Modeling of Voids in Quartz

D. Steich, J. B. Javedani, G. J. Burke	6
--	---

EM Code Characterization for Accelerator Experiments and Lightning Safety Assessments

C. G. Brown, Jr., J. B. Javedani, M. M. Ong, G. E. Vogtlin	7
--	---

Engineering Visualization Theatre

M. D. Loomis, R. M. Sharpe	8
----------------------------	---

Enhanced General Purpose Fluid Dynamics Modeling Capability

K. Salari, J. M. Ortega	9
-------------------------	---

Enrichment of Output Database and New Capabilities for DYN3D

J. I. Lin, E. Zywickz	10
-----------------------	----

MEMS Models for Microscale Fuel Cells

M. A. Havstad, J. D. Morse	11
----------------------------	----

Post-Processing and Data Management Enhancements

D. E. Speck, E. M. Pierce	12
---------------------------	----

RF Component Toolbox Using Microwave Studio

B. Rusnak	13
-----------	----

Sensitivity Analysis

G. A. Loosmore, L. G. Glascoe, H. Hsieh	14
---	----

Software Interface for a Parallel Solver Library

N. J. Champagne, M. L. Stowell	15
--------------------------------	----

Thermal Code Enhancements

M. A. Havstad	16
---------------	----

Verification and Validation Framework for Scientific Codes

K. Salari	17
-----------	----

Center for Microtechnology and Nanotechnology

Application of Modeling Tools to Photonic Devices for High-Bandwidth Diagnostics

T. C. Bond, J. S. Kallman, K. D. Akkerman21

Biological Pathogen Extraction from Raw Water Sources Using Dielectrophoretic Forces

R. R. Miles, K. A. Bettencourt, J. J. Crawford22

Contact-Stress, Deflection, and Strain MEMS Sensors

J. Kotovsky, S. P. Swierkowski23

Direct Bonding of Gallium Arsenide to Sapphire

G. A. Cooper, N. F. Raley, V. R. Sperry, J. J. Muiyco24

Image Processing for Analysis of Microfluidic Systems and Biological Assays

T. H. Weisgraber25

Multichannel Fiber-Optic Processor/Multiplexer

M. D. Pocha, C. F. McConaghy, G. A. Meyer, J. D. Wolfe, T. Laviates26

Nanoelectrodes for Electrochemical Detection of Biological Pathogens

D. A. Sopchak27

Nano-Mechanical Characterization Tools for *In-Situ* Deformation and Morphology of Materials

S. E. Groves, M. W. McElfresh, S. K. McCall28

Polymer-Based Manufacturing Processes for Hybrid Integrated Microsystems

J. C. Davidson, P. Krulevitch, M. Maghribi, J. Hamilton29

Temperature Gradient Focusing

E. K. Wheeler, K. D. Ness30

Three-Dimensional Microlithography System

V. Malba, A. F. Bernhardt, L. B. Evans, C. D. Harvey31

X-Ray Cathode Detector

J. D. Morse, K. Lui, D. R. Ciarlo, H. E. Petersen32

Center for Nondestructive Characterization

Coupling of Nondestructive Evaluation and Finite-Element Analysis for Numerical Analysis

E. J. Kokko, D. J. Chinn, H. E. Martz, R. M. Sharpe, D. H. Chambers, S. J. DeTeresa35

Enhanced Capability for Sonic IR NDE

W. O. Miller, M. W. Burke, G. H. Thomas36

Mesoscale Metrology and Characterization Reference Standards

R. L. Hibbard, M. J. Bono, A. M. Waters, H. E. Martz37

Nondestructive Characterization of Ceramic Processing Defects

D. J. Chinn, C. M. Logan38

Optimization of Photothermal NDE System	
R. D. Huber, D. J. Chinn, C. J. Stolz, C. L. Weinzapfel	39
Synchrotron Microtomography at ALS	
K. W. Dolan, D. Haupt, J. H. Kinney, D. J. Schneberk, T. Smith	40
Three-Dimensional Rendering of High-Frequency Ultrasonic Data	
S. E. Benson, G. H. Thomas	41
Center for Precision Engineering	
Active Vibration Isolation of an Unbalanced Machine Spindle	
D. J. Hopkins, P. Geraghty	45
Digital Synchronous Demodulation and Conditioning for Precision Sensors	
D. J. Hopkins	46
MRF Technology for Non-Glass Applications	
J. L. Klingmann, W. F. Brocius	47
Servo System Machine Tool Control Analysis	
D. J. Hopkins, G. F. Weinert, T. A. Wulff	48
Surface Acoustic Wave Motors	
S. L. Hunter, K. Carlisle	49
Ultra-Precision Machine Spindle Using Porous Ceramic Bearings	
P. Geraghty, K. Carlisle, L. C. Hale	50
Center for Complex Distributed Systems	
Automated Sentinel	
V. N. Kohlhepp, S. D. Freeman	53
Communication and Ranging for Node Localization	
F. U. Dowl, C. A. Kent	54
Distributed Control System	
L. M. Flath	55
Energy Infrastructure Vulnerability Assessment and Response	
J. S. Stewart, A. M. Smith, S. Sengupta, L. E. Clarke; D. Price (PG&E)	56
Field-Programmable Gate Array Chip	
E. D. Jones	57
Radar Vision	
K. Romero, G. E. Dallum, J. E. Hernandez, J. M. Zumstein	58
Real-Time Speckle Imaging for Video Surveillance	
C. Carrano, D. A. Silva	59

Regional Simulation of Ground Motion and Building Response	
M. A. Gerhard	60
Scene-Based Wavefront Sensing for Diverse Applications	
L. A. Poyneer, K. N. LaFortune, B. J. Bauman, C. W. Chan	61
Vibration-Signature-Based Modeling and Simulation	
R. E. Glaser, C. L. Lee, W. G. Hanley	62
Wideband Antenna Arrays for Electronic Countermeasure	
A. Spiridon, F. U. Dowl	63
Other Technologies	
Dynamic Fracture Mechanics Experiments	
S. J. DeTeresa, C. K. Syn, G. J. Larsen	67
High-Speed Digital Transmitter	
B. N. Tran, H. Pao, R. J. Kane	68
Model-Based Inspection	
P. E. Ahre, C. C. Garrett	69
Passive Tracking of Flight Vehicles Using Telemetry-Signal External	
M. R. Portnoff, R. J. Kane	70
RF Telemetry Processing Using Software-Defined Radio Approaches	
R. J. Kane	71
System Architecture for High-Speed Transient Diagnostics	
G. P. Le Sage, B. N. Tran; E. P. Daykin, G. Perryman, C. Perez, R. Eichholz [Bechtel Nevada]	72
Author Index	
	75

Introduction

Steven R. Patterson, Associate Director for Engineering

This report summarizes the science and technology research and development efforts in Lawrence Livermore National Laboratory's Engineering Directorate for FY2003, and exemplifies Engineering's 50-year history of researching and developing the engineering technologies needed to support the Laboratory's missions. Engineering has been a partner in every major program and project at the Laboratory throughout its existence, and has prepared for this role with a skilled workforce and the technical resources developed through venues like the Laboratory Directed Research and Development Program (LDRD). This accomplishment is well summarized by Engineering's mission: "Enable program success today and ensure the Laboratory's vitality tomorrow."

Engineering's investment in technologies is carried out through two programs, the LDRD program and the "Tech Base" program.

LDRD is the vehicle for creating those technologies and competencies that are cutting edge, or that require a significant level of research, or contain some unknown that needs to be fully understood. Tech Base is used to apply those technologies, or adapt them to a Laboratory need. The term commonly used for Tech Base projects is "reduction to practice."

Technology-base projects help bring about the natural transition to reduction-to-practice of scientific or engineering methods that are well understood and established. They represent discipline-oriented, core competency activities that are multi-programmatic in application, nature, and scope.

This volume of Engineering Technical Reports summarizes progress on the projects funded for technology-base efforts in FY2003. Objectives of technology-base funding include:

- the development and enhancement of tools and processes to provide Engineering support capability, such as code maintenance and improved fabrication methods;
- support of Engineering science and technology infrastructure, such as the installation or integration of a new capability;
- the initial scoping and exploration of selected technology areas with high strategic potential, such as assessment of university, laboratory, and industrial partnerships.

Engineering's five Centers, in partnership with the Division Leaders and Department Heads, focus and guide longer-term investments within Engineering. The Centers attract and retain top staff, develop and maintain critical core technologies, and enable programs. Through their technology-base projects, they oversee the application of known engineering approaches and techniques to scientific and technical problems. The Centers and their Directors are as follows:

Center for Computational Engineering:

Robert M. Sharpe

Center for Microtechnology and Nanotechnology:

Raymond P. Mariella, Jr.

Center for Nondestructive Characterization:

Harry E. Martz, Jr.

Center for Precision Engineering:

Keith Carlisle

Center for Complex Distributed Systems:

Donald Meeker (Acting Director)

FY2003 Center Highlights

The **Center for Computational Engineering** orchestrates the research, development and deployment of software technologies to aid in many facets of LLNL's engineering mission. Computational engineering has become a ubiquitous component throughout the engineering discipline. Current activities range from tools to design the next generation of mixed-signal chips (systems on a chip) to full-scale analysis of key DOE and DoD systems.

Highlights of the Center's technology-base projects for FY2003 include enhancements, verification, and validation of engineering simulation tools and capabilities; progress in visualization and data management tools; and updates in parallel interface algorithms. The Center has offered a real-world computing capability that opens the door to solving a wide variety of fluid/solid interaction problems in transportation, aerospace, and infrastructure settings.

The mission of the **Center for Microtechnology and Nanotechnology** is to invent, develop, and apply micro- and nanotechnologies to support LLNL missions in Stockpile Stewardship, Homeland Security, Nonproliferation, and other programs. The Center's capabilities cover materials, devices, instruments, and systems that require microfabricated components, including microelectromechanical systems (MEMS), electronics, photonics, microstructures, and microactuators. Center staff have achieved considerable national recognition for the successes demonstrated in Chem-Bio National Security Program instrumentation, supported by the DOE and the Defense Intelligence Agency.

Our FY2003 projects include the application of modeling tools to photonic devices; characterization tools for *in-situ* deformation and morphology of materials; polymer-based manufacturing processes; advances in detectors and sensors; pathogen extraction for water security; and advances in image processing.

The **Center for Nondestructive Characterization** advances, develops and applies nondestructive characterization (NDC) measurement technology to significantly impact the manner in which LLNL inspects, and through this, designs, fabricates, and refurbishes systems and

components. The Center plays a strategic and vital role in the reduction-to-practice of scientific and engineering NDC technologies, such as electromagnetic waves (infrared, microwave, visible and x rays), acoustics, and particles (*e.g.*, protons) for imaging, to allow Engineering in the near-term to incorporate these technologies into LLNL and DOE programs.

This year's technology-base projects include optimization of a photothermal NDE system; enhancements in infrared techniques and synchrotron microtomography capability; mesoscale metrology; 3-D rendering of high-frequency ultrasonic data; advances in numerical analysis; and ceramic NDC.

The Center for Precision Engineering advances LLNL's high-precision capabilities in manufacturing, dimensional metrology and assembly, to meet the future needs of LLNL and DOE programs. Precision engineering is a multi-disciplinary systems approach to achieve an order of magnitude greater accuracy than currently achievable. The Center's core technologies are essential to the Laboratory because they will reduce the amount of research and development required to build the next generation of instruments and machine tools. By using proven technology, they also reduce the risk, the lead and design times, and the time to complete.

Highlights for Precision Engineering's FY2003 technology-base projects include advances in machine spindle dynamics, precision sensors; and surface acoustic wave motors.

The Center for Complex Distributed Systems exploits emerging information technologies to develop unique communications related to data gathering, advanced signal processing, and new methodologies for assimilating measured data with computational models in data-constrained simulations of large systems. These technology-base projects are delivering application-ready tools into the hands of engineers supporting programs, and thus serve a critical link in transitioning from research to practice.

Current technology-base activities include: vibration-signature-based modeling and simulation; communication and ranging for node localization; continuum-mechanics-based and ground motion simulations; vulnerability assessment and response; wideband antenna arrays for counter-measure; radar vision; high-resolution video surveillance; and scene-based wavefront sensing.

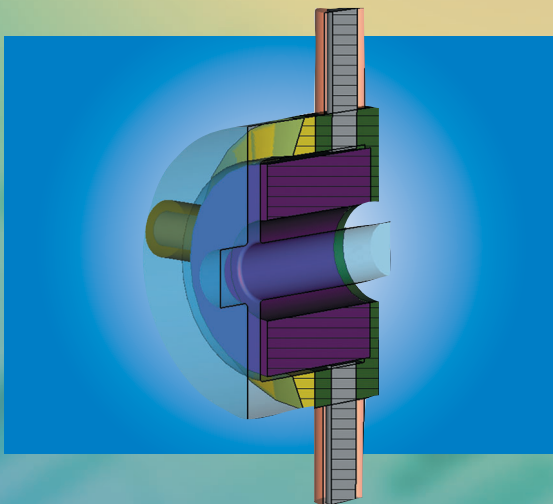
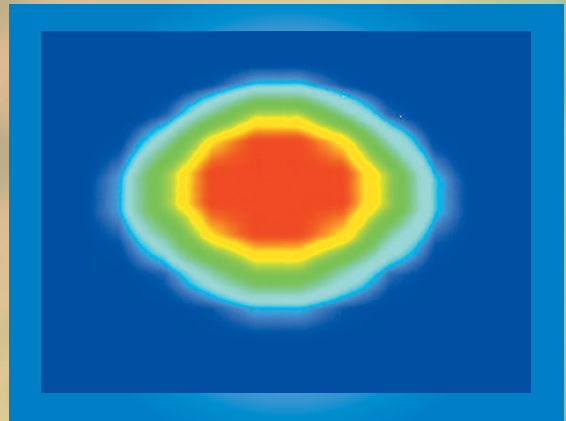
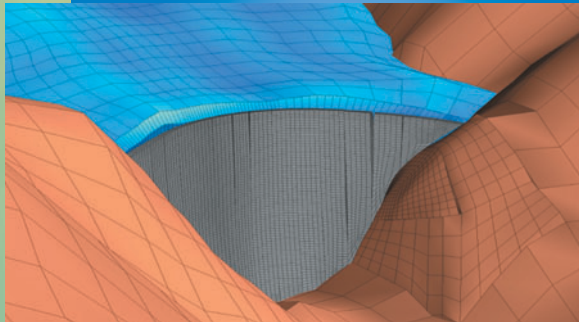
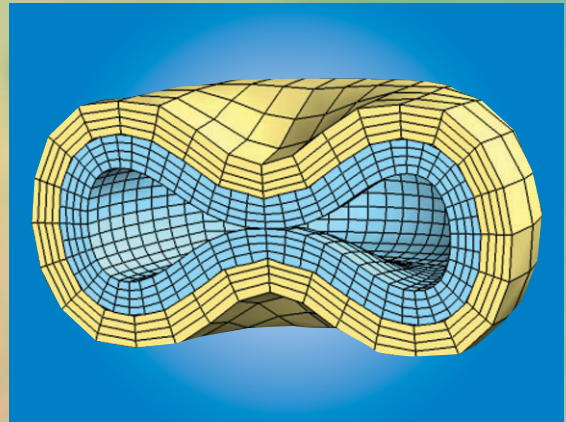
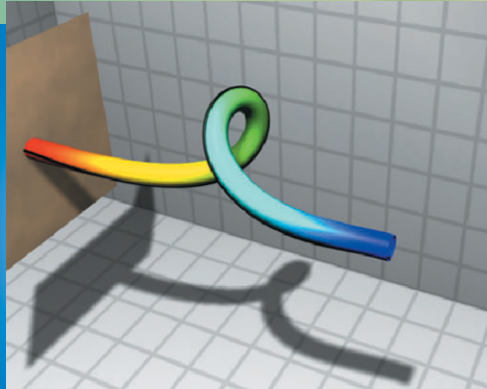
In FY2003, **other technologies** also contributed to Engineering's progress in telemetry, high-speed transient diagnostics, and model-based inspection.

Science-Based Engineering

Our five Centers develop the key engineering technologies that make Laboratory programs successful. They provide the mechanism by which Engineering can help programs attract funding, while pioneering the technologies that will sustain long-term investment.

Our Centers, with staff who are full partners in Laboratory programs, integrate the best of mechanical and electronics engineering, creating a synergy that aids Engineering's mission, and helps turn the impossible into the doable.

Center for Computational Engineering



Laser slab distortions are analyzed using the codes TOPAZ3D, NIKE3D, and OPL. For example, nonuniformity in the prompt heating generates temperature gradients that warp the laser slab and affect beam quality during the laser pulse [see Fig. 1]. This is primarily a dynamic linear elastic mechanical response that is run most efficiently using a direct linear solver.

Laser analysts needed a 64-bit version of NIKE3D on their HP workstations to accommodate the large memory sizes the direct solver demanded. Although 64-bit versions of NIKE3D were available for other platforms, they were not fully standard, and did not work on the HP. A 64-bit HP version was produced that ran three to four times faster with direct solvers than the 32-bit version using an iterative preconditioned conjugate gradient (PCG) solver.

Surface pressures are a form of follower force because their orientation remains normal to the surface

Capability Enhancements in NIKE3D

M. A. Puso

In FY03 we added features to NIKE3D to improve robustness and efficiency in support of multiple applications: a 64-bit version for the coupled NIKE/TOPAZ/OPL codes, the exact linearization of follower-type forces, and a mesh relaxation capability for contact surfaces.

throughout a body's deformation. Thus, they are nonlinear and at times need to be exactly linearized in a Newton-Raphson iteration scheme to achieve convergence. This linearization creates a nonsymmetric stiffness matrix, which increases the memory and time needed for equation solving, but can speed overall performance. For example, the internally-pressurized sphere in Fig. 2 is crushed by a rigid wall. The greatly changing orientation of internal surface pressure required the new pressure linearization to successfully complete the analysis. The analysis simply failed to converge without this new option. This feature was added to aid the convergence of inflatable structure analyses for a defense application.

Using different mesh densities (element sizes) on opposing sides of the same surface definition can lead to material overlaps in the computational model. Nodal relocation at contact interfaces is then required during initialization of a simulation to eliminate these non-physical surface penetrations.

The techniques used can at times move nodes too far and severely distort elements. In this event, some form of mesh relaxation must be made to accommodate the nodal relocation. The relaxation simultaneously repositions multiple nodes in the vicinity of the penetration and thus prevents excessive distortion in any one element. Such relaxation can now be done during the restart phase of NIKE3D. For example, modeling of the Morrow Point dam required the fluid to be in contact with the lakebed. Direct nodal relocation of fluid nodes caused inversion and failure of the simulation. By applying mesh relaxation to the fluid, the nodes could be relocated successfully without large element distortions.

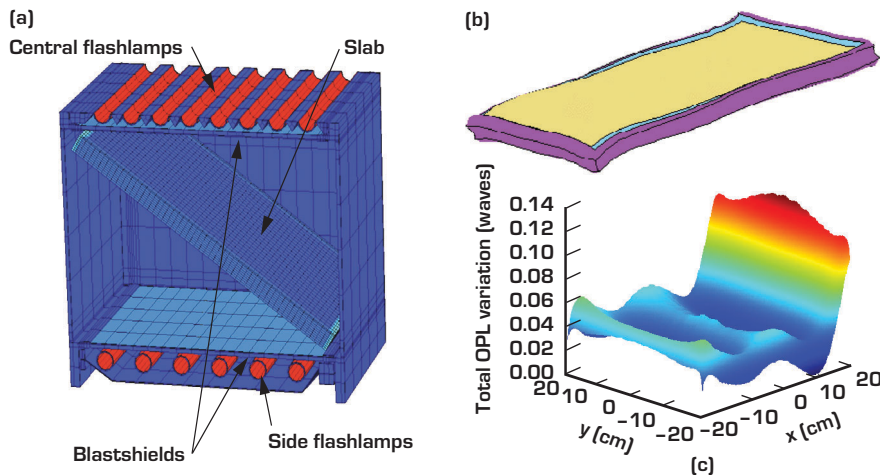


Figure 1. (a) NIKE3D-TOPAZ3D model of amplifier with components. (b) NIKE3D predicted slab deformation. (c) Resulting optical wavefront distortion predicted by OPL.

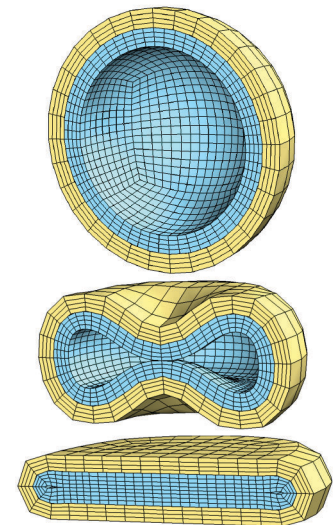


Figure 2. Crushing of pressurized sphere.

The behavior of biomolecules, such as DNA or proteins, is closely related to the dynamics of their physical configurations. Changes in configuration occur over the length of the molecule and on millisecond [or longer] time scales. It is difficult to model such processes with atomistic simulation techniques because of the computational cost arising from including the large number of atoms (possibly greater than 1 million), even for relatively small molecules. We are therefore looking to apply continuum-mechanics-based methods that can capture deformation behavior on these length and time scales. The idea is to apply traditional structural mechanics theories used to model systems from micro-devices to buildings.

Some biomolecules are relatively simple polymers existing in a fluid environment, with a structural appearance

Continuum-Mechanics-Based Simulations of Biomolecules

C. L. Lee; N. C. Perkins, S. Goel (University of Michigan)

The goal of this project is to produce continuum-mechanics-based computational tools to simulate the dynamic behavior and predict the physical configuration of biomolecules on long (whole molecule) length scales and long (millisecond deformation) time scales.

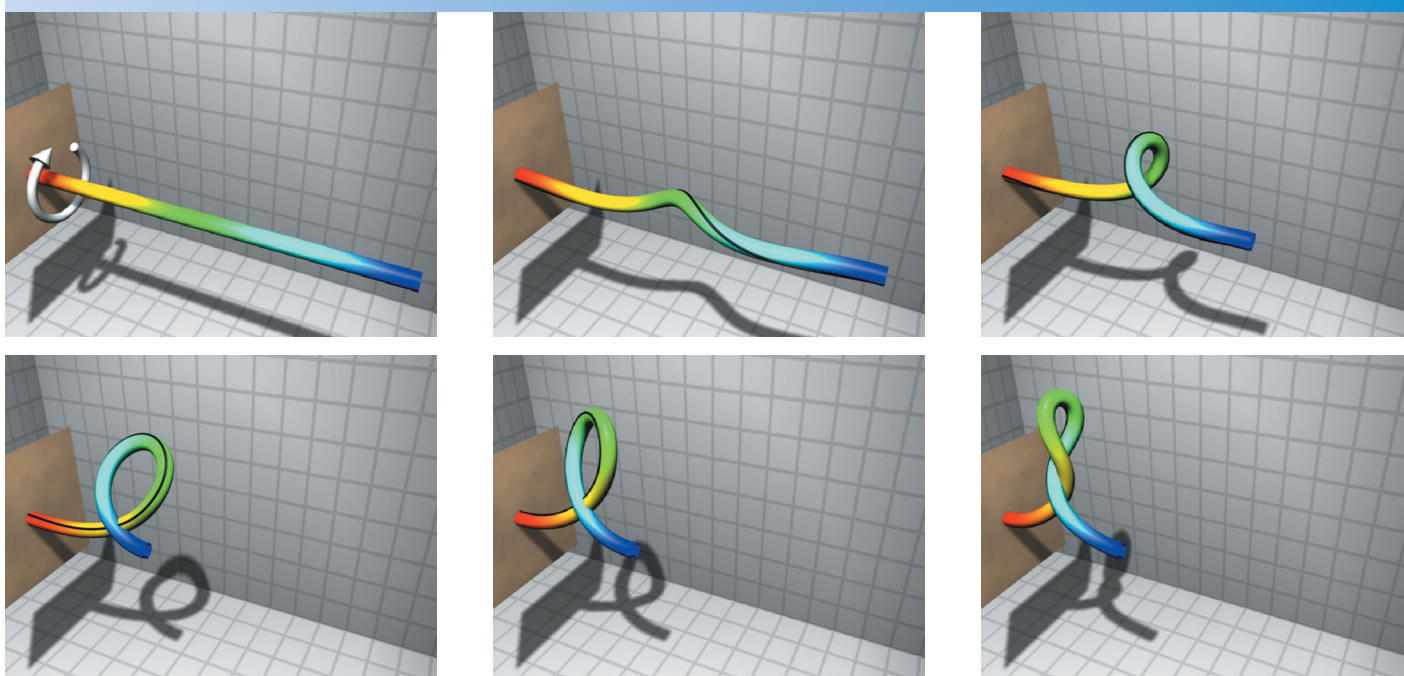
similar to that of a helical spring. In the macro world, these are the same structural features found in submerged elastic cables used in marine applications. With this as our starting point, we are adapting and modifying numerical models of marine cable for simulating three-dimensional motion of long-chain biomolecules undergoing arbitrary large deformation.

The cable model is based on Kirchhoff rod theory that is discretized with a finite-difference formulation using the generalized-alpha method in both space and time. The kinematics of the cross-section

is described using an incremental rotation vector. The model accounts for fluid-structure interactions by added fluid mass and fluid drag, and allows for structural self-contact. The framework is available to include body forces such as electrostatic interactions and Brownian motion forces.

We have implemented an initial demonstration in which a “cable” segment dynamically buckles into a helix that subsequently collapses into a looped form [see figure]. This behavior is known to exist for supercoiled DNA and arises from the conversion of torsional strain energy to bending strain energy.

In future work, we will continue to enhance the numerical simulation capability, and also measure material properties and validate the model through experiments performed with a laser optical trap.



Single time frames from dynamic simulation. An initially straight cable segment is allowed to twist at the left end. All other degrees of freedom are fixed. The right end is constrained to slide along the segment axis. As the imposed twist increases, the cable segment undergoes nonlinear torsional buckling and forms a loop.

E3D is an elastic wave simulation code used for prototyping and optimizing methods for acoustic imaging and detection. Typical applications include prototyping of acoustic inspection systems for optics (see figure); simulating acoustic imaging in tissue; and issues in acoustic tomography methods, buried waste imaging systems, and potting void detection. Future applications include acoustic inspection systems for target characterization and investigation of methods for detecting flaws in layered media.

The original code was written for seismic applications and later adapted for NDE applications. This technology-base project consolidates the many versions of E3D and optimizes the code for engineering applications. This includes building a front-end graphical user interface (GUI) to enable a larger number of engineers to use the code. In addition, a users guide will be created for the NDE version with examples and validations with experimental data.

The two year project includes building a preprocessor, modifying the kernel, and creating post-processing tools, with the preprocessor requiring the greatest amount of effort. Features desired for each part were listed and prioritized (see table).


The preprocessor consists of two components: a GUI, and a script generation tool. For FY03 a specification document was written for these components; the script generation tool was completed; and an initial version of the GUI was constructed. Numerical models for ultrasonic transducers (transmitters and receivers) used in NDE were formulated and incorporated into the preprocessor. Experiments to validate the transducer models were performed and are continuing for each class of transducer used for NDE.

E3D Modifications

D. H. Chambers, K. A. Fisher, S. K. Lehman,
G. H. Thomas, S. C. Larsen

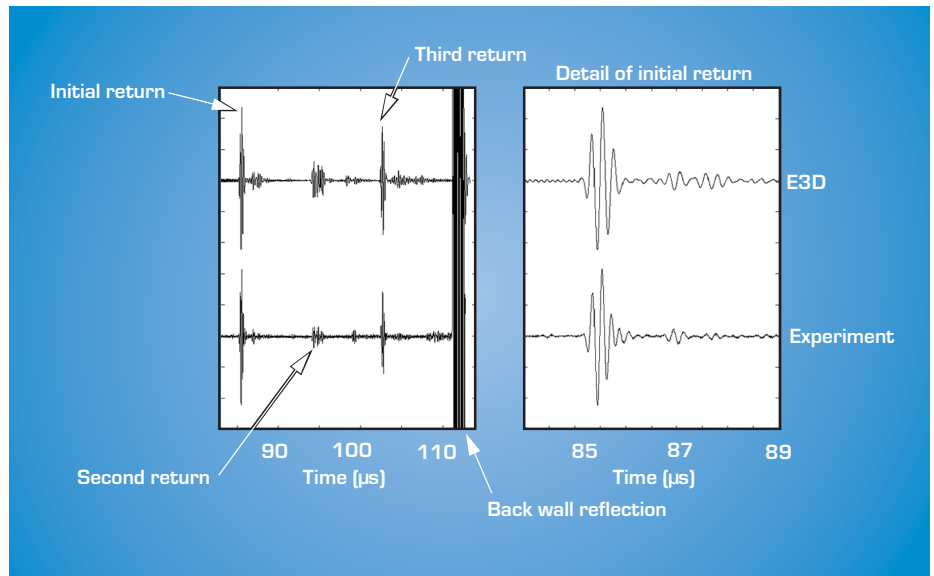
New users who obtain the E3D seismic source code must typically edit the code to adapt it for their specific application. Over the years several versions of the code have been created with various undocumented features. This two-year technology-base project consolidates these versions and optimizes the code for engineering applications.

A visualization method for post-processing tomographic data was investigated, but further work was deferred

processor to visualize the output, completion of documentation, and validation with simple experiments. 

Prioritized feature list.

	Preprocessor	Kernel	Postprocessor
1	Standard NDE axes GUI setup interface Object builder Input pulse builder	Free surface bc Spatially mixed bc's Nonreflecting bc Elastic/acoustic switch	Standard output file formats Runtime movie scaled to window size
2	Setup previewer Array builder Transducer models	Impedance bc Topography/voids Large contrast materials	Derived fields (e.g. divergence)
3	Resource estimation Multi-run scripts	Nonuniform grids Parallel version	Output format options (binary, jpeg, mpeg)



Acoustic reflections from surface pit in optical glass, with comparison between experiment and E3D simulation.

Determining cost versus performance tradeoffs of flashlamps requires understanding the voltage standoff characteristics of quartz in the presence of occlusions (voids).

Producing flashlamp light involves applying an anode-to-cathode potential gradient significant enough to cause the interior gas (typically xenon or other noble gas) to ionize. During this ionization process one or more streamers are formed, typically from the anode to the cathode. Voltage-breakdown physics insights can be gained from simple electrostatic modeling and experimentation.

We performed a set of 2- and 3-D electrostatic modeling simulations involving parametric studies of void diameters, void positions, reflector distances, and streamer diameters of both axial and transverse directions. To verify our simulations, we conducted a series of convergence and mesh refinement checks. We also compared the results to analytic solutions for point charges above dielectric half-planes, with excellent agreement. The streamer pathway(s) usually form along the return conductor (reflector) as shown in Fig. 1. The voltage gradient between the streamer and ground can be very high and susceptible to breakdown, especially in the presence of voids.

Shown in Fig. 2 (a) are typical computed electric field values for a 50-kV, 1-mm source streamer impinging axially on the quartz for various void diameters. Figure 2 (b) shows that the occlusions result in only small to modest perturbations to the potential field.

We also conducted experimental breakdown tests of various voids in the quartz lamps that are in qualitative agreement with our analysis. Based on our analysis and testing, we conclude:

- 1) Streamer diameter has a strong dependence on the potential fields and stress gradients within the quartz.

Electromagnetic Modeling of Voids in Quartz

D. Steich, J. B. Javedani, G. J. Burke

The objective of this project was to study quartz voltage standoff in the presence of embedded occlusions. The results indicate that the key parameters that influence voltage standoff are occlusion proximity to the breakdown pathway, occlusion distance from quartz inner surface, and occlusion thickness.

2) In order of importance, the dominant parameters degrading quartz standoff voltage are: a) occlusion proximity

and d) return conductor standoff distance [the smaller, the worse the degradation].

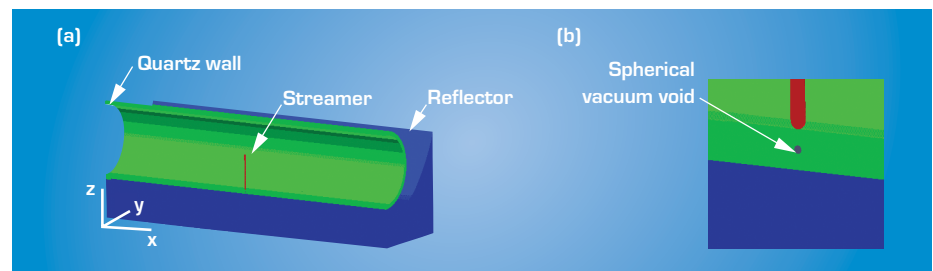


Figure 1. (a) Flashlamp, x-z cut plane. (b) Streamer and embedded spherical void in the quartz wall.

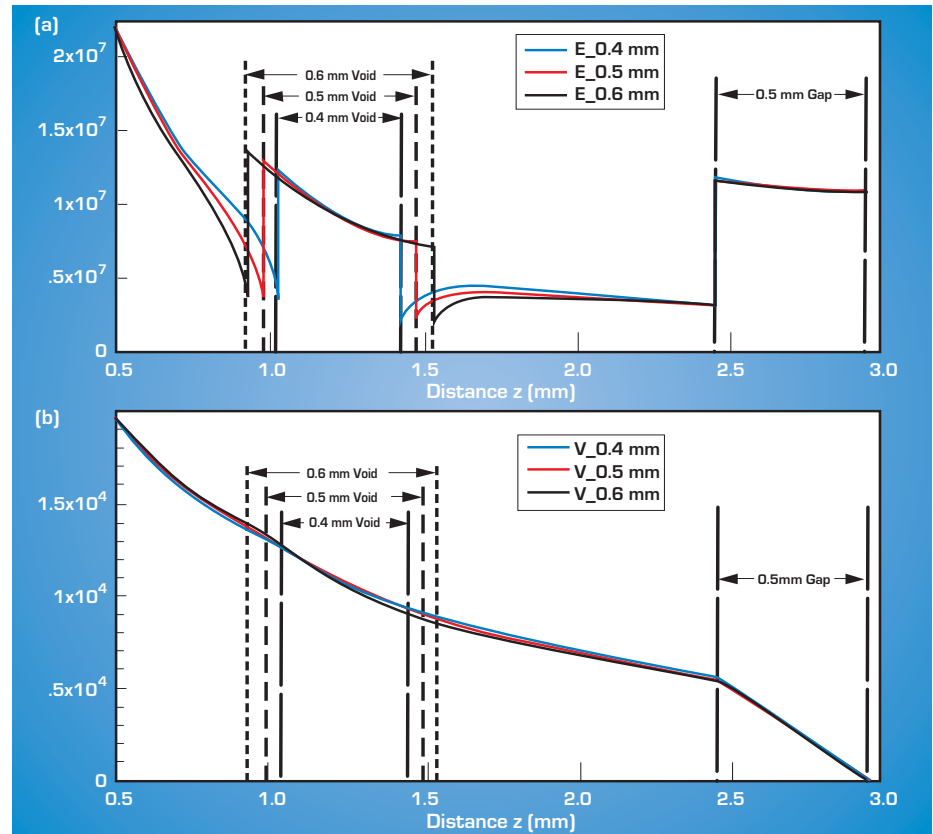


Figure 2. (a) $|E|$ profile and (b) potential profile, as a function of axial distance for a centrally embedded spherical void with varying diameter.

Engineers at LLNL often face electromagnetic problems that require capabilities that are not standard in the commercial simulator industry. Fortunately, there are so many good electromagnetic (EM) codes available, both research and commercial varieties, that it is increasingly possible to find a code that is easy to use and is a good match for the problem.

Our approach was to identify a large number of candidate codes (over 20), particularly 3-D codes, and collect first-order information on them by performing web searches and by talking with code developers, code vendors, users, and experts in the field.

The software packages that looked most promising for our applications were further evaluated, and where possible we ran simple problems, paying particular attention to learning curve and general ease of use. We constructed a table with high-level information such as numerical method and web links.

Using the first-order information, we narrowed the pool of codes for further investigation to Ansoft HFSS, CST MAFIA and Microwave Studio, and

EM Code Characterization for Accelerator Experiments and Lightning Safety Assessments

C. G. Brown, Jr, J. B. Javedani, M. M. Ong, G. E. Vogtlin

The purpose of this project was to survey the field of available electromagnetic codes and to provide code users with guidance in choosing optimal codes for their particular needs. Although we focused on two specific modeling areas, accelerator cells and lightning strikes to sensitive structures, the results are useful for a broader range of problems.

Remcom XFDTD. Our refined pool of codes contains only commercial codes. This preference was due mainly to their ease of use, better documentation, and more favorable learning curve.

To gain more experience with the EM codes, we ran simple models on the refined pool of codes. The figure below is a montage of some of the models. From these more in-depth investigations, we made several general observations.

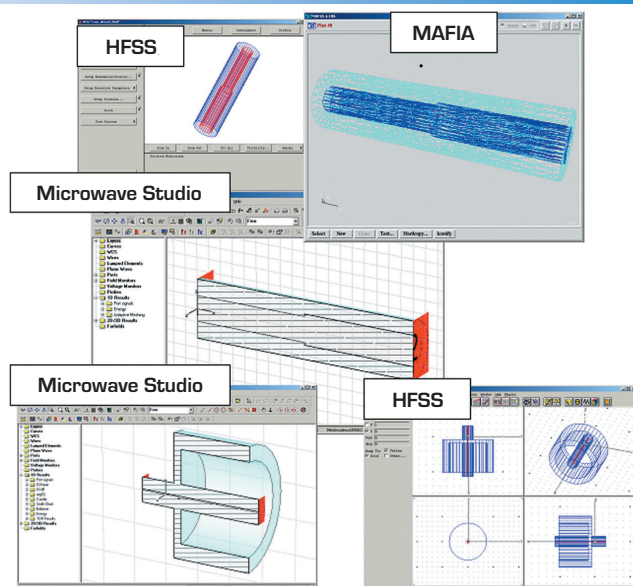
First, there is an essential set of information about a code for determining whether it will work for a given problem. For instance, in accelerator cell simulations, inclusion of a ferrite might be of interest, so it would be important to determine whether a code has a ferrite material model and whether that model is linear or nonlinear.

Also, electrical current sources and thin-wire materials are needed in certain lightning safety studies. If a code has such features, it might be applicable. To organize such information, we have created an EM code survey form (see table) that defines a code's capabilities in terms of parameters such as numerical method, materials, excitations, bound-

ary conditions, and mesh generation. Eventually, we hope to have such capability forms for each software package linked to the first-order information table.

Codes differ in ease of use and learning curve. These factors should be considered in the real cost of a code. Some factors that affect the ease of use are the time to prepare the input, ease of manipulating the results, existence of example problems and tutorials, and level of support locally and from the vendor.

Finally, EM codes are in a constant state of flux, which makes it difficult to keep pace with their capabilities. However, their rapid evolution widens the field of possible simulations. If one version of a code cannot run a given problem, it is entirely possible that the next version may have that capability.



Montage of EM models.

EM Code Survey Form.

- | | |
|--|---|
| <ul style="list-style-type: none"> • Electromagnetics solver <ul style="list-style-type: none"> – Version – Past Applications – Availability – Platform – Numerical Method – Validation • Input <ul style="list-style-type: none"> – Geometry – Mesh Generation – Materials – Excitations – Boundary Conditions | <ul style="list-style-type: none"> • Output <ul style="list-style-type: none"> – Postprocessing – Visualization • Technical Support <ul style="list-style-type: none"> – Links – Support & User Group – Publications • Evaluation <ul style="list-style-type: none"> – Strengths/Weaknesses – Learning Curve |
|--|---|

The first year of this technology-based project focused primarily on construction of the physical facility and system integration. The emphasis for the next years has been on demonstrating the production capabilities of the facility.

As a presentation theater, the facility integrates a large projection video screen and surround audio system with a number of media sources, as specified below. Presenters can easily patch a laptop computer into the system or use the resident hardware to exhibit their material on the large display. The room provides seating for 10 to 15 people and provides an unclassified environment suitable for small-group collaborations, software demonstrations, or video presentations.

As a media production workshop, the facility also enables high-quality visualizations to help engineers better communicate their ideas. The intent is to enhance good engineering with the best possible media tools and presentation techniques. High-end animation, compositing, and image-processing software, staffed by knowledgeable operators, provide the tools and expertise necessary to achieve this goal.

Production activity this year focused on a new movie entitled, "Seismic Analysis of the Morrow Point Dam" [see figure]. Like past EVT productions, it was desirable that the movie should 1) fill programmatic needs; 2) demonstrate a path for visualizing computational results by incorporating actual data; 3) showcase various types of animation to illustrate the creative possibilities and techniques that are available for engineers to use in future animation productions; and 4) generally demonstrate the EVT's capability.

Engineering Visualization Theater

M. D. Loomis, R. M. Sharpe

The Engineering Visualization Theater (EVT) was established as a venue in which to highlight work being performed by LLNL's electronics and mechanical engineering personnel. We accomplished this by creating an appropriate space, assembling the necessary hardware and software, and providing visualization expertise for the production and presentation of high-quality audio/visual media.

The analysis of the Morrow Point Dam was notable for its size and complexity. As such, it was an ideal candidate for a movie. It used both the NIKE3D and DYNA3D LLNL finite-element codes; featured numerous contact surfaces and boundary conditions; and, unlike typical dam analyses of the day, it included the surrounding land mass as part of the calculation.


The EVT used its modeling capability to provide an accurate 3-D surface representation of the Morrow Point topography used in the analysis. EVT personnel then executed a storyboard that would convey the significance of the analysis and present the results in an

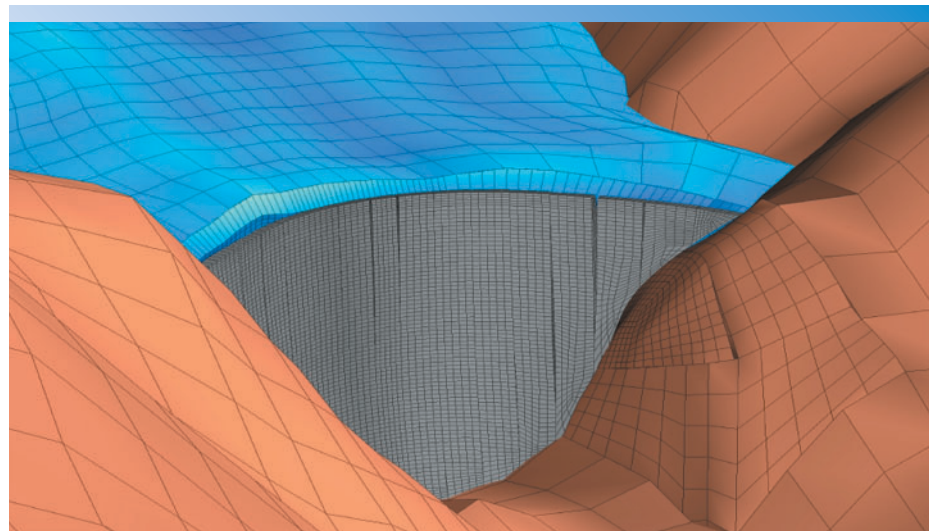
interesting way. The result was a movie that brought engineering ideas to life in a form that was both instructive and visually compelling.

This and other animations were previewed for several key engineering personnel on the large video screen in the EVT facility. By combining creative media produc-

tion with the display capabilities inherent in the assembled hardware, we believe that the presentation demonstrates the potential for using the EVT as a tool to effectively communicate engineering concepts.

The hardware for this project includes two computers, a large screen display, a digital disk recorder, an S-VHS video recorder, a video monitor, a DVD player, surround sound speakers, an AV receiver, a video switcher, and a video network feed from LLTN.

Software includes 3-D animation, compositing, image processing, video editing, DVD authoring, format conversion, and digital video compression. 



Nonlinear seismic analysis of Morrow Point Dam showing vertical contraction joints opening (displacements scaled by a factor of 50).

The project milestones are: verification and validation of the general CFD capability of the code through a series of selected benchmark problems (FY03); and implementation and testing of an advanced turbulence model, and verification and validation of the general capability of Star-CD (FY04).

In FY03, the OVERFLOW suite of codes has been applied to two different validation problems to verify both the code's capability as a general-purpose tool and the overset grid technology as a feasible method to expedite mesh generation.

The first problem is that of unsteady flow within healthy and diseased basilar arteries. This type of flow modeling capability could potentially be used for investigating the flow in vascular systems. Additionally, the medical community may benefit from these results through a better understanding of the mechanisms that contribute to aneurysm growth and rupture, which may lead to improved techniques for aneurysm diagnosis and treatment.

The incompressible Navier-Stokes equations are solved in a simplified model of the basilar artery and posterior communicating arteries. For these initial simulations, a steady inflow velocity boundary condition is applied to the basilar artery. Note that the underlying flow structure in the aneurysm dome is highly unsteady.

Figure 1 shows the time-averaged shear stress magnitude on the walls of the arteries, highlighting regions of high- and low-wall shear stress. A comparison of the flow structures within the diseased artery with those observed in experimental data demonstrates that the computed solution is properly capturing the flow physics. Other comparisons with experimental data have been made from the information extracted from the unsteady solutions for the location and motion of vortical structures in the aneurysm dome.

The second validation problem is a simulation of the complex, unsteady turbulent flow between a tractor and trailer. This flow has been identified by the DOE Heavy Vehicle Aerodynamic Drag Project

Enhanced General Purpose Fluid Dynamics Modeling Capability

K. Salari, J. M. Ortega

This is the first year of a two-year project to enhance LLNL's general capability in modeling complex, unsteady, turbulent compressible and incompressible flow fields using an overset grid technology.


as one of the main contributors to the aerodynamic drag of a heavy vehicle. Observations from experimental data have shown that the gap flow randomly transitions between two states: a symmetric state (low drag) and an asymmetric state (high drag). This unsteady turbulent flow has been simulated with OVERFLOW using overset grids.

The computed results are highly time dependent and, over the course of the simulation, multiple symmetric and asymmetric states are observed. Figure 2 shows an instantaneous velocity vector field in the gap for the asymmetric state. The flow field shown in Fig. 2 compares favorably with that seen in the experimental data.

These simulations provide information that can be used to lower the aerodynamic

drag through the use of add-on devices that could potentially eliminate the asymmetric state.

The OVERFLOW suite of codes has performed reasonably well in computing complex, unsteady flows in compressible and incompressible flow regimes using overset grids.

In FY04, an advanced hybrid Reynolds Averaged Navier-Stokes (RANS)/Large Eddy Simulation (LES) turbulence model will be added to OVERFLOW for improving the accuracy of unsteady flow simulations, such as unsteady turbulent massively separated flows. The new model will apply the RANS formulation to predict the high Reynolds number flows near surfaces (e.g., boundary layer and flow separation) and LES away from the surface (no-slip boundary). This new approach has successfully modeled massively separated turbulent flows where standard RANS turbulence models have failed. In addition, The Star-CD suite of codes will be tested on several benchmark problems of current interest to verify its utility as a general-purpose tool. 

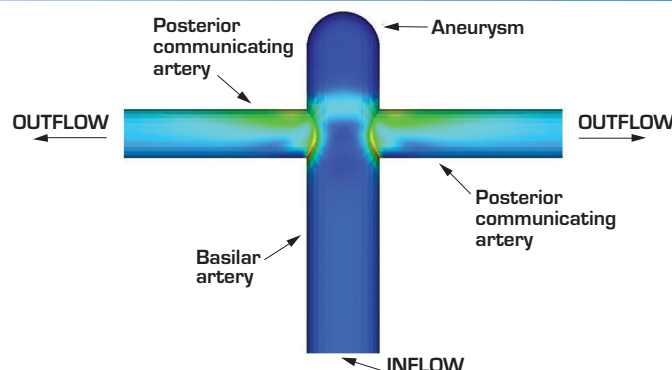


Figure 1. Shear stress magnitude on artery walls.

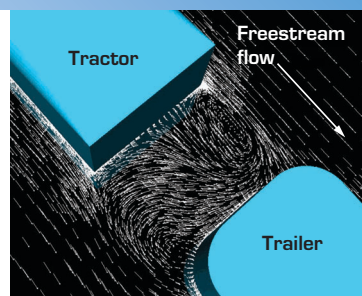


Figure 2. Velocity vector field in the gap between a tractor and a trailer.

Over the years, DYNA3D has faced an ever-increasing desire by users to have more information written to the output database for subsequent result visualization. This demand is especially high on the various element state variables such as stress, and other material response quantities.

The extension of the element state data option was implemented with consideration of flexibility and storage management. A user now has the option to add a single or a collection of state variable(s) for materials of his choice into the output for a particular simulation. By default, only the previous standard element state data will be included in the database for storage economy.

The implementation of the additional element state output was programmed in Fortran 90 due to its flexibility. However, mixing Fortran 77 and 90 caused optimization problems during compilation and/or execution on various UNIX platforms. The problems arose when using a uniform set of optimization

Enrichment of Output Database and New Capabilities for DYNA3D

J. I. Lin, E. Zywicz

With the use of the Mili I/O library, DYNA3D now has the capability and flexibility to add almost any data to the output database. In FY03, we have enriched the output database to include options for the full range of element state variables, accumulated contact frictional work for selected slide surfaces, element time step size, and double-precision nodal positions.

options for both the Fortran 77 and 90 subprograms, and are attributed to the individual vendor's compiler deficiencies.


After repeated effort, we were able to install a near-term workaround in DYNA3D to make it run on all available UNIX/LINUX platforms. The compiler deficiencies were reported to their respective vendors and should be corrected in the future releases.

The inclusion of contact frictional work is to complement the existing output of contact tractions/forces. This additional information enables the user to monitor the contact activities in greater detail, and can also be read in as heat sources

for subsequent thermal analyses by programs such as TOPAZ3D.

A simple ball-drop test, shown in Fig. 1, was used as a sample problem. The frictional work distribution on the target surface, shown in Fig. 2, exhibits the desired symmetric pattern.

A user could employ the element time step display to assess the discretization adequacy for mesh management. For example, the element time step display can tell the user what parts of a structure need to be remodeled to achieve a specific stable time step. The optional double-precision output for nodal positions is added to improve post-processing of strains in the presence of large rigid body motions.

A new material type, the Johnson-Holmquist II (JH-2) constitutive model, was also added to DYNA3D's material model library. JH-2 is a rate-, pressure- and damage-dependent constitutive model designed for simulating brittle materials such as ceramics. This model was made available to us by the Army Research Laboratory. 

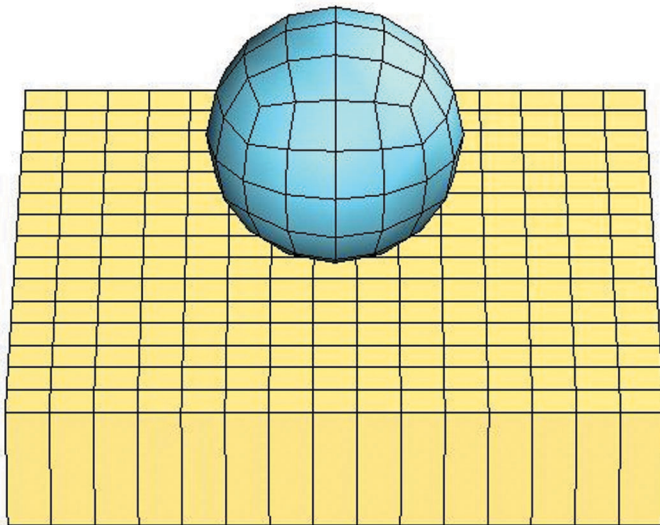


Figure 1. Sample problem for contact frictional work display.

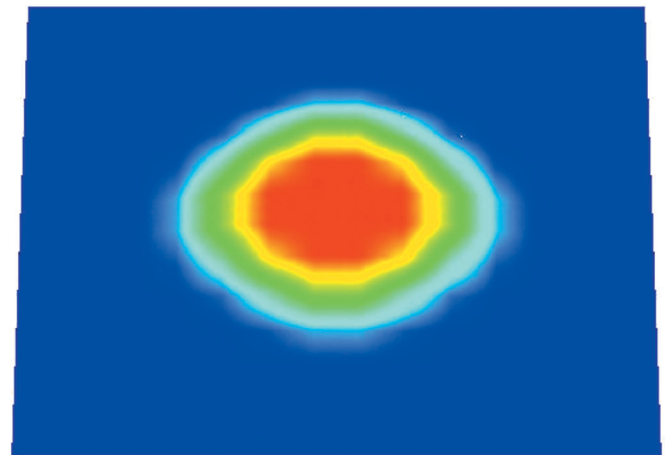


Figure 2. Final contact frictional work on target surface.

Over the past two decades, there has been increased work in small fuel cells and in miniaturized systems for providing them fuel on demand. Applications include consumer electronics such as cell phones, laptop computers, video camcorders, and radios, as well as military systems such as microscale field energy sources for various sensors and remote communication devices.

Methanol steam reforming has been heavily studied, due to the lack of inter-carbon bonds in methanol, to the limited carbon monoxide production, and to a higher hydrogen fraction in the reformate than that of partial oxidation. A MEMS-based micro-reformer has the advantages of small features; of integrating many components in a coherent way; of obtaining microfluidic stability, due to small Reynolds number; and of requiring relatively low heating energy, owing to its small size.

Thermal management of microscale fuel cells is particularly key for four reasons. First, the high temperature of the fuel-reforming reaction must be isolated from human users for safety reasons. Second, efficiency and useful device life can be strongly influenced by the

MEMS Models for Microscale Fuel Cells

M. A. Havstad, J. D. Morse

In earlier work, surface chemical kinetic and plug flow reactor (PFR) models of a steam-reforming process were implemented in TOPAZ3D and exercised, and the PFR approach was validated against tests and a commercial CFD code (FLUENT). This year we have focused on thermal management to fully test our coding and to support device work at LLNL. Driving device size down and suggesting a viable start-up scenario were our principal aims.

amounts of waste and start-up heat required. Third, it is desirable to minimize the thermal signature of any power source. Fourth, total device size must be smaller or comparable in size to other system components. Modeling, rather than repeated fabrication and testing is the preferred approach to arriving at working, cost-effective solutions to these thermal management issues.

Our modeling has shown that the most advanced forms of solid insulations available today, aerogels for example, are inadequate for the project requirements: a 1-in.³ reforming package with an exterior temperature of 40 °C. The required isolation options are summarized in Fig. 1. Only evacuated aerogels display thermal conductivities low enough to approach the 40 °C limit. Alternatively, sets of highly reflective thermal radiation shields layered in an evacuated enclosure

about the reforming package can also approach the low temperature requirement, if the shields are sufficiently reflective and conduction paths due to shield touching are adequately minimized. We are currently modeling and testing a variety of radiative shielding packages.

TOPAZ3D simulations of device start-up have been used to assess time to full conversion efficiency, fuel lost during start-up and heating [I^2R] power required to establish reforming. Figure 2 shows the time dependence of methanol, hydrogen and carbon dioxide flow rates at the reactor exit for a start-up consistent with currently practical battery power. Since the time dependence of conversion efficiency follows closely that of hydrogen flow, we see that current heating and thermal isolation translate into a 20-s start-up time (time to significant fuel cell output for recharging the start-up battery and doing useful work). We can drive this start-up time down by reducing system thermal mass, increasing the capacity of the battery used to provide the start-up I^2R heat, or by burning the unreacted methanol during start-up and coupling the heat of combustion to the reforming reactor.

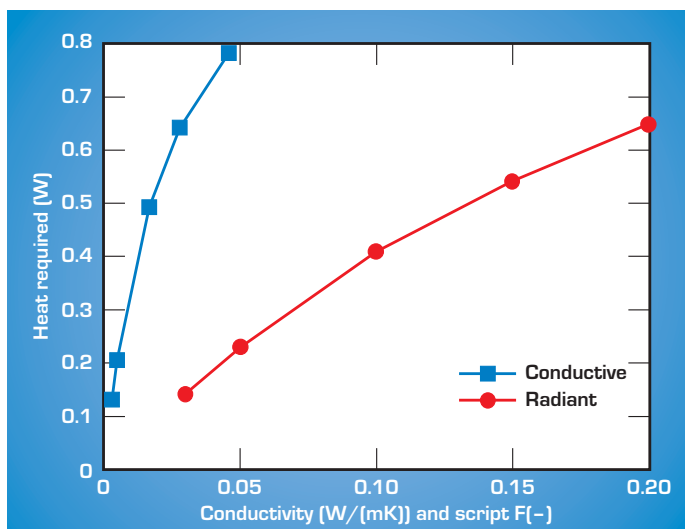


Figure 1. Required isolation options for insulations.

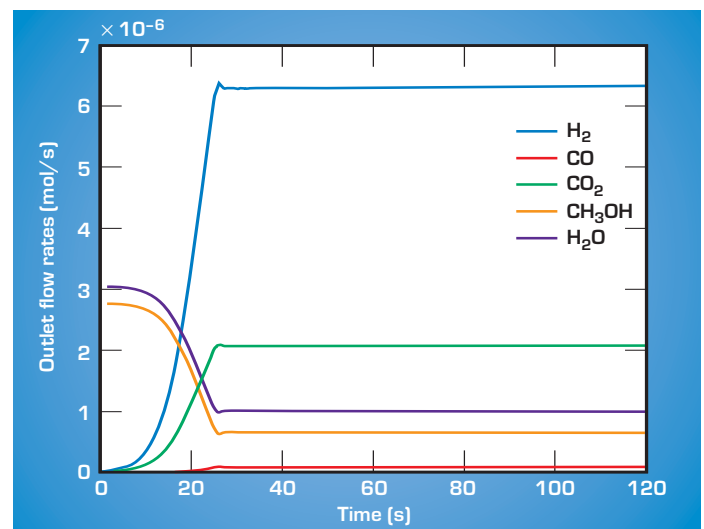


Figure 2. Time dependence of flow rates for various substances at the reactor exit.

Among the changes to GRIZ, the single greatest improvement was a major extension of the time series plotting capability called an "operation" plot [command *oplot*]. The operation plot permits GRIZ users to create new time series that are the difference, sum, product, or quotient (on a pair-wise sample basis) of two input time series. With the *oplot* command, for example, a user can plot the difference in displacement between arbitrary pairs of nodes in a mesh.

The rich *oplot* command syntax does not limit users to operations between time series on mesh objects of the same class. As an example, instead of computing the displacement difference between two nodes, it would be just as easy to compute the difference between the displacement of a node and the rigid body displacement of a particular material.

It is also possible using *oplot* to simultaneously compare results from a particular object with results from a list of other objects. As with the regular *plot* command, *oplot* syntax permits the use of defaults to enable more compact

Post-Processing and Data Management Enhancements

D. E. Speck, E. M. Pierce

This element of our technology-base program is devoted primarily to the ongoing maintenance of the GRIZ finite-element post-processor and the Mili I/O library. Mili provides the primary data path between our analysis codes and GRIZ. For FY03, this effort was chiefly manifested in the resolution of 28 Software Change Requests (SCRs), 16 of which pertained to GRIZ, and the remainder to Mili. The body of SCRs includes both enhancements and bug fixes.

expressions. Finally, *oplot* is fully integrated with the *outth* command for writing data straight to a text output file and the *gather* command to pre-compute the resultant time series into memory without displaying them. The figure shows a plot of the difference in the x-displacement [*dispx*] between node 376 and four other nodes [476, 576, 676, and 776].

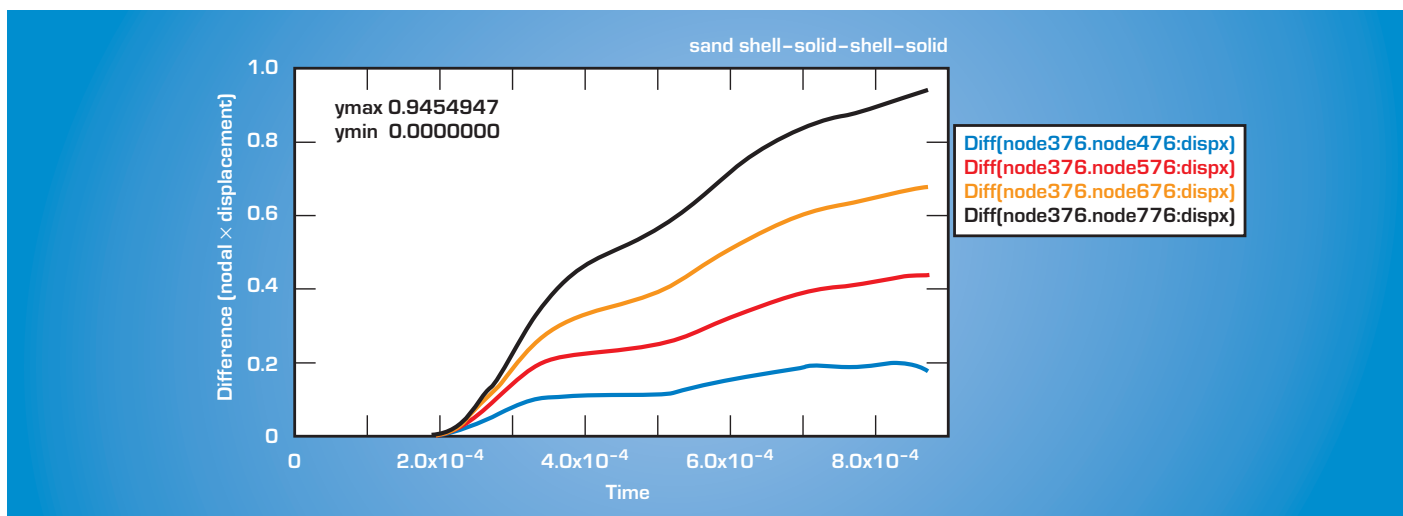
Another GRIZ enhancement builds on efforts completed in FY02 to permit input of double-precision data. That effort implemented basic compatibility by adding logic to detect double-precision data and convert them to single precision on input. In FY03, GRIZ's strain and relative volume calculations were extended to accept double-precision inputs directly. This

takes advantage of an earlier enhancement of DYNA3D to output double-precision displacements and dramatically improves the usefulness of the strain calculation when strains are relatively small, especially in the presence of large displacements. In such cases the existing single-precision calculation was unable to com-

pute accurate answers.

Mili-related efforts this year were primarily maintenance-related bug fixes. One effort worth noting is an ongoing effort by other LLNL programmers to integrate Mili into the new VisIt post-processor, a state-of-the-art visualization application.

FY03 also saw the formation of a Change Control Board (CCB) for post-processing and data management software. The CCB was formed to provide a formal platform for communication between the analyst and programming communities on post-processing and related matters. It also permits and requires the various groups of users to come together to establish priorities for post-processing code work.



Plot of the difference in the x-displacement between node 376 and four other nodes.

To increase our understanding and ability to build accelerators, transmission lines, and RF components and systems, we purchased a license for Microwave Studio [Computer Simulation Technology (CST)], a 3-D modeling code that solves Maxwell's equations for a configured model of an actual object.

Microwave Studio is a user-friendly EM solver. Taking advantage of dramatic gains in computing power in personal computers, it combines a graphics-driven "front end" where a user constructs a geometric model using tools and methods rooted in modern CAD codes, with a novel finite-integration algorithm that

RF Component Toolbox Using Microwave Studio

B. Rusnak

Capability has been furthered in using an advanced electromagnetic 3-D modeling software package called Microwave Studio. Skills have been enhanced by modeling the behavior of a variety of RF components that make up a "toolbox" of techniques that allow more efficient use of the code.

solves Maxwell's equations on a 3-D mesh more efficiently than conventional differential methods.

In the past year, a variety of RF components related to linear accelerator technology have been modeled using Microwave Studio. (See Figs. 1, 2, and 3.) The problems spanned dielectric resonators, resonant bandpass RF windows, half-wave spoke and cylindrical

resonators, non-resonant RF fast tuners, lumped circuit model simulations, ferromagnetic material effects on RF transmission in a cavity, and induction linac cavity model construction.

Capability in the code that was explored included transient excitation and eigenmode solutions; parametric analysis and optimization; material property effects; model response in the form of S parameters, Smith charts, and energy; and field patterns in the model. Post-process calculations of quality factor (Q), cavity loss, and time-domain reflectometry (TDR) response were also performed.

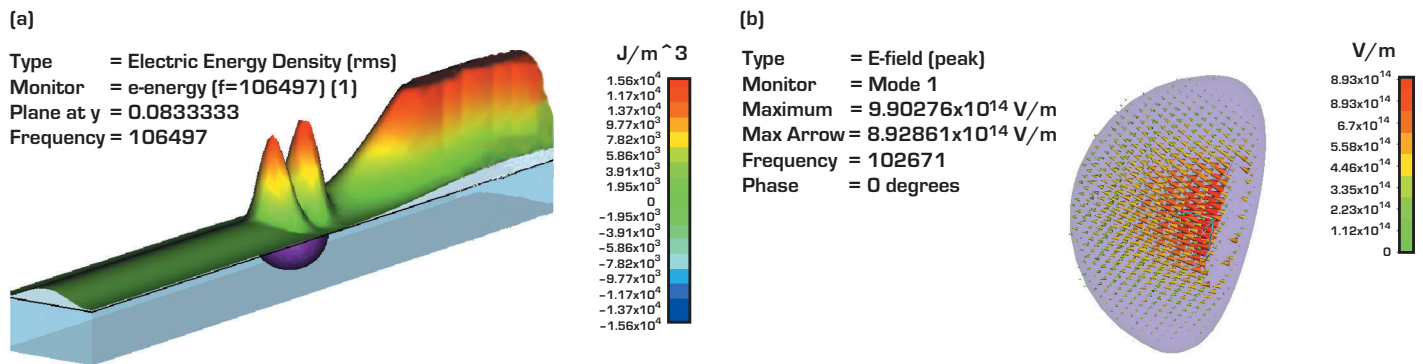


Figure 1. (a) Plot showing energy density in a dielectric sphere placed in a waveguide, driven at 107 THz. (b) Field pattern for the lowest frequency eigenmode in a spheroidal resonator 1 μ m across.

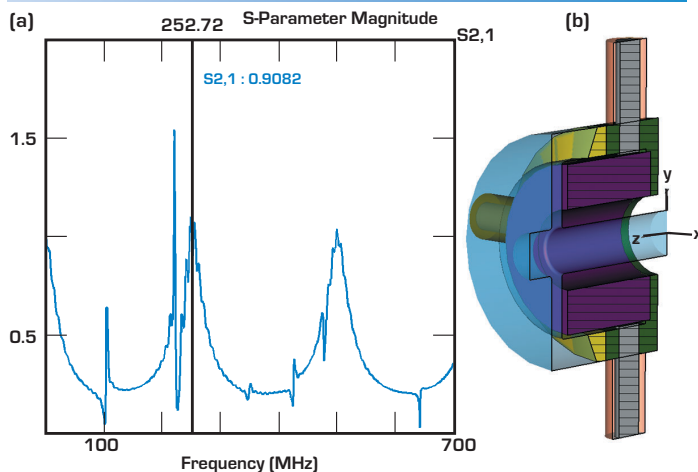


Figure 2. (a) S-parameter plot of transmission through an induction linac cavity, showing dominant passbands and resonant modes. (b) Graphic representation of the induction linac cavity modeled. Full 3-D model was created in approximately 2 h.

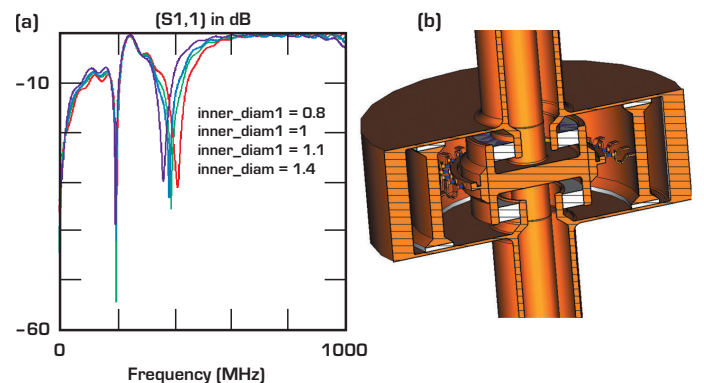


Figure 3. (a) Parametric evaluation of passband characteristics of a resonant window assembly. (b) Graphic representation of a coaxial transmission line resonant passband window assembly modeled using Microwave Studio.

There is increasing interest in uncertainty quantification tools throughout LLNL. Sensitivity analysis plays an important role in the overall quantification of uncertainty for model output, necessary in the integration of data with models, in decision making, and in stochastic methods for source-identification and sensor siting. By quantifying the effect of perturbations of the input parameters on the code output, sensitivity analysis provides a route for the quantification of the output uncertainty, while yielding relevant information on the relative contributions of various input parameters (see Fig. 1).

We have focused on the implementation of sensitivity analysis within LODI, the atmospheric dispersion code used for modeling emergency release scenarios at DOE's National Atmospheric Release Advisory Center (NARAC). The applied sensitivity analysis helps quantify the effect of rain on the plume spread and on deposition fields.

First-order, local sensitivity analysis was implemented within the wet-deposition module of LODI. Wet deposition occurs when rain meets an aerosol (particle) plume. The sensitivity analysis may be used both to estimate overall deposition field uncertainty and to compare the contributions of rain rate and particle size to that uncertainty (Fig. 2).

The LODI wet deposition module is logically split from the remainder of the dispersion calculation, so the sensitivities may be explored without concern for parameter and computational dependencies, and the linearization implicit in the formulation is acceptable. With this first-order local methodology, sensitivities are obtained from a differential

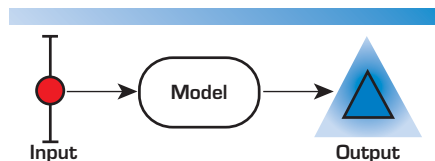


Figure 1. Representation of uncertainty in quantification tools. Input uncertainty contributes to output uncertainty.

Sensitivity Analysis

G. A. Loosmore, L. G. Glascoe, H. Hsieh

The intention of this project is to determine the sensitivity of dispersion code predictions to the specific input parameters of interest, and also to better understand the uses and limitations of sensitivity analysis within such a context. This project enhances the capabilities of the atmospheric dispersion code, LODI, and builds the core competency in sensitivity analysis within LLNL's Engineering Directorate.

equation describing their evolution in time. This initial effort involved a careful choice of algorithm, code enhancement, and analysis. The code enhancement was straightforward, and the added computation of sensitivities added little (a few percent) to the overall CPU time of the simulations.

A series of analyses were conducted with the upgraded code. Sensitivities to rain rate and particle size were examined for both suspended mass and deposition fields. Generally, simulations were slightly more sensitive to particle size than to rain rate for the domain of interest, although the contribution of uncertainty from the two parameters was of the same magnitude. This result indicates that good knowledge of both parameters will be necessary for robust simulations. Wet deposition sensitivities

to rain rate changed sign with distance downwind, indicating a complex dependence of the wet deposition field on the rain rate.

In FY04 we will address the temporally and spatially varying wind-field, a significant cause of uncertainty in disper-

sion calculations. To conduct sensitivity analysis for these inputs, it is necessary to define a logical perturbed windfield. Because simulations are conducted with mass-consistent gridded windfields generated from forecast models or observational data, the very notion of a perturbed windfield is undefined, and the uncertainty in the winds is poorly quantified. Hence, our next step for this project will be to build a tool to explore the sensitivities in these large meteorological input data sets and extrapolate a representative subset sufficient to capture the variability and uncertainty in the larger set. The reduced data set can then be used for both sensitivity analysis and consequence assessments. This data analysis tool, and the sensitivity analysis methodologies, will be available to other projects within the Laboratory.

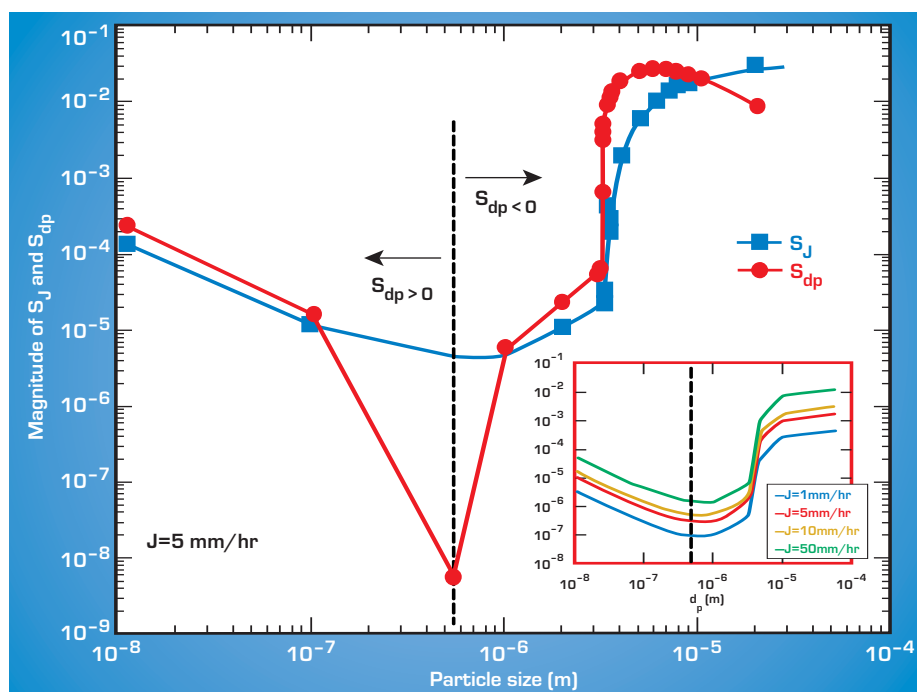


Figure 2. Sensitivities (S) to rain rate (J) and particle size (d_p), showing comparable values for particle sizes in the range 1 to 10 μm .

Since maintaining and updating a C++ solver library is a significant task in itself, it was determined that the interface should be created in an automated way, if possible. The idea was that after each modification of the solver library, updating the interface would be easy. To do this, a previously available Python script was modified to create the necessary C and Fortran 90 interfaces to the C++ solver library. After any C++ solver library updates, the Python script is executed. It creates the C and Fortran 90 interface source files. These files are compiled and added to library

Software Interface for a Parallel Solver Library

N. J. Champagne, M. L. Stowell

The primary goal of this project was to produce a software interface to the parallel solver library that was created under the solver LDRD project on numerical technology for large-scale computational electromagnetics. This software interface was needed since the solver library was created in C++, and there are many legacy engineering codes written in Fortran. With this interface, Fortran programmers now have access to the C++ solver library features such as serial and parallel, direct and iterative solvers.

archives. From there they may be linked to Fortran programs.

In all the examples, the simulations were done with EIGER, a computational electromagnetics program written in Fortran 90, and the solver interface. The radar cross-section (RCS) of

a perfectly-conducting (PEC) sphere with a hole, illuminated by a plane wave, is shown in Fig. 1. The sphere is modeled with finite elements in the interior and with boundary elements on the surface. The resulting matrix is a hybrid sparse/dense matrix, which is easily handled by the C++ solver library. The results from different processor runs agree very well.

The surface currents on a Predator are shown in Fig. 2. The currents are produced by a monopole on top of the fuselage. The frequency of the simulation is 350 MHz. The matrix for this problem is completely dense and was solved in parallel.

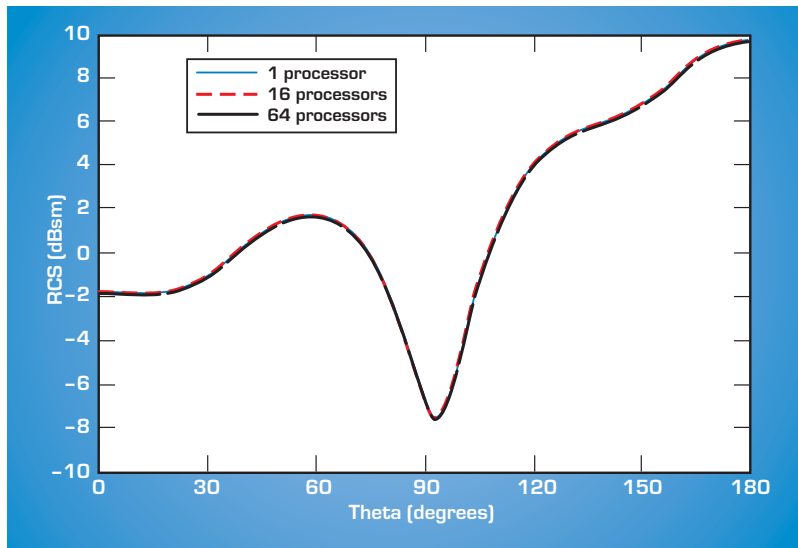


Figure 1. RCS of a PEC sphere with a hole for 1 processor, 16 processors, and 64 processors.

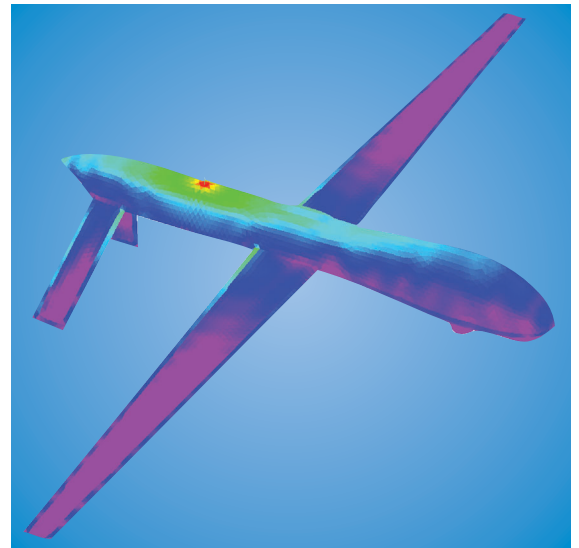


Figure 2. Surface currents on a Predator at 350 MHz.

The figure shows a laser amplifier module, including three slabs in the beam direction, two slabs in the stack direction, and the accompanying flash lamps and cooling passages. By symmetry, the model includes all four slabs in the stack direction. Boundary conditions in the beam direction can be altered to model finite-length diamond-end and x-end slab configurations, and also an infinite chain configuration. The model was created to capture amplifier thermal, structural, and optical recovery of targets, including the effects at end slabs and variations in coolant flow rates through different slab banks.

Radiant heat exchange between amplifier parts is computed with a matrix of exchange factors. MONT3D computes radiation-exchange factors between surfaces separated by non-participating media. This code and FACET are our two means to coupling thermal enclosure radiation to the solid conduction in TOPAZ3D. MONT3D permits more physically realistic conditions, such as specular and diffuse wavelength-dependent emitting, reflecting, and absorbing surfaces, rather than the simply gray and diffuse surfaces of FACET.

Thermal Code Enhancements

M. A. Havstad

TOPAZ3D, our uniprocessor thermal transport FEA code and MONT3D, our Monte Carlo-based radiation-exchange-factor code, were modified to simulate larger problems.

The input fields for MONT3D integer data-like node and element numbers were expanded from I5 to I8 format, i.e., the largest node number that can be specified or referenced increased from 99,999 to 99,999,999. Parallel execution under the Parallel Virtual Machine (PVM) communication library was revised to current library versions. The code will now run in serial or parallel on machines with the TRU64 operating system. Small benchmark problems have been run and used for verification of the new coding and a large amplifier problem is work in progress. Reviving the parallel capability provides important computational efficiencies to our engineering analysts.

TOPAZ3D input was also expanded from I5 to I8 format. However, this revision was insufficient for a very large amplifier end-effects thermal model. Not only did we need to read a larger problem specification, but also the internal capacity of the program needed to be expanded. The variables


acting as memory indices into large internal storage arrays were elevated from four-byte to eight-byte integers.

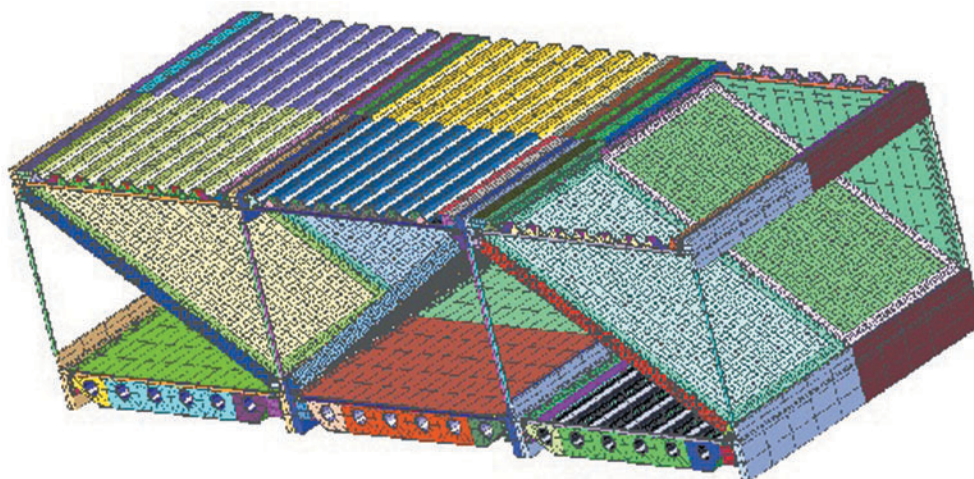
These larger problems reveal other issues in the code. The writing of

the large dump files associated with saving an intermediate state of the calculation has led to performance issues. Therefore, for purposes of the present amplifier analyses, the *dumpfile* option has been made inoperative.

An up-to-date users manual for TOPAZ3D has been drafted, in which new features, including the larger input format option, are described.

TOPAZ3D enhancement has also continued via several other areas of funding. Stockpile surveillance (SS) has funded coupling conduction to representations of surface corrosion, and both SS and an ASCI project on reentry vehicle dynamics have supported mesh motion/regression algorithms, due to the loss of material from the mesh occurring during both corrosion and ablative reentry.

A technology-base project for modeling of fuel cells and fuel reformers for fuel cells, described elsewhere in this volume, has funded methods for coupling models of chemical reactors to TOPAZ3D. 



Thermal model of laser amplifier module.

Verification and Validation Framework for Scientific Codes

K. Salari

This is the first year of a two-year project to provide education and training on formal verification, validation, and uncertainty quantification for engineering staff involved in code development, analysis, and experiment.

Users of computational simulations and developers of computational software face a critical issue: how confidence in modeling and simulation (see figure) can be decisively assessed. The verification and validation (V&V) of computational simulations are the primary tools for building and quantifying this confidence.

Briefly, verification is the assessment of the accuracy of the solution of the computational model (governing equations) by comparison to a known solution. Validation is the assessment of the accuracy of the computational simulation to the real world (experimental data). Validation science requires a close and synergistic working relationship between computationalists and experimentalists. This relationship is crucial for a well-established and successful V&V program.

In the first year, staff training was conducted through lectures on the following topics:

Verification assessment

- Fundamentals
- Computational error estimation
- Testing

Validation assessment

- Validation and prediction
- Validation error and uncertainty
- Validation experiment
- Guidelines for validation experiment

In the second year, training will include:

Validation assessment

- Statistical estimation of experimental error
- Validation metrics

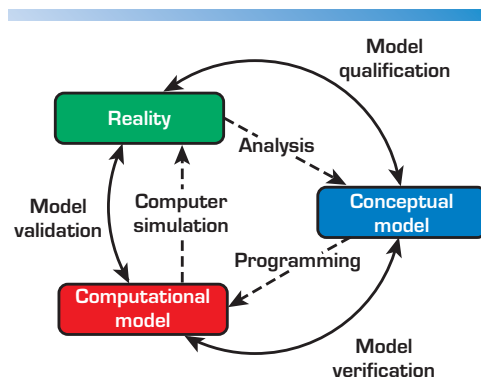
Uncertainty quantification in computations

Recommendations and critical implementation issues

Demonstration

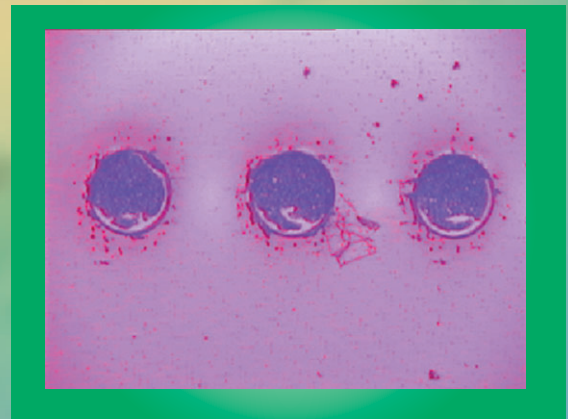
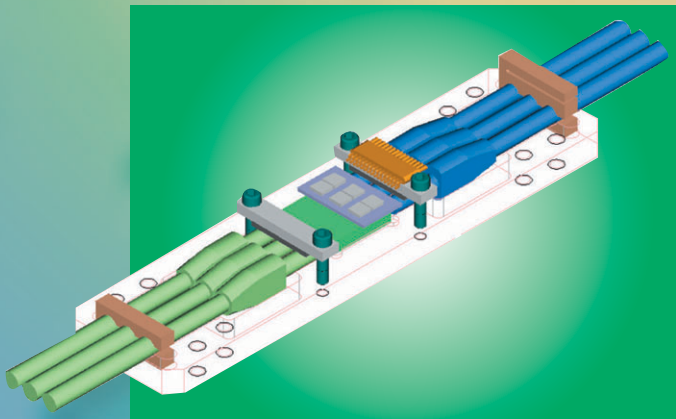
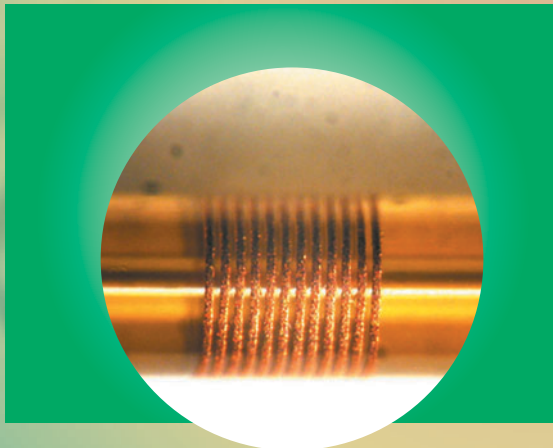
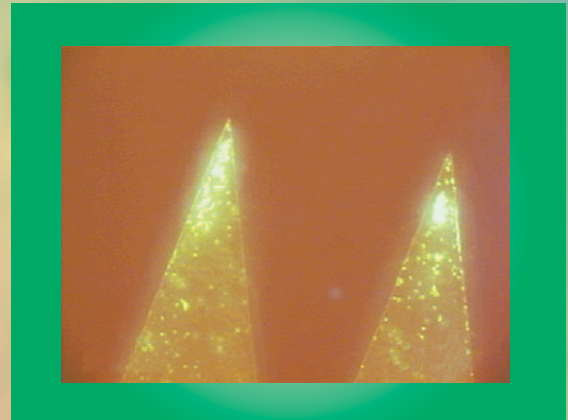
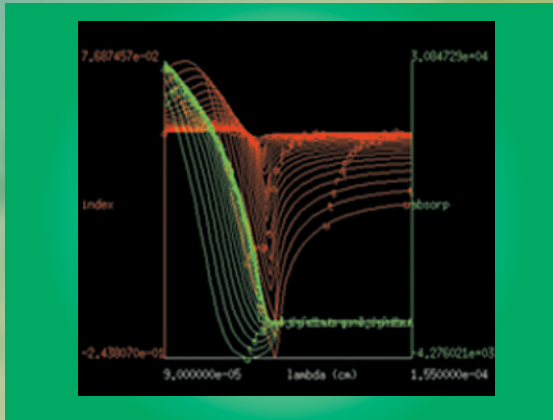
- Verification techniques
- Validation procedures
- Uncertainty quantification

An internal LLNL website has been established for current information about the V&V activity of this project.



Phases of modeling and simulation.

Center for Microtechnology and Nanotechnology



High-fidelity instrumentation is required for many diagnostic systems. These instruments must be reliable, fast (10 ps to sub-ps), sensitive (able to detect single x-ray photons), and have a large dynamic range. Existing commercial technologies cannot satisfy these requirements, but progress in photonic materials, devices, and circuits is making possible devices that may meet these needs. Emerging all-optical technologies and devices are being exploited in novel configurations for direct radiation detectors and recorders. Modeling tools are necessary to support these efforts.

Specifically, the radiation detectors being explored are basically all-optical switches, where ionizing radiation plays the role of an optical pump beam. Radiation creates electron-hole pairs in a semiconducting medium, which changes the index of refraction and modulates an optical signal.

The purpose of this project was to extend existing modeling tools in two directions: adding known semiconductor material modeling and optical device modeling.

For the material model, we computed changes in absorption and refractive index due to three effects: bandfilling, bandgap shrinkage, and free-carrier absorption.

Bandfilling occurs when the density of states is sufficiently low that a small number of carriers can fill the bands. The effective bandgap increases, because electrons in the valence band require more energy to be excited into the conduction band. Bandgap shrinkage occurs because injected electrons occupy states at the bottom of the conduction band, resulting in a lowering of the conduction band edge. The valence band edge similarly increases due to the presence of holes. The result is a shrinking in the gap between the bands.


Application of Modeling Tools to Photonic Devices for High-Bandwidth Diagnostics

T. C. Bond, J. S. Kallman, K. D. Akkerman

The purpose of this project was to extend the QUENCH2D_TD code to make it suitable for modeling x-ray sensors. This involved incorporating time-varying absorption and refractive indices into the code, as well as the ability to model reflection from scattering centers along a waveguide. After making these changes, and building the WAVEGAIN code to model the effects of changing carrier densities in bulk semiconductor waveguides, we were able to reproduce some of the effects seen in experimental x-ray sensors, and to make suggestions for speeding up their response.

Free-carrier absorption occurs because free carriers can absorb photons and move to higher energy states within a band. Absorption change was easy to compute for bandfilling and bandgap shrinkage, but index of refraction change was more difficult and had to be computed using the Kramers-Kronig relations (which link the real and imaginary [absorption] part of the index of refraction).

Optical-device modeling was also split into two parts: computing the effective indices of refraction as a function of wavelength and carrier density, and computing the optical responses of the device. We built the code WAVEGAIN (see figure) to perform the effective index computations and created files that could be loaded into QUENCH2D_TD. QUENCH2D_TD was modified to be able to read absorption and index of refraction from tables, to model the arrival of x rays using a Poisson stochastic process, and to crudely model the generation of carriers from x-ray absorption.

Using all of these updated tools we were able to qualitatively reproduce experimental data and to make suggestions for parameter improvements. 

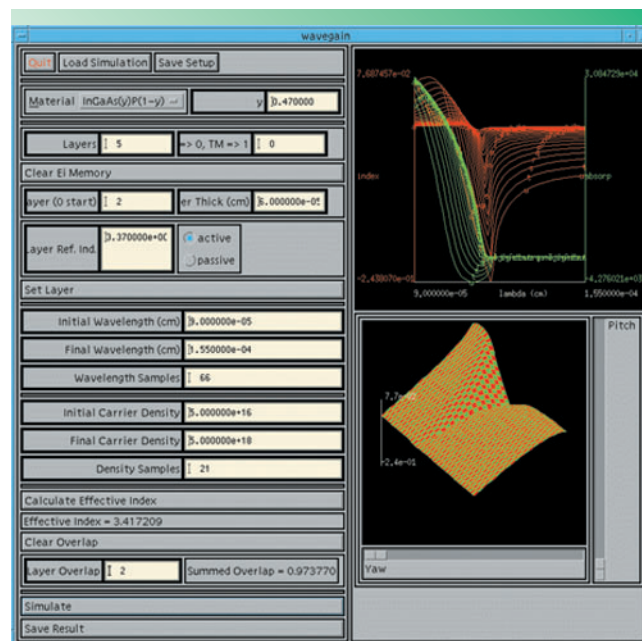


Illustration of the graphical user interface of the WAVEGAIN code. In this simulation, an InGaAsP layer is the active material in the waveguide being modeled. The graph at the upper right shows the change in index of refraction (red curves) and the absorption (green curves) as a function of wavelength (x axis) and carrier density (each curve is at a single carrier density). The graph in the lower right is a 3-D plot of the change in index of refraction as a function of wavelength and carrier density.

One of the biggest technical hurdles to overcome in detecting biological pathogens in the water supply is isolating the pathogenic organisms from the other solid debris normally associated with water. This includes both organic and inorganic material. Use of functionalized beads combined with filters has been suggested, but the feedback from a noted expert in the field of water security is that filters clog over time, and are therefore unsuitable for monitoring applications.

In this program we considered the use of dielectrophoretic fields to enable separation of potential pathogens from the raw water. A key advantage to dielectrophoresis is that body forces can be exerted on biological particles without occluding channels, thus mitigating clogging, the biggest impediment to continuous monitoring. Another advantage of using dielectrophoresis is that there can be some capture selectivity depending on the frequency of excitation. Thus, it may be possible to separate bacteria from other particulates earlier in the sample preparation process to make the overall system more robust.

We have worked extensively with dielectrophoresis over the past several

Biological Pathogen Extraction from Raw Water Sources Using Dielectrophoretic Forces

R. R. Miles, K. A. Bettencourt, J. J. Crawford

Since 9/11 there has been an increased awareness of the vulnerability of U.S. infrastructure to terrorist attacks. As a result, there is a heightened concern about the safety of our water supply. One could easily conceive of a saboteur introducing pathogenic species, such as cholera, downstream of treatment facilities, thereby inducing widespread sickness within the civilian population. Pre-symptomatic action following such an attack requires the ability to detect biological pathogens in the water supply. We have considered the use of dielectrophoretic fields to enable separation of potential pathogens from the raw water.

years, demonstrating particle capture, but three important issues needed to be resolved for this application. First, the electrodes needed to be more robust than those used previously; second, the working distance for the forces needed to be increased from its previous distance of 25 μm ; and lastly, we needed a bigger area over which the force could be applied.

We demonstrated the application of 49 V peak-to-peak at 2 MHz without electrolysis, using a superfine, but fragile, glass needle-electrode. This enabled collection of cells from up to 1 mm away from the electrode.

In this project, we built arrays of metal needle-electrodes in an attempt to duplicate the results of the glass needle-

electrode in a more robust fashion, but found the precision of manufacture to be an important factor in a working dielectrophoretic system. We therefore returned to microfabricated parts. We built a relatively simply etched set of saw-toothed needle-electrodes etched straight through a wafer. Sets of these electrodes can easily be stacked in an array to increase sample throughput.

These electrodes did collect particles, as shown in Fig. 1. However, the speed of collection was far too slow for processing the large amount of water sample desired. We believed that an improvement would be gained by going to a 3-D etched needle-electrode, as shown in Fig. 2. We built arrays of these electrodes and are in the process of obtaining a transparent tin-oxide topside electrode for viewing.

Concurrently, we are investigating more robust surface electrodes to stack multiple layers of interdigitated electrodes. In the past, we have demonstrated that interdigitated electrodes were effective at collecting particles, but the metal electrodes degrade with time. We are in the process of fabricating improved electrodes.

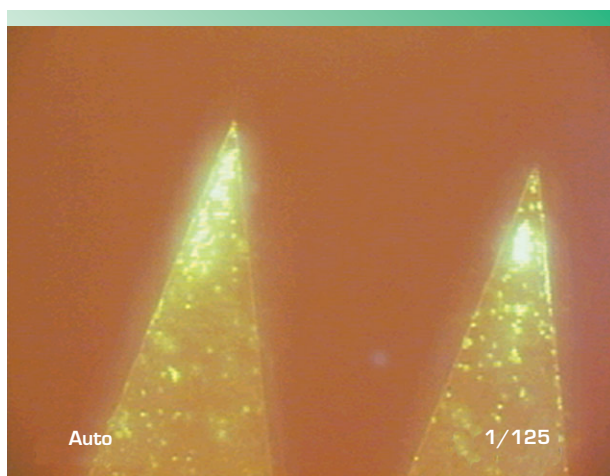


Figure 1. 2-D needles capturing particles.

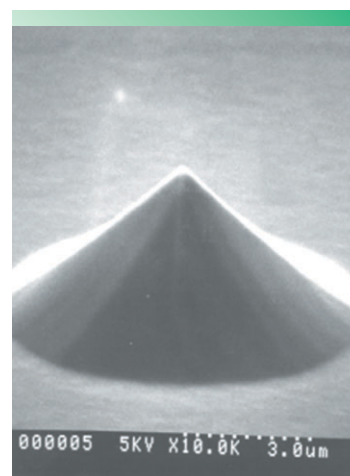


Figure 2. 3-D needles.

M easurement of dynamic contact stresses or interface stresses between contacting surfaces poses a number of instrumentation challenges. Introduction of measurement hardware at the contact interface inherently alters the stress to be measured. The successful measurement relies on a minimally thick, membrane-like instrument in the load path to avoid alteration of the contact mechanics. For this reason, microfabrication techniques were selected to form this small sensor.

Silicon was selected for the transducer for its consistent elastic behavior and high gage factor, both well suited for the 30-year lifespan and accuracy requirements of the sensors. Processing techniques were used to form piezoresistive sensors in a wafer surface. The devices

Contact-Stress, Deflection, and Strain MEMS Sensors

J. Kotovsky, S. P. Swierkowski

LLNL's Stockpile Stewardship mission requires miniature, high-fidelity sensors to be installed in weapons systems. Commercial sensors are not suited for the environmental, physical, and performance demands of weapons testing. This project explored and produced three sensors as part of the ongoing effort to test specialized instrumentation: silicon-based contact-stress, deflection, and strain microsensors.

were then thinned and their shape defined by wet and dry silicon etching.

The resultant silicon chip contains a thermally-compensated single sensor of 55- μ m thickness (Fig. 1). It is embedded in a flexible polymer package that mimics existing materials used in weapons and other assemblies to preserve interface mechanics. A typical device on a wafer shows 290 Ω /MPa sensitivity and 1.25% imprecision, although a large range of loads and sensitivities is achievable. Future efforts

will demonstrate the sensors as high-density 2-D arrays capable of conforming to arbitrary, complex curvatures.

Two sets of optical deflection and strain sensors have been made this year. The sensors transduce deflection and strain to dimensional change in a Fabry-Perot cavity. This

change is accurately measured by a remote detection system through an optical fiber.

The initial devices now being tested are in the bare silicon form, *i.e.* without glass packaging. Other strain gauges have been packaged and await fiber-optic packaging. Two sizes are available; the gauge lengths are 1 and 2 mm long. The 1-mm-gauge device is shown in Fig. 2. The silicon portion of the deflection gauge fabrication has been made, and it is shown in Fig. 3.

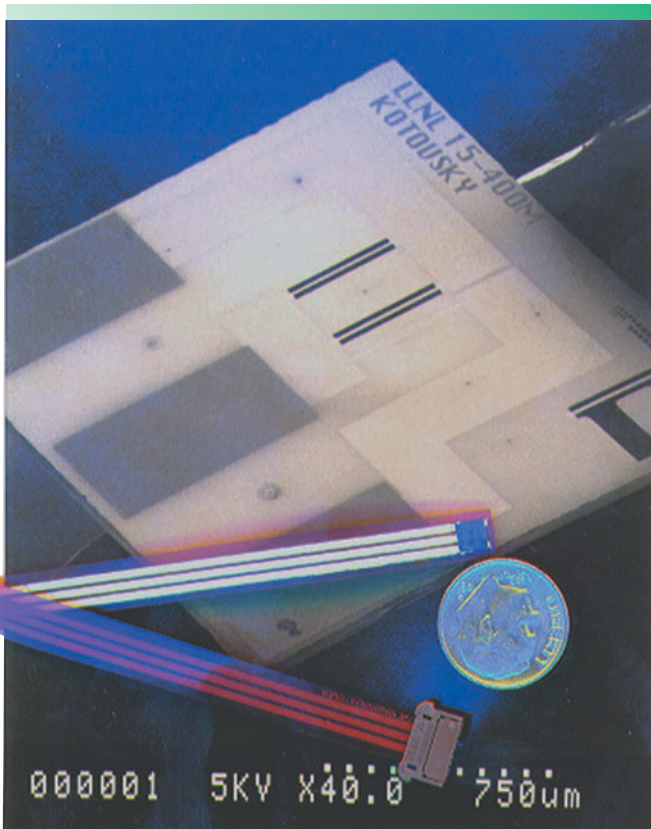


Figure 1. Photograph of mounted contact-stress sensor with flex connector, next to a dime. The device is sitting on an SEM image of a 55- μ m-thick silicon sensor.

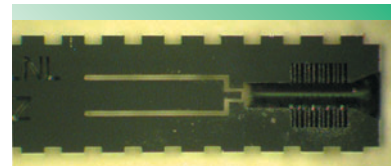


Figure 2. Prototype silicon fiber-optic MEMS strain gauge. The central horizontal pillar with the small end stub is the 1-mm gauge length. The channel awaiting optical fiber insertion and bonding is the dark trumpet shaped region on the right. The notches on the top and bottom sides are for more firmly attaching the sensor with epoxy to the object whose strain is to be measured.

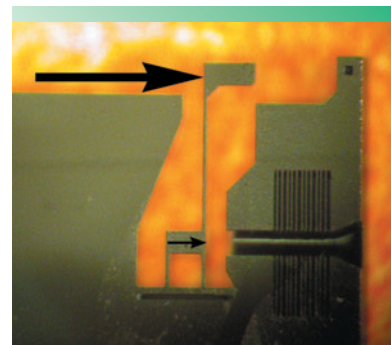


Figure 3. The active end of the silicon portion of the prototype deflection gauge. The not-yet completed device will incorporate an external leaf spring that will actuate the silicon compound lever, as shown by the large arrow. This will result in a small motion, shown by the small arrow, of a movable Fabry-Perot mirror. The mirror motion of about 10 μ m will be read by an optical fiber.

High-voltage photo-voltaic arrays have been identified as possible components of advanced firesets for DOE and DoD applications. Gallium arsenide (GaAs) is preferred over silicon, due to its higher efficiency at converting light into electricity.

Early attempts to take advantage of IC mass production techniques by fabricating arrays of photodiodes on a single substrate have met with limited success due to the leakage of electric current through the substrate. Electrical barrier layers between the GaAs substrate and the photodiodes on the surface have failed to provide enough electrical isolation. Arrays generating voltages in excess of 800 V have been demonstrated by adhesively mounting an array of lower voltage photodiodes onto a glass insulator, then using a wafer saw to create isolation trenches between the photodiodes, and finally wire bonding the photodiodes together. However, while all steps of such a process are manufacturable, such a technique may not be consistent with a low-cost IC fabrication process.

Thin layers of silicon bonded to insulators without the use of adhesives have been commercially available for many years. However, we have been unable to identify commercial sources of GaAs bonded to insulating substrates, and working processes have not been published in sufficient detail to easily replicate. It is clear from the published reports that the surface roughness of the materials to be bonded is a critical parameter. RMS surface roughness over a $2\text{-}\mu\text{m}\times 2\text{-}\mu\text{m}$ area is often specified to be less than 0.2 nm.

Another parameter that is important if the bonded materials are going to be exposed to elevated temperatures is the coefficient of thermal expansion (CTE). If there is a significant difference between the CTE of the GaAs and that of the insulator to which it is bonded, substantial strain can develop when the bonded pair

Direct Bonding of Gallium Arsenide to Sapphire

G. A. Cooper, N. R. Raley, V. R. Sperry, J. J. Muyco

We have initiated an effort to add a gallium-arsenide-to-sapphire bonding process to our technology base. We have measured the effect on surface roughness of several possible pre-bond processes. All of the processes examined show promising results.

is heated, leading to possible cracking and debonding. Sapphire has a relatively good CTE match to GaAs and can be obtained in thin, polished wafer form suitable for bonding.

Prior to any attempt to realize a GaAs-on-sapphire bonding process at LLNL, it is necessary to examine the surface roughness of the starting materials and determine how that roughness may be degraded by any pre-bond treatments. We have measured the RMS surface roughness on four wafers of GaAs: 1) as procured;

2) after heating for 10 min at $720\text{ }^{\circ}\text{C}$ in an arsine/ H_2 flow; 3) after $7\text{ }\mu\text{m}$ of epitaxial growth; and 4) after a wet cleaning process consisting of solvent clean, oxygen plasma treatment, and 20% hydrochloric acid dip.

The RMS roughness after each of these treat-

ments is shown in the table. The terraced crystalline surface of the GaAs wafer after arsine/ H_2 treatment is shown in Fig. 1.

We have also measured the surface roughness of two sapphire wafers, as procured, and after heating to $500\text{ }^{\circ}\text{C}$ in hydrogen gas. The RMS roughness for these two samples is shown in the table. The data exclude particles that were attracted to the wafer surface. Figure 2 shows the topography of the sapphire surface after the heat treatment in hydrogen, and includes a couple of particles.



RMS surface roughness for GaAs and sapphire as received and after various prebond treatments.

Material	Treatment	RMS Roughness (nm)
GaAs	As-Received	0.20
GaAs	Arsine/ H_2 @ $720\text{ }^{\circ}\text{C}$	0.10
GaAs	$7\text{-}\mu\text{m}$ epitaxial growth	0.30
GaAs	Wet clean, oxygen plasma	0.24
Sapphire	As-received	0.21
Sapphire	H_2 @ $500\text{ }^{\circ}\text{C}$	0.11

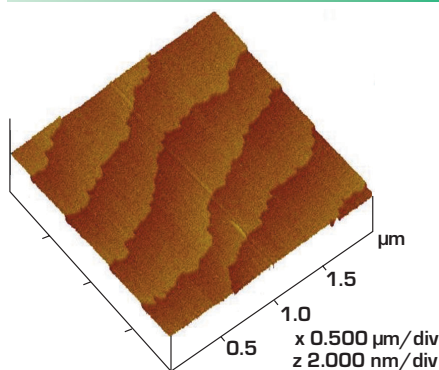


Figure 1. Surface topography of GaAs wafer after arsine/ H_2 heat treatment. The vertical scale is magnified 250x compared to horizontal scale.

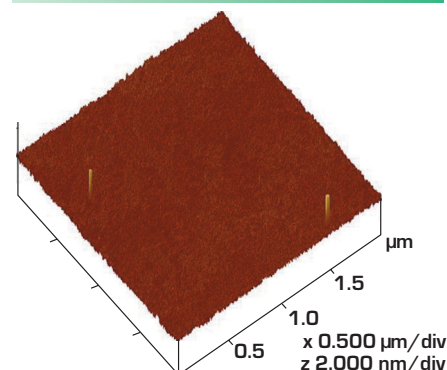


Figure 2. Surface topography of sapphire wafer after H_2 heat treatment.

Microfluidic devices typically have limited optical access; therefore, an epifluorescent microscope is used to illuminate a volume of fluid in the device. As a result, particles away from the object plane, but within the depth of focus, still contribute to the correlation peak, and can introduce a bias into the measurement. This effect is increased in shallow channels where vertical velocity gradients are high. To address these issues and to improve accuracy and resolution, new image processing algorithms were integrated into one software package.

In addition to unfocused particle images, particles that intersect correlation zone boundaries contribute to the bias error, due to the signal loss by the truncated particle images. This error dominates when correlating with small zones to obtain a high spatial resolution since a large fraction of the particles lie on the boundary. Incorporating a mask filter to remove these unfocused and boundary particles reduced the error by

Image Processing for Analysis of Microfluidic Systems and Biological Assays

T. H. Weisgraber

Effective diagnostic tools are essential to study microscale flows and characterize the performance of microfluidic systems. Digital particle image velocimetry (DPIV) is a measurement technique that combines fluorescent imaging and specialized correlation algorithms to accurately determine instantaneous, spatially-resolved velocity fields in a noninvasive manner. Though the application of DPIV to macroscopic flows is well established, enhancements such as those made in this technology-base project are required to measure flows in micrometer-sized channels.

as much as 20%, with little impact to the processing time. Pre-processing steps were also introduced to remove background noise and compensate for inhomogeneous lighting conditions.

To improve resolution, a particle tracking velocimetry (PTV) algorithm was integrated with the DPIV capability. In this hybrid approach, the initial velocity field was estimated with a few DPIV iterations using grid refinement. PTV further refined the measurement with a tunable match probability algorithm to determine the corresponding particle pairs between two images.

Whereas the resolution for DPIV is determined by the correlation zone size, the PTV resolution depends on the particle seeding density of the flow. In addition to improving the resolution, PTV obviates the need for special handling of complex boundaries. This adaptive scheme was demonstrated by characterizing the flows through arrays of micro-fabricated pillars and in the disposable PCR device. The measure-

ments in Figs. 1 and 2 validated the flow predicted by computations.

As a stand-alone capability, PTV can be adapted to discriminate between labels in particle-based immunoassays for pathogen detection. The particle detection algorithm is not limited to spherical shapes and can also identify the nano-barcode rods, currently being worked on for a multiplex assay. In addition to measuring velocity, the new PTV capability can also quantify the shape and rotation rate of particles.

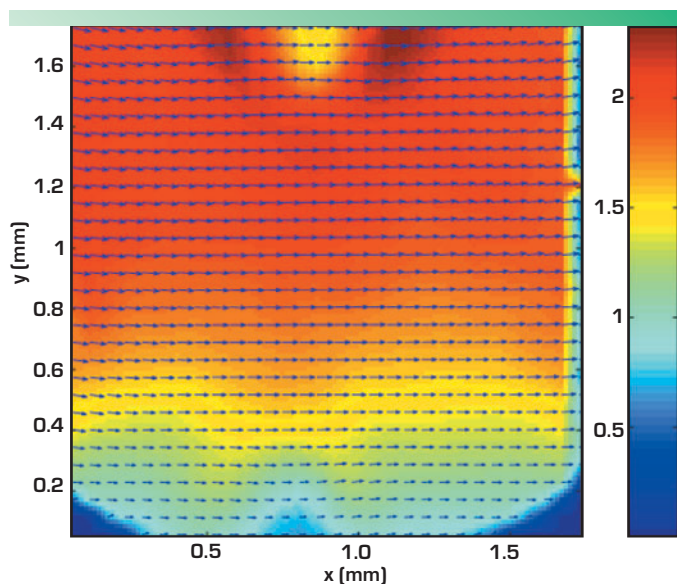


Figure 1. Pseudo-color plot of velocity in the detection window of the disposable PCR device.

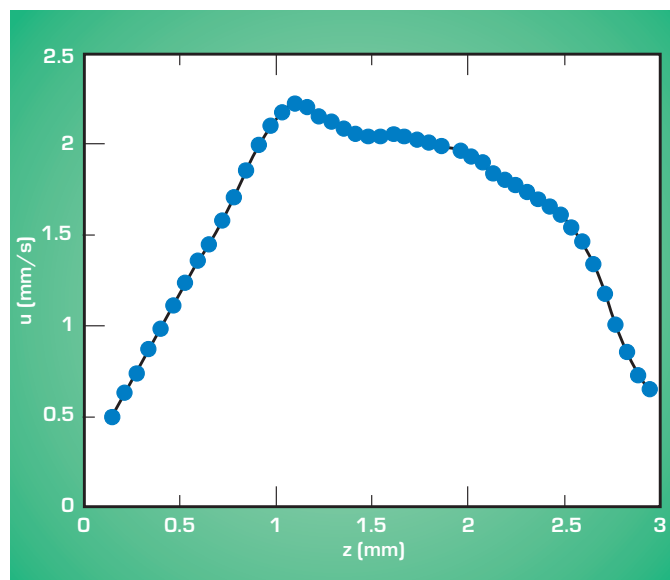


Figure 2. Velocity profile across the detection window.

Due to space constraints, miniaturizing the measurement system, not just the sensors, is essential to the success of the microsensors project. Since some sensors can make measurements at kHz rates, a several-kHz multichannel/multiplexed processor is required, exceeding capabilities of existing commercial devices. Commercial multiplexers may not have the bi-directionality, the bandwidth, or the speed required for our applications.

Previously we built a single channel processor that was approximately the size of a 9-V battery. We also generated concepts for further miniaturization and multiple-channel operation. The final focus of this project was to reduce-to-practice and build a three-channel processor based on these concepts. Our focus changed during the year as funding and programmatic goals changed, and occasionally overlapped our project goals.

We also began a low-level effort to collaborate with a NASA team to reduce-to-practice a miniature MEMS incandescent light source for future use in an absolute measurement processor.

Building on our highly successful single-channel, In-Phase-and-Quadrature (I/Q) measurement technique, we have

Multichannel Fiber-Optic Processor/Multiplexer

M. D. Pocha, C. F. McConaghy, G. A. Meyer,
J. D. Wolfe, T. Lavietes

High-fidelity flight tests are required by LLNL's Stockpile Stewardship mission, and these tests require miniature, minimally-invasive sensors. Sensors also need to be optically read out to reduce exposure of sensitive components to electrical energy. We have established a Microsensors Program to enhance our engineering infrastructure, and to reduce-to-practice miniature optical sensors. Several different sensors are being used to measure parameters such as acceleration, strain, displacement, pressure, and temperature.

almost completed the implementation of a three-channel miniature processor (see figure). We have refined our original concept that consisted of several layers of silicon and glass to a single glass block optical path.

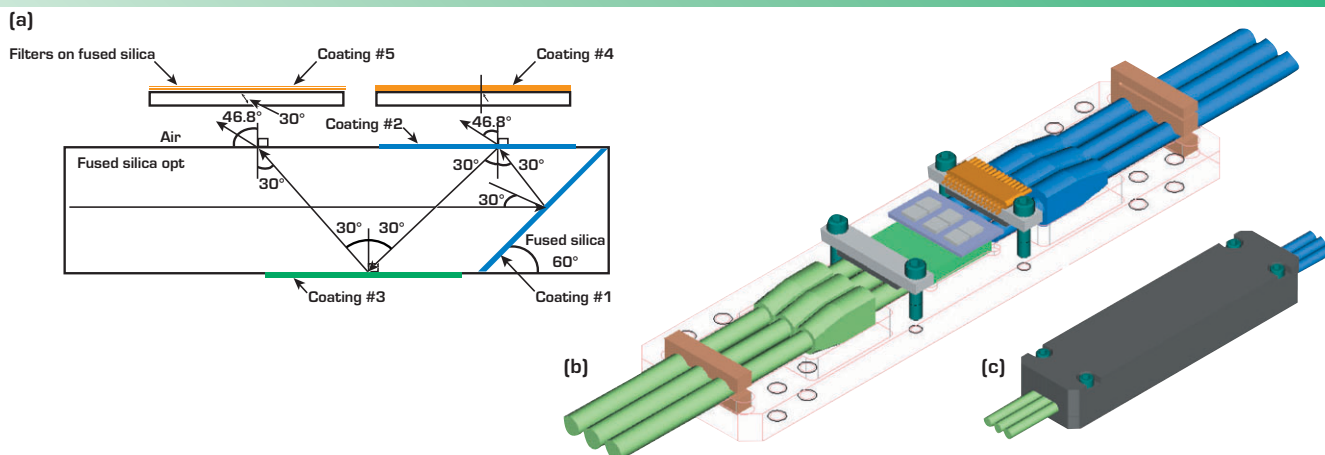
We also solved a number of fabrication and packaging problems to get the overall three-channel package size down to 8 cm x 2 cm x 1.2 cm. This is about 50% longer than our previous single-channel implementation (required due to strain relief for fibers, which the original did not have), but is about 40% smaller in height and width. This is a substantial improvement in overall volume.

One of the key problems was the need for a pair of thin optical filters with precise bandpass and center wavelength to give us quadrature phase detection. We were able to use a commercial thin-film simulation package to generate a theoretical structure, only a few mm thick, for

these filters. The overall filter becomes about 0.5 mm thick with its substrate. We [J.W.] demonstrated experimentally that the structures could be built. We could not actually build them, because LLNL does not have the correct precision hardware in its deposition systems. A commercial vendor is building the filters for us.

Several components are on order from vendors; however, it is not likely that we will be able to complete the assembly this fiscal year. We will be seeking funds for continuation of this project into FY04 to complete the assembly, test, calibrate, and evaluate performance of the instrument, and to perform any design modifications needed as a result of the evaluation.

We have begun the collaboration with NASA. They have built and sent us several component parts of a miniature filament incandescent source. We plan to use the capabilities of LLNL's Microfabrication Laboratory, and Vacuum Processes Laboratory to assemble these components and hermetically seal them to implement a miniature sealed source of broadband fiber-coupled light for use in a future absolute measurement fiber-optic processor.



Three-channel miniature processor with overall dimensions 8 cm x 2 cm x 1.2 cm. (a) Sketch of optical path; (b) assembly drawing without cover; (c) with cover.

Presently, the most common techniques for DNA separations are performed with fluorescent labels using capillary electrophoresis (CE) to sequence the samples of interest. While this technique provides excellent sensitivity and is amenable to four-tag detection, fluorescent detection involves optics and lasers that are relatively expensive, and difficult to miniaturize.

Electrochemical detection techniques offer the potential of high sensitivity, low cost, and simple integration.

The use of electrochemical detection has previously been demonstrated using redox-active molecules in DNA hybridization studies, and for detectors in capillary gel electrophoresis. While these techniques have exhibited excellent sensitivity, they have not been applied to homeland security. Our effort is specifically looking at the use of custom patterned electrode materials that can be directly integrated with CE devices for evaluation against the more proven fluorescent detection techniques.

Electrochemical detection has advantages over traditional fluorescence detection: it can be sized easily to microscale dimensions, and the cost and reliability of such devices is not compromised in this arrangement. Amperometric detection of the redox-active commercial eTag™ can be used, or the eTag™ can act catalytically to

Nanoelectrodes for Electrochemical Detection of Biological Pathogens

D. A. Sopchak

Separation and detection techniques are essential for identification of DNA fragments for a variety of applications, including drug discovery, DNA sequencing, and pathogen detection. Electrochemical detection techniques offer the potential of high sensitivity, low cost, and simple integration, which would greatly reduce the cost of packaging and increase the ruggedness of a detection system

enhance, or be used to block the signal from a redox-active species present.

If the use of conventional electrode materials, such as noble metals, proves problematic due to corrosion or fouling at the small scales used, there exist other electrode materials, such as tetrahedral amorphous nitrogen-incorporated carbon (taC:N), which are more robust and provide better signal-to-noise ratio than conventional electrode materials. Materials such as taC:N can be made at LLNL and patterned into desired electrode patterns using equipment already available.

After considering various approaches, it was decided that the first attempt in this project would involve the following testing protocol:

Part 1: eTag™ recognition of target DNA;
Part 2: CE of eTag™ reporters;
Part 3: electrochemical detection of electrochemically active eTag™ reporters.

For Part 1, three anthraquinone derivatized eTags™ were obtained.

Part 2 will ultimately involve a commercial CE detector. For initial tests, a simple plug-flow syringe set-up will be used to mimic the CE apparatus and the travel of the eTag™ reporters through the fluid medium.

For Part 3, we are currently fabricating a MEMS-based electrochemical eTag™ detector device, sized to fit a CE apparatus. This device is made of a silicone rubber flow channel

bonded to a silicon substrate, with gold counter and working electrodes, a silver/silver chloride reference electrode, and inlet and outlet fluid ports. Initial testing will involve plug-flow testing of anthraquinone and hydroquinone at micro-molar levels in the borate-based CE buffer solution. The analyte passes the working electrode, the latter poised at (in this case) a potential sufficient to oxidize the former. This results in an anodic current generated by the device and signals the detection of the analyte.

Assuming the initial plug-flow tests go well, one of the anthraquinone-based eTags™ will be tested in a like manner. If this shows good results, the electrochemical detection devices will be integrated into a CE cartridge and tester. This tester is also equipped with ultraviolet and fluorescent detectors, which will allow for simultaneous electrochemical, fluorescent, and ultraviolet detection of species and the relative sensitivity of each method.



Our micro- and nano-mechanical tools allow one to map out the local *in situ* morphology and inter-granular, inter-particulate, or inter-molecular deformation fields in materials that are subjected to local mechanical stresses. Nano-scale stress-strain data would be obtained which would allow the characterization of localized constitutive models. Load/deformation fields in the vicinity of crack tips

in materials could be used to characterize and validate various localized fracture mechanics models.

In addition, the small-scale deformation stages can be used to characterize the strength of micro- and nano-scale reinforcements (small samples of material where traditional large specimens cannot be obtained), and the adhesive bond strength of small joints.

An accurate understanding of the relations between material morphology, deformation, and fracture will provide critical information for enhancing our ability to model the macroscopic response of all materials in general. It is anticipated that a significant amount of small-scale testing would be performed on metals in

Nano-Mechanical Characterization Tools for *In-Situ* Deformation and Morphology of Materials

S. E. Groves, M. W. McElfresh, S. K. McCall

We are working with a suite of micro-/nano-mechanical deformation test stages that can be incorporated into both a scanning electron microscope (SEM) and an atomic force microscope (AFM) for the purpose of providing micro- and nano-scale experimental data in support of material characterization and modeling efforts.

support of the plethora of multi-scale modeling efforts underway. With organic materials, like plastic-bonded explosives used in the nuclear stockpile, an accurate representation of the local granular morphology does not exist; nor do we know how this morphology, when stressed, affects local deformation and fracture. New efforts are underway at LLNL to characterize the mechanical response of biomaterials, including living cells. The ability to image and map *in situ* deformations for any of these material systems will be invaluable.

To accomplish this task, we purchased a nano-positioning stage with controller that functions within the ultra-high vacuum and space limitations

required in our SEM. This stage has a total of 200 μm of motion with approximately 10 lbs of force capability. It is expected that additional stages will be needed to accommodate higher deformation or loading conditions. One of the critical components to the success of this effort has been and will continue to be the gripping methods and specimen configurations required for testing a variety of

materials at the micro-/nano-scale. Figure 1 shows our deformation stage and our first iteration of mechanical grips and specimen. The grips and specimens have been fabricated at LLNL.

We were able to demonstrate as an integrated system that we could fail a ductile Al tensile specimen with a stress concentrator (Fig. 2). Based on our first results, we have plans for the next grips and specimens, which will be easier to fabricate and require less precision to make (Fig. 3). We have also finalized a method for measuring load in our miniature grips using semi-conductor gages.

In FY04 we plan to test a variety of materials to demonstrate the new system. In addition to the SEM, the system will be coupled with an AFM for measuring the change in morphology at crack tips and grain boundaries. To complete the system some form of local strain measurement will have to be implemented.

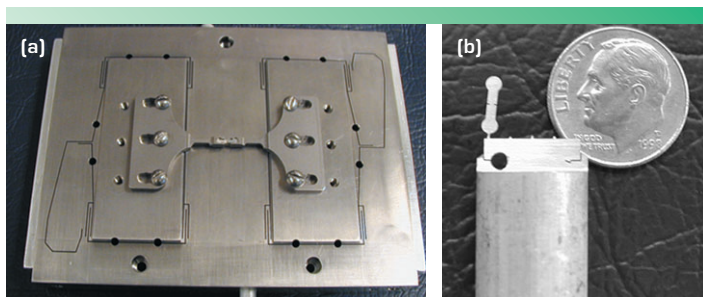


Figure 1. (a) Nano-stage with 200 μm of motion and 10 lbs force capacity. (b) First tensile fracture specimen.

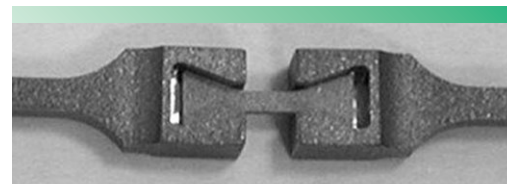


Figure 3. Wedge grip specimen configuration.

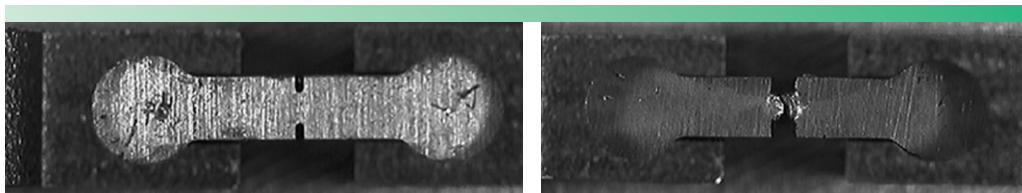


Figure 2. Successful tensile failure of 6061 Al specimen.

Integrated microsystems applications require small, low-cost, rugged, field-operable devices. To address these issues, we have conceived of a polymer-based platform that will lead to hybrid microsystems with integrated sensors, electronics, optical elements, power, and microfluidics. The platform is capable of incorporating off-the-shelf components as well as custom fabricated devices, and features a low-cost packaging approach.

PDMS serves as the integration backbone, with microfluidic structures molded into the silicone polymer, and other components such as silicon sensors and circuits directly bonded to the PDMS, forming a leak-proof seal. Electrical traces are patterned on the PDMS to interconnect the various components.

We have deployed and demonstrated several aspects of this technology, including stretchable electrical traces on PDMS, bonding of silicon chips and small batteries to PDMS, and two-level electrical interconnects. We have begun to deploy and characterize manufacturable PDMS-based processes that will create a new capability for LLNL, and enable us to generate a broad range of integrated microsystems for many applications.

Our first year efforts to deploy and measure manufacturable PDMS-based processes were focused on conductive ink printing on PDMS and on multilayer

Polymer-Based Manufacturing Processes for Hybrid Integrated Microsystems

J. C. Davidson, P. Krulevitch, M. Maghribi, J. Hamilton

Integrated microsystems will play an increasingly important role in homeland security applications. Examples include microfluidic systems for chemical/biological threat detection, distributed sensors for tracking terrorist activities, radiation detectors, and cargo-container monitoring devices. We have demonstrated methods for screen-printing of conductive inks for single and multilevel metalization on polydimethylsiloxane (PDMS). The methods provide the basis for further deployment of PDMS-based hybrid microsystems integration. These initial enabling processes are now being used in support of LLNL's in situ sensing effort and DOE's Artificial Retina Project.

interconnects. These two core processes provide the basis for using PDMS as a "superstrate" for integrated fluidics and electronics.

Initial evaluation of screen-printing conductive ink on PDMS required measurements on multiple conductive inks and vendors. A conductive silver ink composed of a polyester carrier and 71% solid content was determined to be chemically compatible with PDMS. Thin PDMS films, on the order of 50 μm thick, were made primarily on gold-coated glass. Gold serves as a release layer to permit removal of the film.

Characterizing screen-printing involved many variables, including squeegee angle, offset height, durometer, speed, and pressure. Detailed evaluations of these parameters were performed using the services of an outside vendor. Upon optimizing these parameters for pliable PDMS

substrates, we attained the vendor-specified sheet resistance of 0.02 $\Omega/\text{sq}/\text{mil}$. We also demonstrated linewidth print control down to 80 μm , surpassing our original target of 100 μm (see Fig. 1).

As a further demonstration of the use of PDMS as a substrate for hybrid systems integration we coated screen-printed conductive ink traces with an additional layer of insulating PDMS. This passivation layer successfully adhered to the base layer of PDMS and trace conductivity was maintained.

Hybrid integration on a PDMS also requires multilevel metalization. To this end our efforts also focused on the deployment of a screen-printing alignment apparatus and process. We successfully demonstrated an approach to align to first level and subsequent levels of metalization. A photograph of screen-printed filled 400- μm -diameter vias is shown in Fig. 2 (a).

Another approach was demonstrated whereby vias were filled with conductive ink using pin deposition (Fig. 2(b)). A micro-needle was used to uptake conductive ink by dipping and then depositing it in the vias. Transfers were demonstrated down to approximately 100 μm in diameter. A variation of this approach using positive pressure to extrude the ink also proved successful.

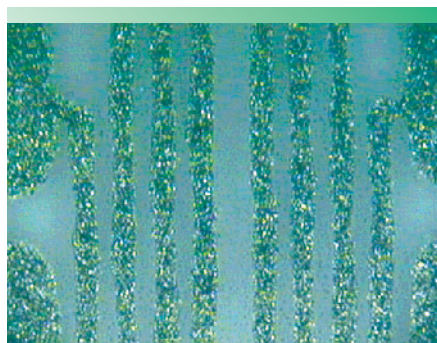
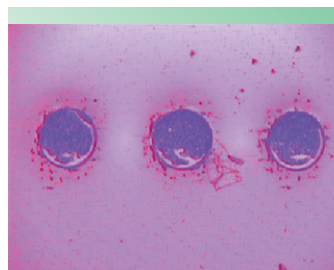
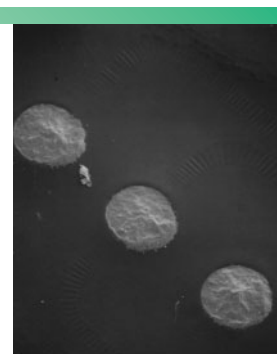


Figure 1. Demonstration of screen-printed conductive ink traces on PDMS.

Figure 2. Demonstration of two methods evaluated for via filling, required for multilevel metalization using conductive ink.



(a) Screen-printed via fill.



(b) Pin-deposited via metal.

The approach taken here uses the known, differing functional dependences of electro-osmotic and electrophoretic mobilities on temperature to uniquely balance a charged species' individual velocity components,

$$(u_{\text{electrophoresis [EP]}} + u_{\text{electroosmosis}} + u_{\text{pressure}} = 0)$$

at a particular temperature, shown schematically in Fig. 1. When performed in the presence of a temperature gradient, the sample focuses to a particular location while diffusion continually smooths out and broadens the focusing band.

A photograph of the fabricated and tested device is shown in Fig. 2. Thermal gradients of approximately 40,000 °C/m along the microchannel are characterized and depicted in Fig. 3, using a quantitative optical temperature measurement

Temperature Gradient Focusing

E. K. Wheeler, K. D. Ness

Recent advances in the field of proteomics are derived from biologists' ability to study and manipulate intracellular components using various instruments. Further optimization of current technologies and the creation of new instruments to manipulate biomolecules are necessary to accelerate the unraveling of the age-old question: what is life at its most fundamental level? Deployment of an instrument for simultaneous purification, concentration, separation, and focusing is the scope of this project, with a final deliverable of a new tool for biomolecular manipulation.


technique based on the calibrated temperature-dependent quantum yield of different fluorescent dyes.

An automated image-processing algorithm and accompanying MATLAB code were used to perform rapid image registration, image correction, data reduction, calibration-curve generation, and data analysis, for both temperature measurements and temperature gradient focusing (TGF) experiments.

Successful focusing of 1 μM fluorescein with an electric field of 70 V/cm

and an applied pressure gradient of 170 Pa/m in a 900-mM boric acid/900 mM Tris buffer solution with a 60 °C temperature gradient (80 °C left, 20 °C right), is shown in Fig. 4. The focusing peak has a signal-to-noise ratio of 170. The raw focusing images shown were acquired approximately 5 min after the voltage was applied.

The test device, image analysis code, model, and characterization platform comprise the capability enhancement package deliverable of this project for the application of TGF to various LLNL missions.

Sample TGF applications are front-end sample preparation and PCR inhibitor purification for nucleic-acid-based bio-warfare detection instruments, and a third dimension for protein separations that is different from capillary electrophoresis and isoelectric focusing. 

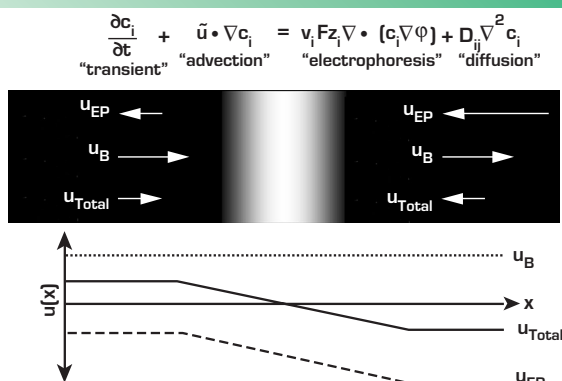


Figure 1. Governing equation and schematic of principles behind TGF. A balance is obtained between electrophoresis and the bulk flow at a specific temperature.

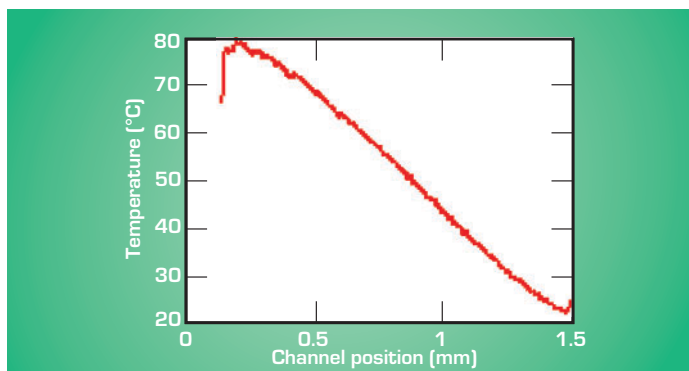


Figure 3. Temperature profile along microchannel characterized using quantitative fluorescent imaging techniques.

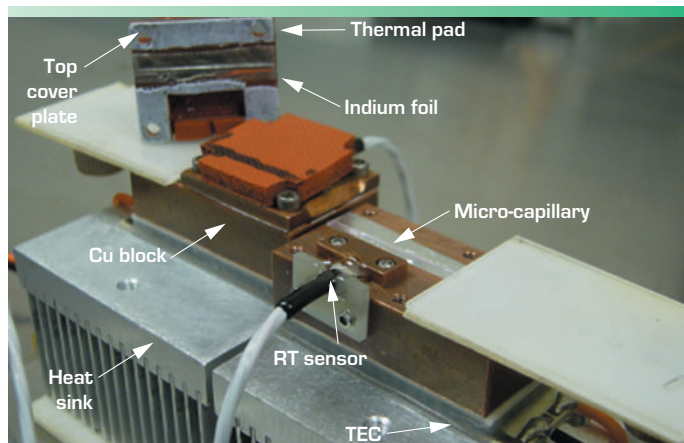


Figure 2. Photograph of the device used to produce a stable temperature gradient along a microchannel.

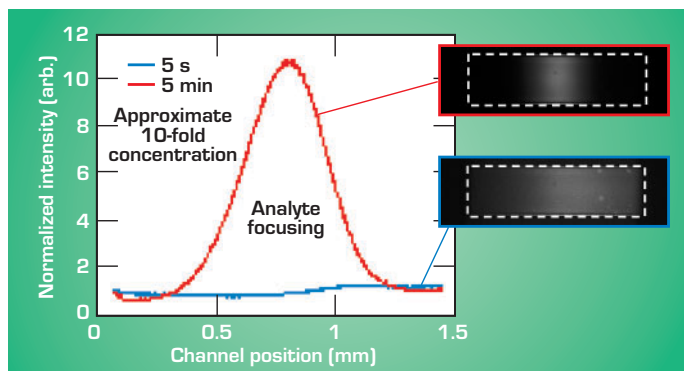


Figure 4. Measured focused peak using TGF. A concentration of ~10 fold is observed in 5 min with raw images shown on the right using fluorescein as the dye species.

Twelve years ago, LLNL's Micro-electronics Program developed a quasi-3-D laser direct writing tool, called Laser Pantography, to fabricate metal interconnects on multichip modules. In addition, this tool, together with associated deposition and etching processes, allowed the program to make unique mm- and sub-mm-scale parts such as RF inductors, diamond anvils with electrode structures, NMR microcoils, micromotor stators, and magnetic relays.

The Laser Pantography tool had fundamental limitations, however, and because of the original multichip module application and limitations in the CAD/CAM systems of the time, the configuration could not support out-of-plane patterns more complicated than straight lines of fixed length parallel to the z-axis. Also, the workstation was out-of-date, using an operating system no longer supported.

Another limitation was that motors could not be started at exactly the same time. This meant that diagonal lines in the x-y plane, to use a simple example, were executed as stair steps. A modern motor control system would allow simultaneous movement of multiple stages so that smooth diagonals, ovals, and other shapes could be drawn.

These limitations have been addressed in this technology-base project.

We are assembling a modern, fully 3-D, sub- μm -accuracy motion system driven by a commercial CAD/CAM package. This 3-D microlithography system (3D MLS) functions as a five-axis milling machine with a focused laser as the "cutting tool." The laser does not actually cut; it exposes a photoactive substance such as photoresist, to create the desired pattern.

With improvements in the optical system, the "cut size" can be 1 μm . The upgrade of the 3D MLS will involve the replacement of the original custom hardware and software with a standard motion-control hardware package,

Three-Dimensional Microlithography System

V. Malba, A. F. Bernhardt, L. B. Evans, C. D. Harvey

We are creating a unique lithography tool capable of patterning 3-D surfaces at micron dimensions. Unusual micro-electromagnetic and micro-electromechanical structures can be created using this tool.

together with commercially available 3-D CAD/CAM software, which is licensed to LLNL. The new software will output standard G-code, which the new hardware will be able to execute in the same fashion as a five-axis milling machine.

A true 3-D microlithography system will be the final product. It will be a unique capability, and is expected to generate considerable interest and funding. It will dramatically increase the 3-D patterning capability of the present system, making it applicable to surfaces and structures that cannot now be patterned. As technology demonstrations, we will pattern helices on < 400- μm -diameter cylindrical surfaces (for NMR and MRI applications) and simple periodic structures on spherical or elliptical surfaces of radius of order 1 mm.

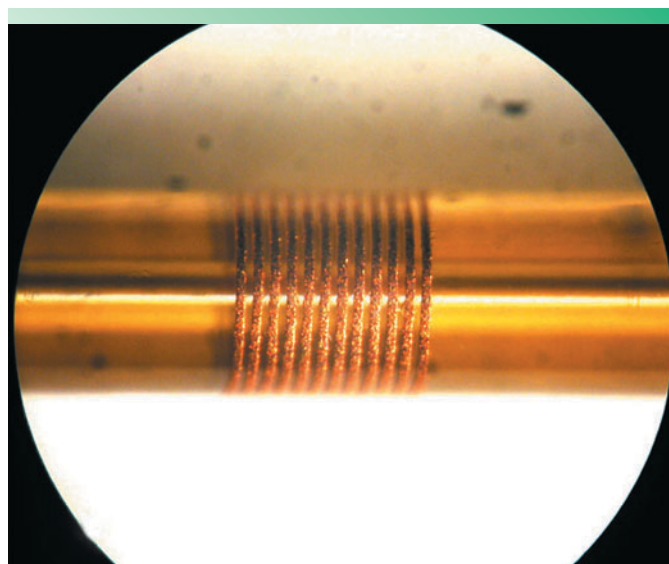
In FY02 we installed new motion-control hardware, including motor amplifiers and motor controllers for up to eight degrees of freedom. A 3-D CAD/CAM package was installed, and

initial handshaking software linking it to the motion-control hardware was installed. X, y and z translation stages (existing equipment) were installed and wired. Requirements for high-precision theta in x- and z-axes were ascertained, and stages with sufficient

speed and precision were identified and purchased. A high-power UV argon-ion laser was procured internally and was refurbished. An optical system emphasizing a small focal spot, which can be expanded for rapid patterning of large areas, was completed, and the required components identified.

In FY03 we completed the motion system with two rotation stages. An initial version of a Visual Basic GUI front end for the PC was written. We assembled a new optical system (e.g., objectives and tube lenses), which is more versatile.

Fixturing for various workpieces is also a significant issue when precise knowledge of the exact position of the part is required. We have made significant progress on holding 360- μm -diameter flexible tubes on which NMR coils are fabricated. We are now confident of our ability to fabricate 100- μm -diameter NMR tubes for DOE and DHS in the coming year.



Twelve-turn coil patterned on 360- μm -diameter capillary.

The process for fabricating silicon field-emission cathodes (FECs) is illustrated in Fig. 1. The fabrication steps include 1) forming Cr/insulation mask patterns having 2- μm diameter; 2) isotropic etching of silicon that undercuts below the Cr/insulation mask caps; 3) thermal oxidation of silicon to form the tips; 4) deposition of metal gate layer; 5) removing Cr/insulation mask caps and

X-Ray Cathode Detector

J. D. Morse, K. Lui, D. R. Ciarlo, H. E. Petersen

Advanced diagnostics require detectors sensitive to the 10- to 20-keV x-ray spectrum. These detectors will make up an imaging array that is then coupled to a streak camera. The required temporal response of the x-ray detector is 500 ps. The device being deployed for this effort is a solid-state x-ray detector, with a field-emission cathode to convert electron-hole pairs generated by the absorbed x rays to electrons emitted into vacuum. The focus of this year's effort has been the fabrication and testing of a gated field emission array suitable for integration with a 10- to 20-keV x-ray detector.

etching back silicon dioxide to expose the silicon tips.

The implementation of the FEC using a field-emitter array for an x-ray photocathode is illustrated in Fig. 2. A SEM image of a gated silicon field-emitter array fabricated by the process in Fig. 1 is shown in Fig. 3. The gate-to-tip spacing is on the order of 1 μm . The resulting field-emission current as a function of the applied gate voltage is presented in Fig. 4 for a 1-mm² active-area array having nominal 3- μm tip-to-tip spacing.

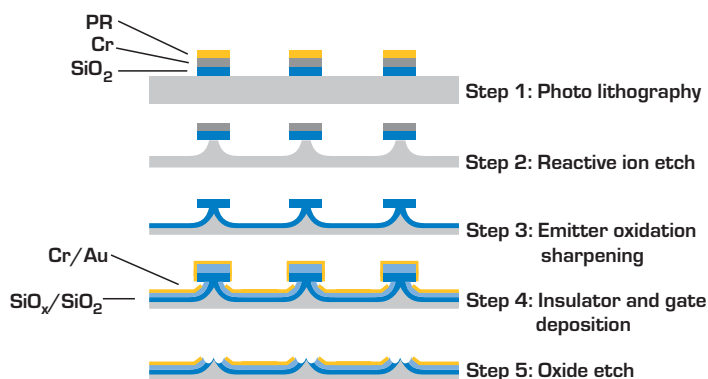


Figure 1. Microfabrication sequence for FEC arrays.

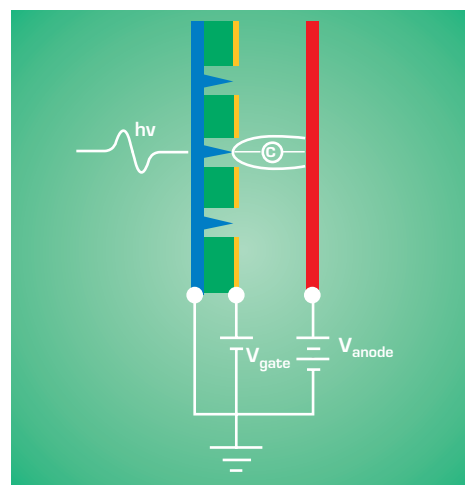


Figure 2. X-Ray cathode implementation using FEC array.

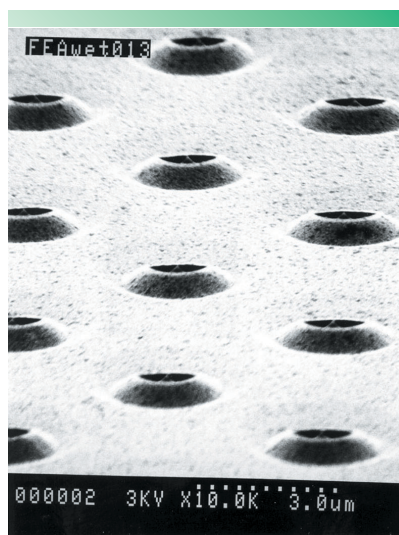


Figure 3. Gated silicon FEC array fabricated at UNL.

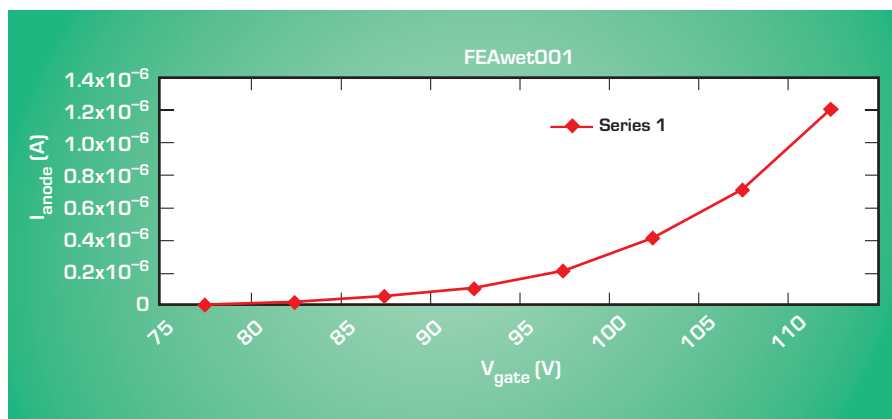
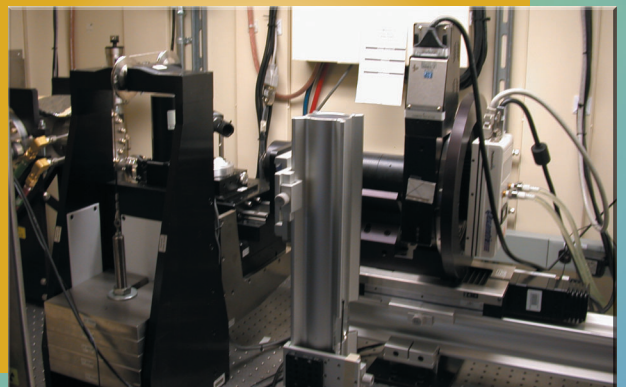
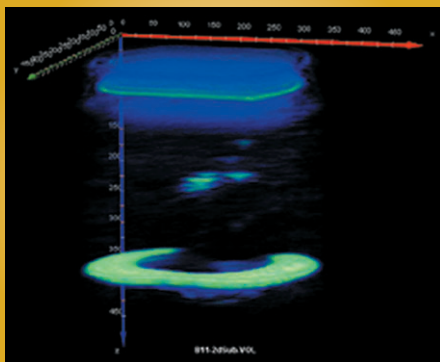
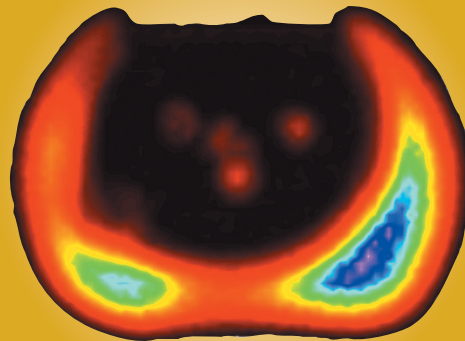
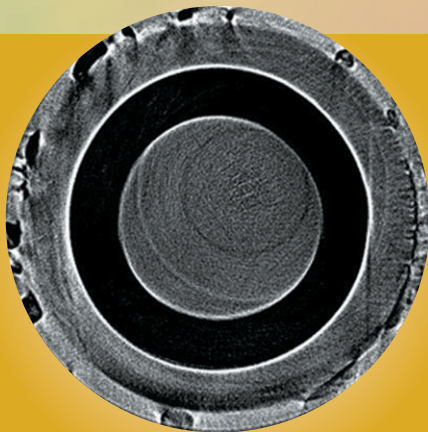
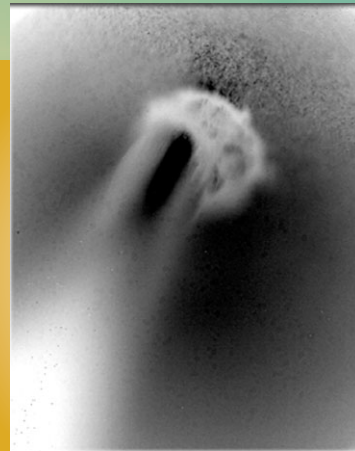
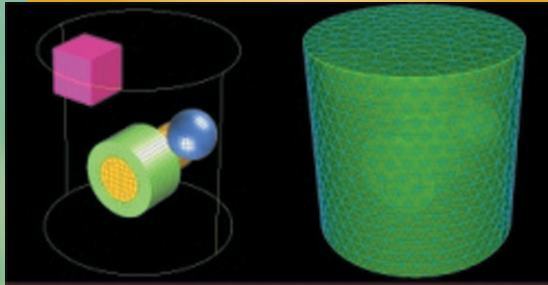


Figure 4. Turn-on characteristics for gated silicon FEC.

Center for Nondestructive Characterization



Engineering finite-element analysis models are typically used to evaluate component designs and to predict the results of test scenarios. Most finite-element analysis models are currently built using idealized object design specifications, and do not take into account material flaws (including cracks, voids and inclusions) or geometric irregularities (including warping) which exist as a result of materials and manufacturing processes and service conditions.

Even though the most accurate representation of the object is desired, the additional steps required to detect, identify, and model material and geometry deviations in the object's "as-built" configuration are currently too time-consuming and difficult for most applications.

In FY03, we generated a preliminary roadmap linking all the key steps between the initial evaluations of an object using nondestructive evaluation (NDE) techniques such as x-ray CT and acoustic tomography, through to the

Coupling of Nondestructive Evaluation and Finite-Element Analysis for Numerical Analysis

E. J. Kokko, D. J. Chinn, H. E. Martz, R. M. Sharpe,
D. H. Chambers, S. J. DeTeresa

We have generated a preliminary "roadmap" linking all the key steps between the initial evaluations of an object using nondestructive evaluation (NDE) techniques through to the analysis itself, using engineering finite-element codes at LLNL.

analysis itself, using engineering finite-element codes at LLNL.


Key steps in our as-built modeling process roadmap include multi-modal and multi-source NDE data collection; image reconstruction and artifact removal; multi-modal NDE data fusion; image segmentation; feature extraction (based on analyst requirements); mesh generation; and object analysis using finite-element codes (structural, electromagnetic, and thermal).

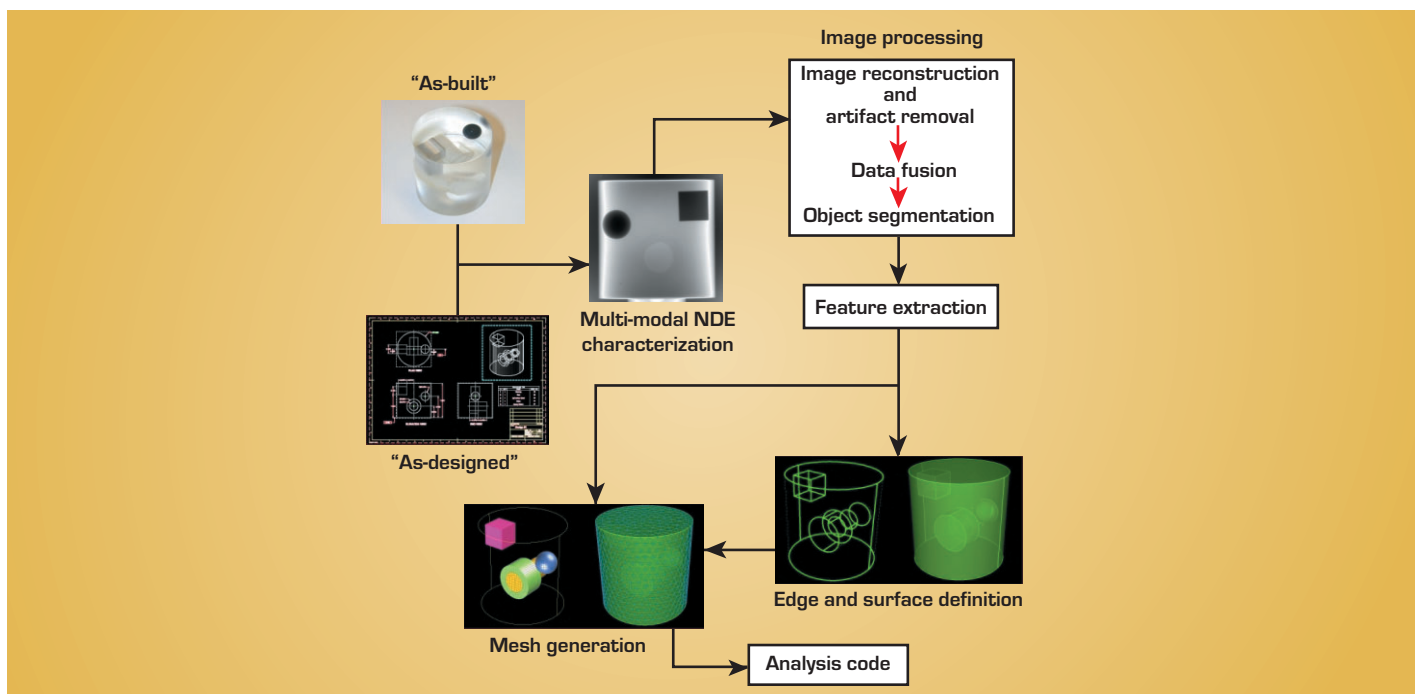
Identifying specific techniques within each key step to use for specific classes of analysis is the crux of the problem. The ultimate project goal is to eventually semi-automate

the process by aligning and enhancing existing time-saving tools and techniques for each key step.

As part of the project, several test objects have been conceptualized, manufactured, and imaged using several NDE techniques. The NDE data sets that have been collected will be used in FY04 to test the

techniques that will be implemented for each of the key steps in the process (see figure). In FY04 we will focus on evaluating algorithms to correctly "fuse" multi-modality NDE data sets for as-built components; methods to extract desired features from images; and methods to translate image information into a form easily manipulated with LLNL analysis code pre-processors

The as-built modeling process leverages many of LLNL engineering core technologies, including computational engineering, digital image processing, signal processing, and nondestructive characterization. 



Flow diagram showing the required steps to generate as-built models from NDE data. A sample object with various features is used as an example.

As this technology-base project comes to completion, we have succeeded in the main goals we set out to achieve: we have deployed and applied a new NDE technology for LLNL that complements the existing methods, and we have succeeded in proving the method to programmatic customers who have since identified Sonic IR NDE as a requirement for their NDE tasks.

There remain areas where further deployment is warranted however, and we will seek opportunities to continue to deploy Sonic IR into a fully mature capability.

In brief, Sonic IR works by dynamically exciting the part being tested with an acoustic probe that is in physical contact with the part. Any resulting differential motion across a crack face creates heat by friction, and a high-speed IR camera images the transient temperature rise at the crack.

A typical experiment requires an input pulse of about 0.1 s, and the transient thermal image is acquired for about 1.0 s. The camera can image a large area, so point-wise scanning is not required. We have found that the method is generally applicable to most

Enhanced Capability for Sonic IR NDE

W. O. Miller, M. W. Burke, G. H. Thomas

This year, our Sonic IR effort progressed from the laboratory bench to useful applications, as we moved to general deployment of this new nondestructive evaluation (NDE) technology. In this final year of this technology-base project we have applied the knowledge and experience gained in the previous years, and have begun demonstrating the method on practical tests of programmatic interest. We have also established external collaborations and we are now internationally recognized as a lead deployer for Sonic IR NDE.

engineering materials, and works well on large and complex parts.

The effort for FY03 has focused on demonstration and practical applications. The following accomplishments are noteworthy.

Tube braze study. We created a series of samples with stainless steel tubes brazed into aluminum plates. Several brazes were intentionally of poor quality while others were of high quality to serve as reference standards. Sonic IR testing clearly identified poor brazes with localized flaws (Fig. 1). The samples were later subjected to dye-penetrant testing to verify the IR results. The two methods were in concurrence for surface flaws, although only Sonic IR could detect subsurface flaws.

DOE/LANL pilot test. We completed a series of tests to determine the

suitability of Sonic IR for detecting flaws in a composite material used in DOE and LANL facilities. The tests showed an excellent ability to detect damage (Fig. 2). As a result, Sonic IR is expected to be the NDE method of choice for part recertification testing.

HEPA hood. We have commissioned a hood for containing Sonic IR tests on hazardous materials.

The hood allows the camera and the acoustic stack to remain uncontaminated, so that these expensive items can be quickly reconfigured for nonhazardous tests. The hood is designed to attach to a HEPA filter to capture any airborne contaminants that may be created during testing, such as from minor surface abrasion. The hood will be delivered complete to LLNL in FY04.

External collaborations. We have maintained an active alliance with Wayne State University (WSU), which holds the initial patent on Sonic IR. We presented three papers on our work at two different conferences. We have been invited to participate in the first-ever session and working group devoted to Sonic IR at the 2004 SPIE Thermosense conference.

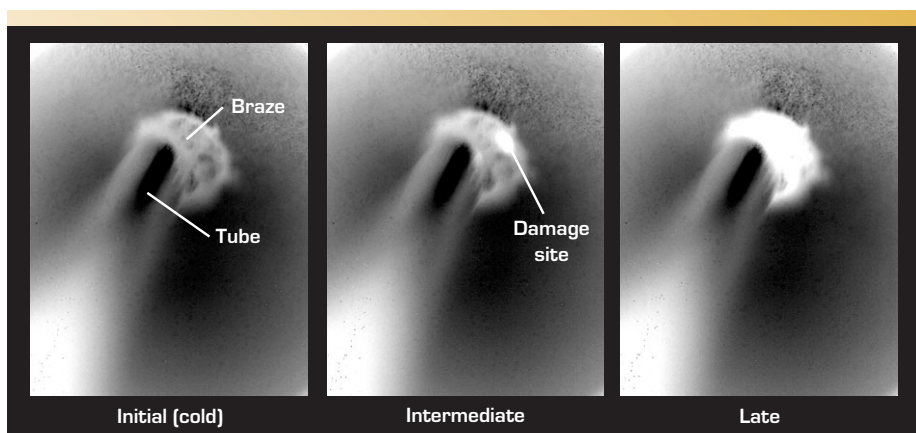


Figure 1. Tube braze results. Images show braze at three times: initial, intermediate, and late. Flaw location is identified at intermediate time, while the entire braze is warmed at late time.

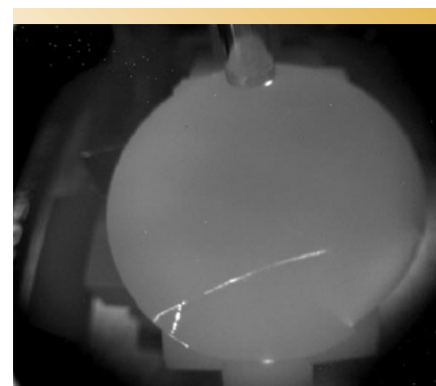


Figure 2. Sonic IR image of cracks in a composite material.

The significance and payoff for this project is that the dimensional metrology and characterization of target components and assemblies is as important as their fabrication. The actual target assembly is the input to the physical experiment, and the metrology and characterization data on the target assembly is the input to the physics simulation. Without the critical step of having certified standards for qualifying metrology and characterization tools, there can be no verification of performance of these tools.

The work was based on typical target geometries, features, and metrology requirements. Figure 1 shows finished products for the chosen cylindrical and spherical designs. The materials are plastics and low-density foams. These targets are usually less than 2 mm³ in volume and have μm-sized features manufactured onto them.

All the features and materials in these two designs have been chosen to

Mesoscale Metrology and Characterization Reference Standards

R. L. Hibbard, M. J. Bono, A. M. Waters, H. E. Martz


The goal of this project was to build a set of reference standards for typical laser target components and assemblies, with features that could be used to benchmark dimensional metrology and nondestructive evaluation (NDE) tools. These specific examples are being addressed because no commercial applications or standards address these mesoscale components and materials.

provide metrology and characterization resolution challenges, and represent realistic target geometries. Design considerations were made to ensure that dimensional stability over time could be maintained. The dimensional metrology and preliminary NDE data of these targets have been archived.

Preliminary computed tomography (CT) data were acquired for the spherical reference standard with an LLNL system (KCAT) and a commercial system. KCAT results are shown in Fig. 2. Qualitatively, one can begin to see flaws in the reference standard. For example,

be made.

The deliverables for this technology-base proposal were to: 1) define a set of standards; 2) build two sets of standards; 3) document the metrology of the standards; 4) characterize the standards with NDE tools, both at LLNL and with outside vendors; and 5) write a final report.

The goals of this proposal have been achieved. The standards are available for continued use to test metrology and NDE characterization tools, and have already proven their value. 

the left image shows that the bond on the left side of the joint is not uniform. In addition, the image in the center shows gaps or voids in the joint [the streaking noticeable in the equatorial slice image is a data acquisition artifact]. Preliminary analysis of this data has been done, but more data must be acquired and analyzed before quantitative conclusions and measurements can

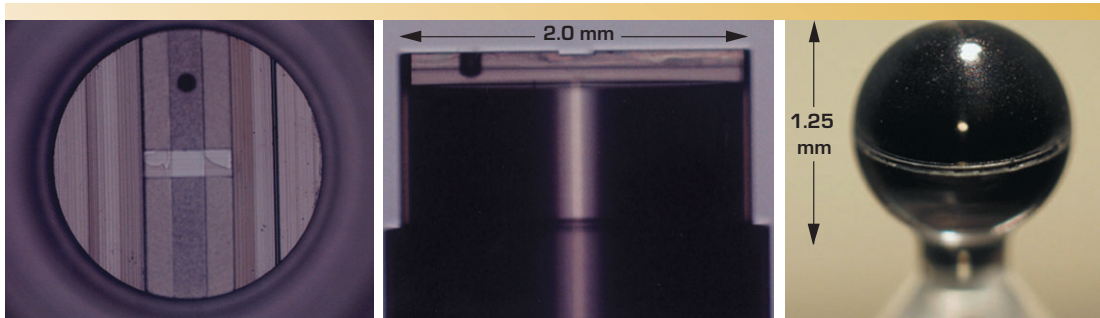


Figure 1. Two orthogonal views of the cylindrical subassembly and a completed spherical reference standard.

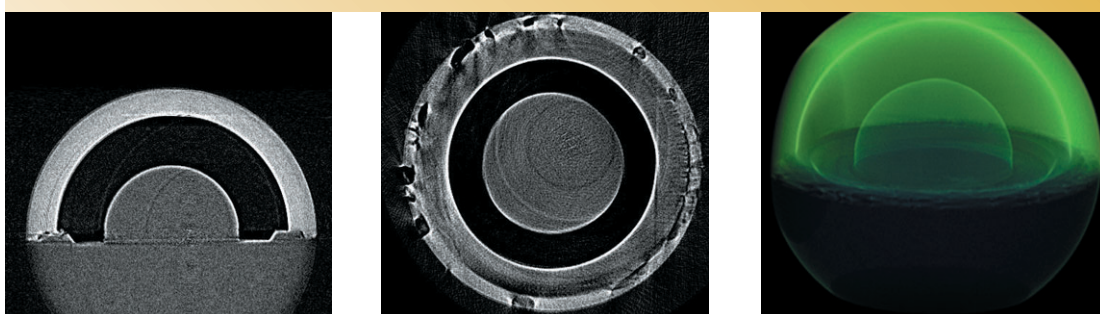


Figure 2. Left and middle: KCAT reconstructed CT slices through the vertical or polar plane and the equatorial plane, respectively, of the spherical reference standard. Right: 3-D volume rendering of the KCAT CT data.

We manufactured a set of 48 alumina and beryllia specimens with geometry chosen to facilitate the nondestructive methods applied. The specimen geometry offers two sets of parallel surfaces 22 mm apart and has no point, line or surface symmetry. Features are included to provide orientation confirmation in cross-sectional views cutting the axis.

The table lists the six defect types introduced into the specimen set, as well as the thirteen NDC methods applied to the specimens. The NDC methods can be divided into five modalities: x-ray (film radiography and x-ray CT); acoustic (acoustic tomography, ultrasonic velocity, and acoustic microscopy); optical (candling, spectrophotometry, and optical coherence tomography); thermal (thermosonics, infrared imaging, and photothermal imaging); and surface (dye penetrant and metrology).

In general, the defect types responded similarly within each NDC modality. Low optical transmission through 22 mm of beryllia and alumina prohibited imaging internal defects with the optical modalities. Surface techniques cannot characterize internal structures, but perform well on surface defects. Complementary to surface techniques, x-ray techniques identify internal geometry very well but are inadequate for imaging surface defects. The acoustic modality is very sensitive to internal material variations and surface defects, but does not penetrate beyond internal cracking. Thermal techniques have mixed results, with infrared imaging producing no defect response, while thermosonics gives excellent images of cracks.

The multi-modality NDC data set collected from a beryllia sample with molybdenum (Mo) inclusions illustrates four of the

Nondestructive Characterization of Ceramic Processing Defects

D. J. Chinn, C. M. Logan

The objective of this work is to understand the response of multiple non-destructive characterization (NDC) methods to known flaws in ceramic materials. Our overall approach is to manufacture ceramic specimens with intentional flaws, apply NDC methods, destructively section the flawed regions, then correlate the NDC results to micrographs of defects.

complementary techniques. During manufacture of the sample, several Mo wires, sized approximately 1.0 mm x 0.5 mm, are mixed into the beryllia powder before pressing.

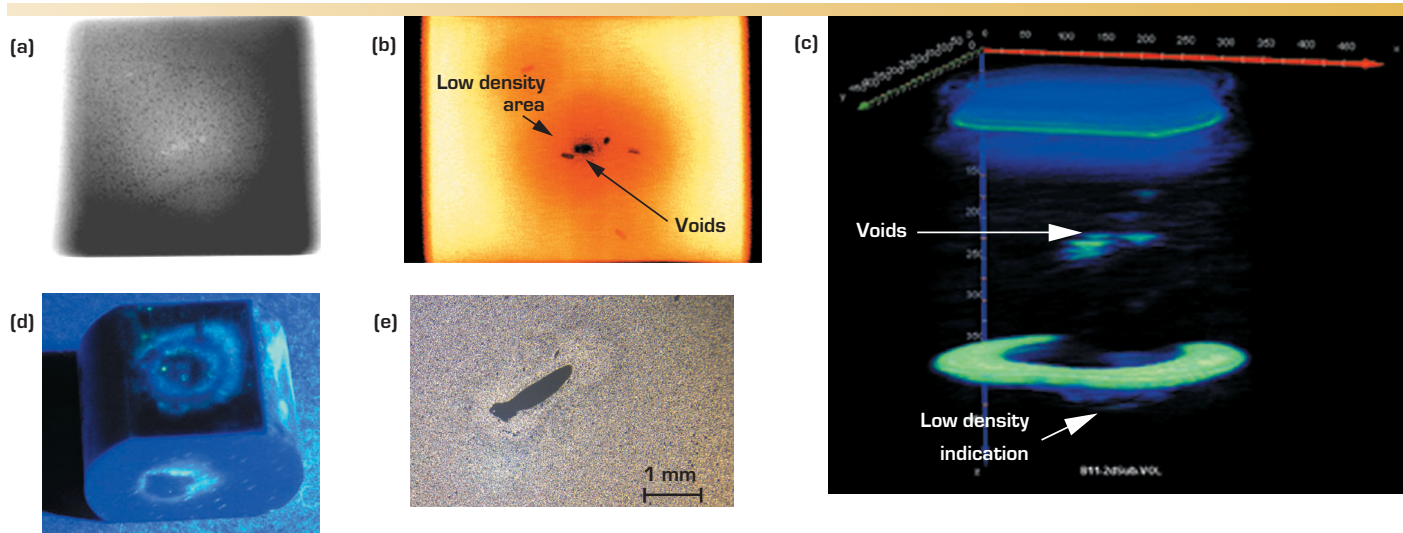
Film radiography and x-ray CT show evidence of several hundred highly attenuating particles. Film radiography (Fig. (a)) shows low-density areas

surrounding voids and highly-attenuating particles. A mid-thickness x-ray CT slice (Fig. (b)) also shows low-density areas surrounding voids. A rendering of 3-D acoustic microscopy data (Fig. (c)) shows reflections from voids and acoustic velocity variations, indicating low-density regions. Dye-penetrant testing (Fig. (d)) shows absorption patterns on three surfaces, indicating material variations. Destructive sectioning near a void (Fig. (e)) confirms the void size and shape.

Future work will include investigation of data fusion techniques to fully utilize the complementary aspects of the modalities. Analytical modeling using information from the data sets will also be investigated.

Defect types and NDC methods applied to the sample set.

Ceramic defect	NDC methods
Molybdenum inclusion	Film radiography
Unsintered agglomerate	X-ray computed tomography
Underfired (entire specimen)	Acoustic tomography
Delamination	Ultrasonic velocity
Thermal cracking	Acoustic microscopy
Surface cracks	Candling
	Spectrophotometry
	Optical coherence tomography
	Thermosonics
	Infrared imaging
	Photothermal imaging
	Dye-penetrant testing
	Metrology



NDC techniques, showing voids, low-density regions, and highly-attenuating particles in a beryllia sample with Mo inclusions: (a) film radiography; (b) x-ray CT; (c) acoustic microscopy; (d) dye-penetrant testing; and (e) optical micrograph of void from destructive sectioning.

The photothermal system was constructed as a means to detect, nondestructively, locations in optics that may damage under high laser flux. Detection of these sites before the optics are placed in service would allow the optics to be processed to reduce the risk of damage, and thereby increase the in-service lifetime of the optics, and also reduce aberrations to the beam that would degrade the beam and adversely affect experiments.

The system in its current state uses a temporally-modulated frequency-doubled Nd:YAG laser (532 nm wavelength) to act as a pump beam on an optic. A diode laser with a wavelength of 635 nm is used to probe the surface of the optic at the area being pumped. Unwanted particles in the coating that absorb the pump beam more strongly than the bulk of the optic will lead to a distortion of the probe beam. The probe beam is reflected off the surface of the optic and sent to a CCD camera. This imaging by camera allows faster scanning of optics when compared to traditional single-point pump-probe techniques.

Unwanted fringes arising from optics in the photothermal system had been affecting the images being obtained. Some of the optics in the camera were modified by the manufacturer according to our requests, and this greatly reduced problems with unwanted fringes.

Since the resolution goal of this system is on the order of micrometers, with sub-micrometer imaging being a possibility, motion of the components can be a problem. Modifications were made to some of the mounts holding various components. These modifications were found to improve the images, yielding an increase in signal-to-noise. Some vibration issues remain, but resolving these is beyond the scope of this project.

The figure shows an approximately 10-mm-x-10-mm area of a BK-7 sample with a dielectric coating scanned using the photothermal system. The image is

Optimization of Photothermal NDE System

R. D. Huber, D. J. Chinn, C. J. Stolz, C. L. Weinzapfel

Improvements have been made to the sensitivity of a photothermal system. These improvements were accomplished by modifications to the optics, particularly those of the camera, and also through more robust mounting of the components to reduce the effects of vibrations. The net effect of these modifications was to reduce noise in the images obtained, and thereby increase the overall signal-to-noise.

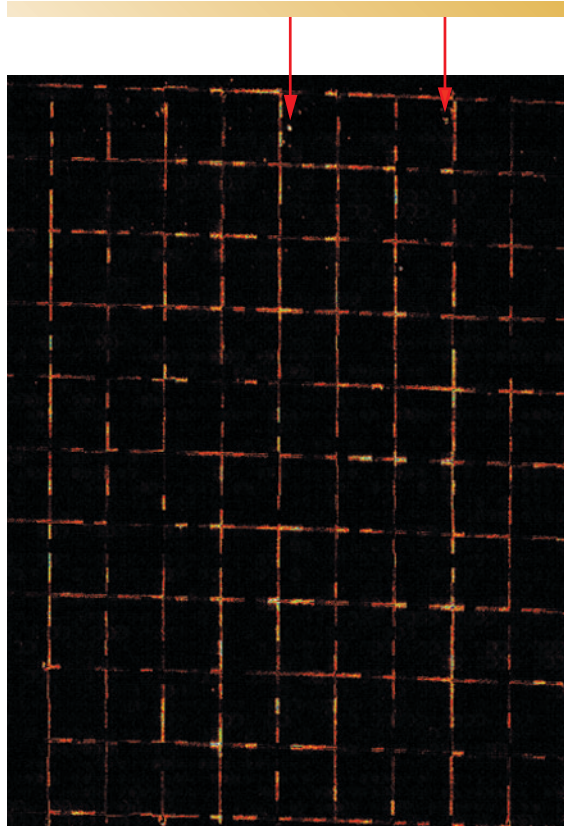
rectangular since the camera views the sample at an angle. The image resolution was 2.64 pixels/ μm in y (vertical) and 2.12 pixels/ μm in x (horizontal).

Data reduction was performed to display the image. This is the largest scan yet obtained using this technique. In addition to the marks scribed onto the sample at 1-mm spacing, several spots show potential damage sites as indicated by high intensity on the image. Arrows on the figure point out a few of these potential damage sites. Damage studies will

be performed on the sample to identify the type of defects.

The scan for the figure took approximately 30 h. The figure is actually a composite image made up of 50 x 52 smaller images. The system is currently limited in pump power. A higher-powered laser would allow a larger area of the sample to be pumped for each individual image obtained. Currently, for the field-of-view being used, more than half of the camera pixels are not used in the composite images, since the pump beam does not cover them.

The plan is to move the system from its current location and reassemble it for implementation and deployment. The system will be modified to allow use of a higher-powered pump laser and scan times should be greatly reduced, allowing larger optics to be scanned in more reasonable times.



Photothermal image of defects in BK-7 glass. Lines are at 1-mm spacing.

Our microtomography system is intended to provide nondestructive characterization of microstructure, and internal dimensioning of samples and components with an achievable spatial resolution of 1 μm . The system consists of translation and rotational stages, a lens coupled camera-based imaging system, and data acquisition and control software. It is able to obtain 3-D microstructural images with monochromatic hard x rays in the energy range 4 to 140 keV.

During the past year we accomplished the following: 1) the data acquisition software was tested and modified to reduce electronic overhead involved with camera readout and stage motion; 2) improvements were made and tested for aligning the imaging detector (camera and scintillator); 3) image tiling software was applied to handle samples of larger diameter than the field of view of the camera; and 4) a number of application results were

Synchrotron Microtomography at ALS

K. W. Dolan, D. Haupt, J. H. Kinney, D. J. Schneberk, T. Smith

A microtomography system has been installed for nondestructive microstructural characterization and internal dimensioning at small length scales. The system has been installed on the dedicated computed tomography beamline at the Advanced Light Source (ALS) synchrotron facility at LBNL.

obtained to test and demonstrate system capabilities with the system fielded at the Stanford Synchrotron Radiation Laboratory (SSRL) prior to completion of the ALS beamline.

At the beginning of FY03, new software was tested that greatly increased data acquisition rates. The data acquisition time is now limited by the photon intensity and the speed with which the rotation stage moves the specimens. Imaging specimens of importance to LLNL programs provided important functional tests of the new system. High-explosive samples were imaged with microtomography at multiple energies, allowing particle and boundary phases of the explosive to be separated and

analyzed, and to obtain pore density for the first time [see Figs. 1 and 2].

High quality 3-D images of the microstructure of shock spallation samples were obtained that show both void morphology and particle size distributions. A new tiling algorithm that enables imaging of large diameter

(larger than the camera field of view) specimens at high spatial resolution was tested in two dimensions on aerogel witness plates. The same tiling program was demonstrated in three dimensions for reconstruction of a human vertebra.

The microtomography system components have been installed at ALS (Fig. 3). Significant improvements in image resolution and contrast and extended capabilities are expected since the beam divergence and beam intensity at ALS are both improved by nearly a factor of 10 compared to SSRL, x-ray energies extend to nearly a factor of 5 higher (140 keV), and new contrast mechanisms, such as phase contrast, can be explored.

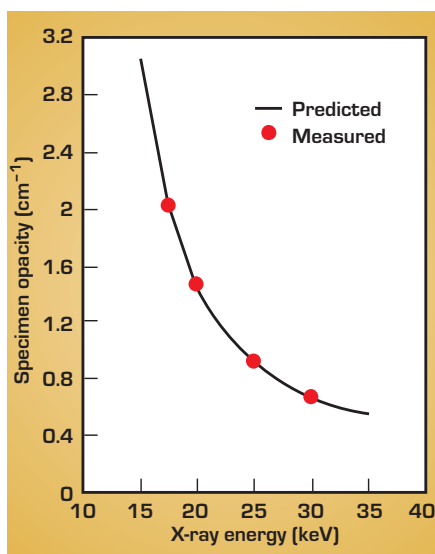


Figure 1. Multiple energy microtomography. Analysis of scans provides sample averages for binder, explosive, and porosity volume phases.

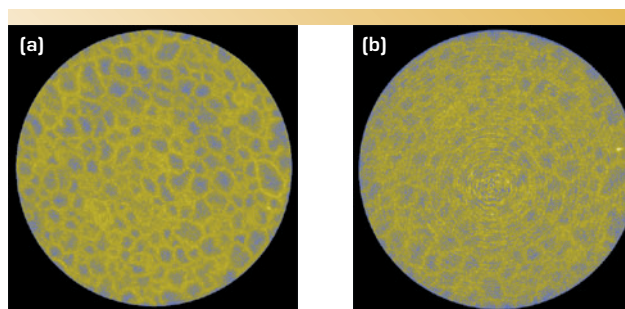


Figure 2. Multiple energy scans: MicroCT images at (a) 17.5 keV, and (b) 30.0 keV.

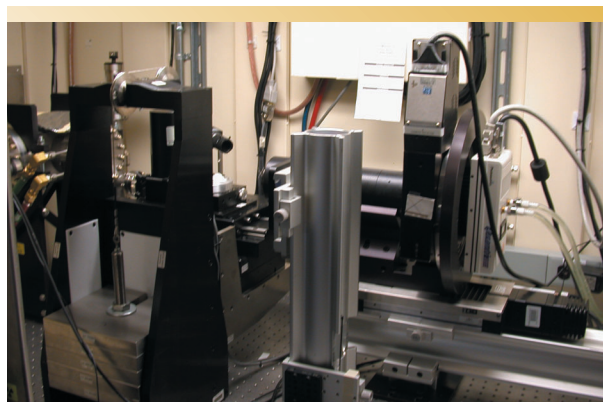


Figure 3. Microtomography system installed at ALS. Monochromatic x rays in the energy range 4 keV to 140 keV are provided by two interchangeable monochrometers, a multiplayer monochromator (4 keV to 60 keV), and a silicon crystal monochromator (60 keV to 140 keV). Beam profile is 60 mm wide to 5 mm high. Data acquisition time is less than 50 μs per image.

Traditional ultrasonic imaging converts amplitude-time information into a 2-D image by time-gating the data and color-coding the amplitude of the signal in the gate. Unfortunately, this approach throws away the depth information. We are capturing all the information in the ultrasonic waveform and processing that information to generate a 2.5-D (from C-scan data) and a 3-D (from acoustic tomography) image (see figure).

Once the image is rendered, it can be manipulated to best display the internal structure of a component. Thus, 2.5- and 3-D rendering of ultrasonic images greatly increases our ability to interpret the data. Our customers gain a better understanding of the results when viewed in three dimensions. Also, our ability to characterize components in three dimensions will support "as-built" modeling of objects.

There are two main tasks involved in rendering ultrasonic data in 2.5- and 3-D. One task is to capture the full ultrasonic data set and store the data in the computer. The other main task is processing the data to render the 2.5- or 3-D image.

Three-Dimensional Rendering of High-Frequency Ultrasonic Data

S. E. Benson, G. H. Thomas

Our technology-based project includes specifying the hardware and software requirements for a PC-compatible, 3-D rendering of high-frequency ultrasonic data.

Our progress to date includes specifying the hardware and software requirements for a PC-compatible 3-D volume rendering system. The two major components of the system include a real-time 3-D volume rendering card and a software package capable of using the rendering hardware as well as providing visualization routines for processing, displaying, and manipulating the ultrasonic 3-D volume data set in real time.

We have installed the hardware and software in a computer workstation dedicated to this project and have rendered 2.5-D ultrasonic data with the system.

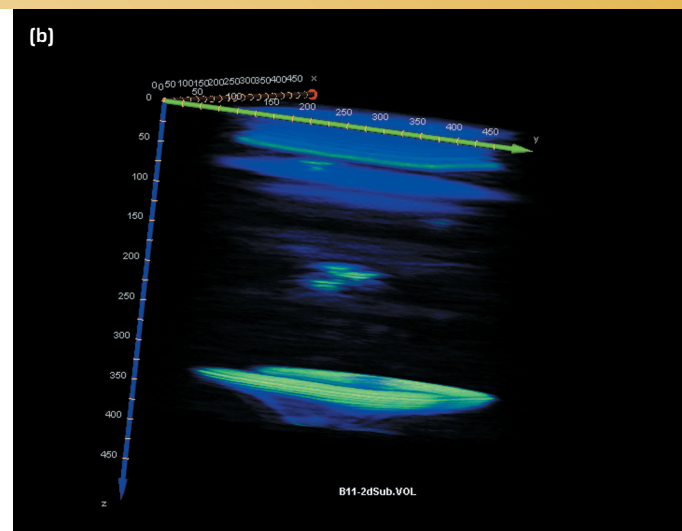
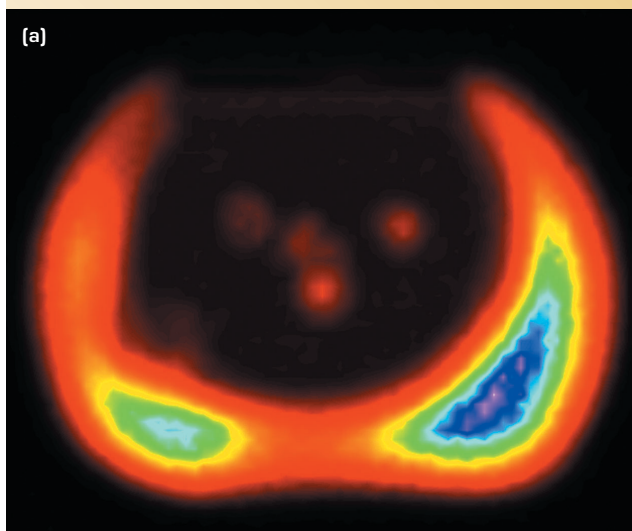
We completed the ultrasonic data acquisition and software system that is capable of capturing ultrasonic RF waveforms over an area of interest. Capturing the full ultrasonic waveform entails

assembling the instrumentation and writing the computer driver to digitize the signals. These signals must be correlated to the scanner position at the time of digitization.

We completed the post-signal-processing software that provides an interactive user interface and tools that allow for a region of interest or sub-volume to be extracted from the ultrasonic data set.

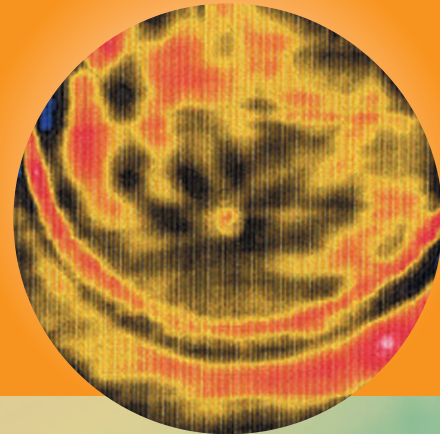
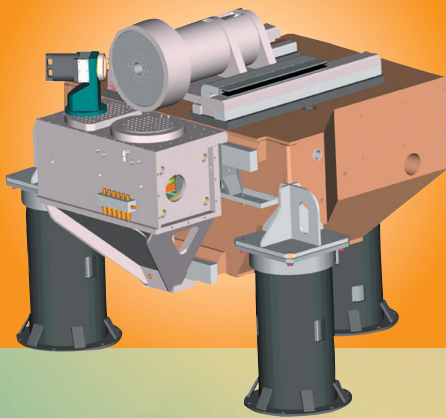
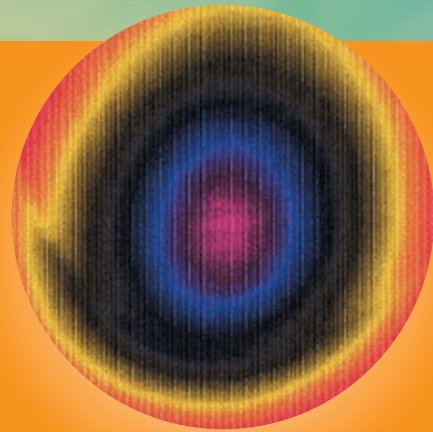
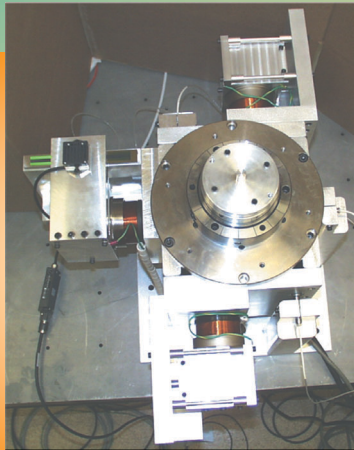
The sub-volume is then converted to a binary data file compatible with the rendering system. We successfully acquired, processed, and volume rendered a data set from a ceramic part with internal flaws.

Next year we will further advance the post-signal-processing to remove ultrasonic waveform ringing artifacts, overlay as-built models on the 3-D display, and deploy a computer workstation dedicated to ultrasonic 3-D rendering. The final product will be a technology to capture and render ultrasonic data so that 2.5- and 3-D characterization can be realized. This information can be incorporated into modeling codes to predict component performance based on as-built characteristics.



(a) Two-dimensional conventional time-gate image. (b) Two-and-a-half-dimensional volume rendering image.

Center for Precision Engineering



An unbalanced spindle creates a rotating force vector with a once per revolution period. The cause and size of this force vector is a function of the spindle, the part, the part fixturing, the part setup, and the spindle speed. In addition, certain spindle speeds coupled with the size of the unbalance force vector can contain other harmonics that may excite machine structural resonances. The magnitude of the unbalance force vector increases as the square of the spindle speed.

Our system can be used to actively cancel spindle unbalance forces — specifically, to attenuate the spindle housing vibration using an active vibration control process to prevent the unbalance forces from disturbing the rest of the machine systems (e.g., the slide servo system or the machine metrology frame).

The displacement induced by the unbalance force is held to nanometer levels (sensor-dependent) regardless of the spindle speed or changes in the part contour, and adapts in real time to changes in unbalance forces.

The ideal solution is to cancel the unbalance forces at the source or rotor of the spindle. This is difficult, since the rotor must hold the part and any apparatus that would be used to cancel the vibration forces that radiate from the spindle housing so that these forces do not induce motion into sensitive machine systems.

The basic concept of the system is to measure the force-induced spindle-housing motion and exactly cancel this motion with a controlled, moving inertial mass. Essentially, the spindle housing motion is measured with a displacement sensor referenced to the machine base. This measurement, along with the spindle angle (measured with an encoder) is fed to a controller running a specific

Active Vibration Isolation of an Unbalanced Machine Spindle

D. J. Hopkins, P. Geraghty

Proper configurations of controls, sensors, and metrology technologies have enabled precision turning machines to achieve nanometer positioning. However, at this level of positioning resolution, vibration sources can become a limiting factor. One of the largest sources of vibration in a turning machine may be an unbalanced rotating spindle. The purpose of this technology-base project is to implement a system that actively cancels spindle unbalance forces. In the second year of this project, we have refined the control algorithm and extended the degrees of freedom the system can control.

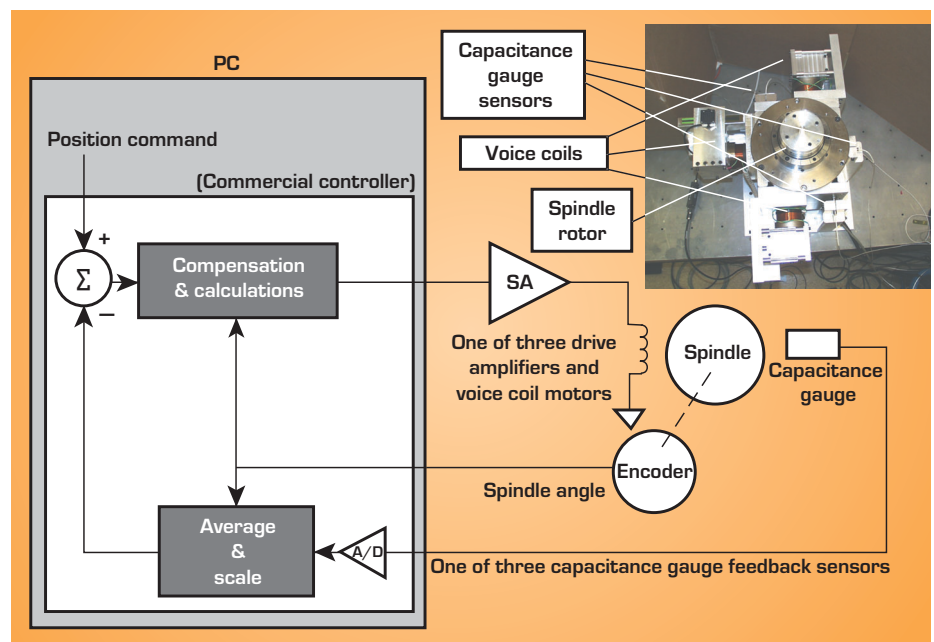
algorithm. The algorithm computes the required signal, and the controller actuates a voice-coil (VC) motor, canceling the original force-induced motion. The amount of force required to cancel the unbalance spindle force is a function of frequency (spindle speed), the amount of mass the VC is moving, and the range of VC travel.

In FY02, we focused on canceling the unbalance force in a single direction. In FY03, we have addressed three degrees of freedom of spindle housing motion: the x direction (the single-VC motor); the y direction (the two y VC motors acting

together); and rotationally, the yaw motion (the two Y VC motors acting in opposition).

The testbed and a block diagram of the control system are shown in the figure. In addition this year, the control system has been refined to eliminate the scale feedback on the VC motors. The control algorithm is fully implemented on a commercially available controller and is sensitive only to unbalance-induced motion.

The system and control algorithm have demonstrated the ability to adapt in real time to remove the fundamental component of the unbalance rotational force vector to nanometer levels. However, high-order structural resonance components of the testbed have been observed when the system is active. The control system is stable and the VC excitation is harmonically clean, but the high Q (measured) of the mechanical system is apparently excited by energy leakage. Our results indicate the need to examine carefully the dynamics of any spindle system that would take advantage of this active system.



Control system block diagram and top view of the physical system.

Increasing demands in precision engineering for high-resolution displacement measurements and motion control require high-sensitivity, low-noise sensor signal conditioning techniques. Sensor measurements and signal conditioning at DC or low frequencies are prone to thermocouple wire junction effects, amplifier offset drift, shot noise, $1/f$ noise, and many other noise sources. If the sensor

information is placed on an AC carrier signal, and signal-conditioned, then synchronous demodulation can be used to convert the signal back to the baseband frequencies with significant signal-to-noise improvement.

Synchronous demodulation is a well-known technique, and highly effective against external noise sources that may attempt to contaminate the sensor signal. The technique creates, in essence, a highly-tuned filter around the sensor excitation frequency. Synchronous demodulation uses a phase-sensitive detector to recover the original signal information. It is highly effective in picking out a desired signal (synchronous to the sensor excitation) out of what otherwise would appear as noise.

In addition to high sensor-resolution requirements, there is a need to measure over a large dynamic range, and for

Digital Synchronous Demodulation and Conditioning for Precision Sensors

D. J. Hopkins

Instrumentation for high-sensitivity, drift-free measurements of displacement and temperature are an important part of precision engineering. The resolutions of existing sensors are limited by the inherent noise of the sensor and the signal conditioning electronics. The focus of our technology-base project is to perform the task of signal conditioning and synchronous demodulation in the digital domain, using high-resolution A/D and D/A converters, coupled with a digital signal processor performing the demodulation algorithm.

the conditioned signal to be made available directly to a computer for data acquisition, or to a dedicated machine tool controller for motion control. Currently, the fulfillment of these requirements rests typically with a dedicated analog instrument for each sensor channel. The instrument provides signal conditioning and synchronous demodulation and an analog output signal that can be digitized by an external A/D for input to a control system. There are strict requirements on the A/D. It must have a high bit count for resolution vs. dynamic range; it must have no missing codes; and it must support simultaneous sample and hold with other system channels. The last two requirements are important for control systems.

Figure 1 is a simple block diagram of a typical channel of sensor signal

conditioning. It is composed of an oscillator for sensor excitation, a gain block (not illustrated), a phase-sensitive detector (PSD), the synchronous demodulator and a low-pass filter (LPF). The output of the LPF provides an analog signal that can be digitized by an external A/D converter.

This technology-base project has combined the sensor signal excitation [oscillator], gain block, PSD, LPF and A/D into a single instrument. This reduces costs and provides a more flexible device.

Figure 2 is a simple block diagram of a single channel of our approach. Note that there are two possible outputs per channel. The first is the digital signal that can be used directly by an external motion controller, and the second that converts the internally calculated results back to an analog signal.

There are issues that limit the number of channels that can be processed and the ability to support direct control system use. [Phase delays through the processing system limit control system bandwidth.] These issues include the excitation frequency; the input and output buffer depth; the computational processing delay; and because this is a phase-sensitive technique, the sample rate vs. the sensor excitation frequency.

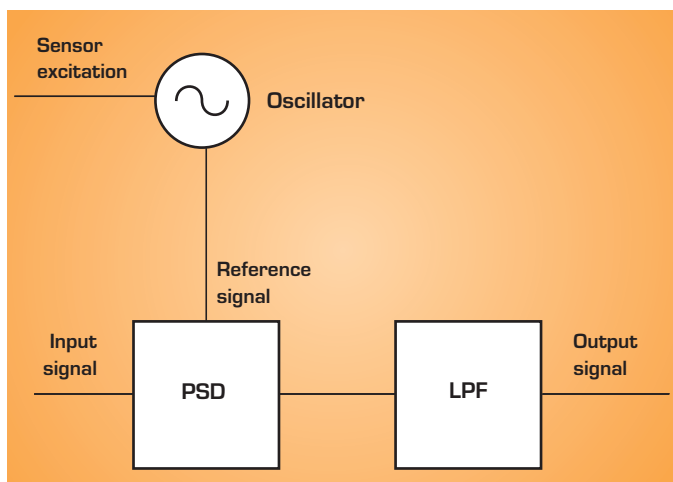


Figure 1. Typical analog method of excitation and sensor signal conditioning.

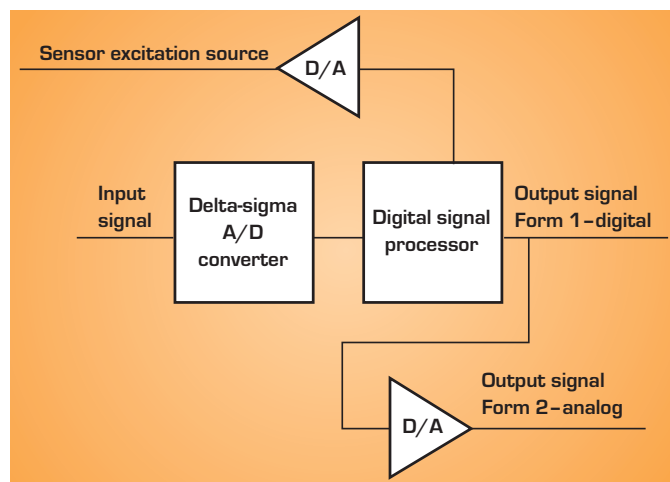


Figure 2. Technology-base method of excitation and sensor signal conditioning.

Our interest is in the use of the MRF tool for improving our figure and finish capabilities in classical diamond turning applications.

Improvements in capabilities could be in two different directions. The first would be in increasing the range of materials, since the list of practically useful diamond-turnable materials is fairly small. The advantage of the diamond turning machine over conventional optical grinding and polishing techniques is that the determinism of the machine leads to little iteration in the fabrication process. Using the MRF process on an accurate machine is a composite of the two approaches, allowing parts that are difficult to measure interferometrically to be fabricated cost-effectively.

Silicon is an attractive material for the fabrication of optics for several applications, such as space-based laser-cavity optics and optics for x-ray laser light sources such as the Linac Coherent Light Source. Two problems identified in fabricating silicon optics are generating a steady state MRF process and applying this process on a real optic, where material hardness may vary within the part due to the crystalline orientation.

During this technology-base project, we have applied the MRF process to silicon wafers and found acceptable process parameters for good material removal. In the future, we will look to figure mirrors with varying crystalline orientations. This achievement would give high confidence that silicon mirrors, such as the space-based laser-cavity optics, could be fabricated using the MRF process on a diamond turning machine such as LLNL's Large Optics Diamond Turning Machine (LODTM).

MRF Technology for Non-Glass Applications

J. L. Klingmann, W. F. Brocius

LLNL has acquired a magneto-rheological finishing (MRF) machine for application to glass optics for various programs. As configured from the factory, the machine is suited to the finish fabrication of moderate-sized (200-mm) glass optics that can be measured with conventional interferometric techniques. We are interested in using the MRF tool for our diamond turning applications. We have worked on capabilities that could improve parts that we would traditionally fabricate on diamond turning machines in a range of materials.

The reason for using LODTM is its extreme accuracy, which would be required for measurement and feedback to the MRF process.


The second improvement is adding MRF capability to our diamond turning machines for typically diamond-turnable materials. In this approach MRF would be an iterative material removal process using the diamond turning machine as a metrology tool. The goal here is to achieve better accuracy and surface roughness, and this approach has the potential to be extrapolated to the fabrication of non-axisymmetric optics.

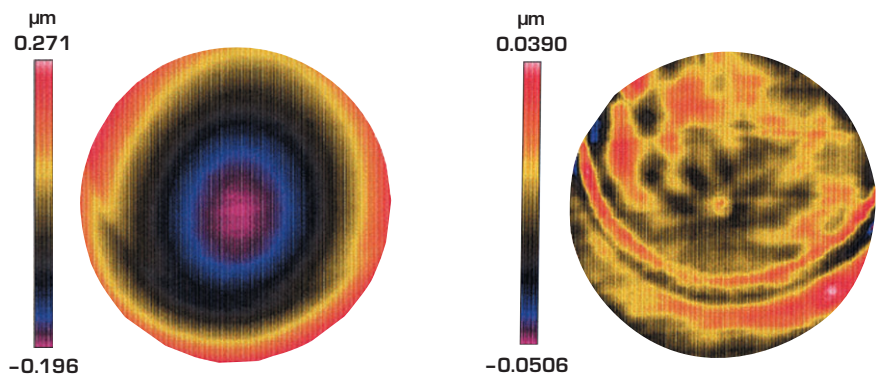
On plated nickel samples, we had early difficulties with the MRF process causing streaks in the nickel, seemingly initiated by the tooling cusps in the nickel surface.

We overcame this problem with a change in abrasive to diamond, and were able to produce surface figure improvements of a factor of three to ten, with similar roughness improvement to 15 Å rms. The example shown in the figure has an improvement in figure error of more than five times.

Aluminum samples were difficult to evaluate because of contamination of the alloy with other materials. The

MRF process seemed to work well but left behind distinct spots of contamination. As a result, we are interested in using MRF as an evaluation tool to understand the contamination of aluminum and its effect on diamond turning.

This project has given the Laboratory an introduction to the capabilities of the MRF process. We have demonstrated its capabilities on non-glass materials of interest to LLNL and other national programs. Potential areas for future work are in the application of this technology to grazing incidence optics, where the process would be installed on an accurate diamond turning machine, and, if the material removal function can be made small, to the fabrication of millimeter-scale components. 



Before and after interferograms of nickel parts, showing five-times improvement in rms figure error.

Major factors in the performance of a machine tool are the loop gain and the bandwidth of the machine servo system. The servo system plays a key role in both the static and the dynamic performances of the machine tool. Good static performance provides high stiffness of the machine and allows it to follow with high accuracy the commanded tool path. Good dynamic performance is important to reject disturbance forces, and is a function of the servo system bandwidth, specifically the loop gain at the disturbance frequency. Increasing the loop gain generally implies an increase in the system bandwidth. The loop gain decreases with increasing frequency and provides enhancements in machine performance until it drops to a gain of one.

Several factors, such as amplifier bandwidth, feedback sensor response, and, most importantly, machine dynamics, can limit the final machine bandwidth. It is generally the machine structural dynamics that limit system bandwidth, primarily due to mechanical resonances. A simple proportional, integral, and derivative (PID) gain control loop cannot address these resonances and so the loop gain and machine bandwidth must be limited to keep servo stability. A solution is to shape the dynamic response by adding one or more second order filters to the loop response.

The typical servo architecture of each axis of the controller used in this project is shown in the figure. Up to 32 axes can be configured in this particular controller. All relevant components of the servo algorithm (block) are shown, including the PID terms, a second order filter, and the ability to provide motor commutation.

Servo System Machine Tool Control Analysis

D. J. Hopkins, G. F. Weinert, T. A. Wulff

Several LLNL precision machine tools have been built with custom-designed controllers, many of which have reached the end of their effective lifetime. Attempts to replace these controllers with commercial controllers have had only limited success, but recent technological improvements have overcome some of the limitations. In this technology-based project, we exploit the capabilities of one of these controllers to allow it to process multiple feedback sensors per axis for tool-tip calculations in real time, and to extend the servo compensation capabilities by cascading several standard motor compensation loops.

By using a custom written servo algorithm and giving up a motor axis, we have been able to direct the output of a block to the input command of a second block, and so on, until the required number of second order filters is added to the loop. Servo loop response measurements do not indicate any significant phase delay is added to the loop as the number of blocks increases.

Tool-Tip Calculations. There are at least two methods to correct for machine geometry errors in the x-z plane of a machine tool. The first method relies on an independent (not part of the controller) geometrical correction system. The controller calculates the x- or z-axis motion independent

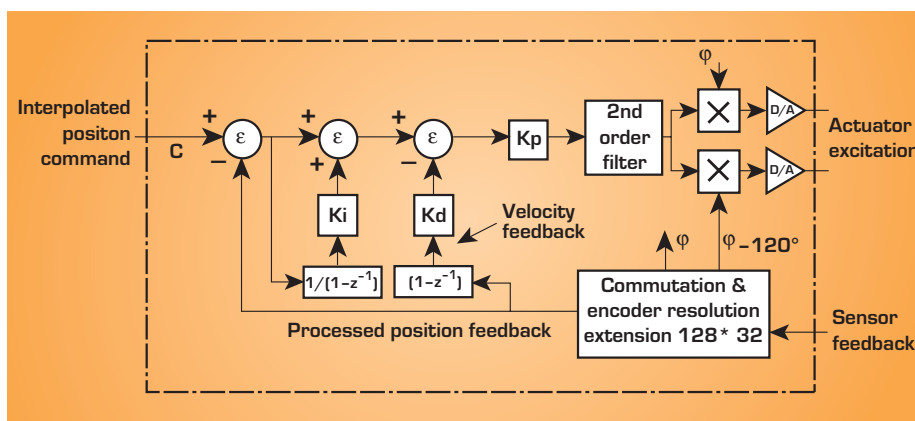
of all axes. The second method is to use the machine tool controller and accept multiple feedback sensors per axis to calculate the tool position and geometry corrections in real time.

Exploiting the custom servo algorithm of this controller, we have software that calculates an effective feedback input for a block based on at least two feedback sensors. The calculation exists at the servo algorithm

level to account for dynamic force disturbances. This separates this kind of correction from a part program correction because it does the correction in real time at the servo rate.

The benefit of this work is that it demonstrates that the controller has the necessary flexibility to provide tool-tip calculations for machine geometry corrections in real time. The ability to mathematically calculate an effective tool position from multiple feedback sensors is very important for achieving high accuracy in a precision machine tool.

LLNL has several machines that require this capability or could take advantage of this capability, including the new POGAL machine, the LODTM, PERL I and PERL II, and Pneumo.



Standard controller servo architecture.

SAW technology (Figs. 1 and 2) is new enough that there are no companies selling the motors. One company that we've had successful technology exchanges with in the past was a potential vendor, but was not able to get the part to us in time to perform meaningful research before the end of the fiscal year.

Wear is a problem with SAW motors. The rotor and stator are in direct contact with a preload force. The friction caused by the rotor against the stator causes both parts to wear out. As the parts wear, there would be inconsistent drag, resulting in an uncontrolled rotational motion. The additional friction of the worn area would also cause a change in response to the control inputs, complicating the system design. For these reasons, SAW motor technology is not mature enough for precision motion applications at this time.

Most of the literature on SAW motors is from, or based on, work at the Tokyo Institute of Technology.

The stationary part of the motor, the stator, is made of piezoelectric material

Surface Acoustic Wave Motors

S. L. Hunter, K. Carlisle

We have investigated surface acoustic wave (SAW) motors for use in precision motion at the mesoscale level. SAW motors create high-frequency vibrations in a small plate to push a slider along. The slider can be pushed in both directions by having a vibration source at each end of the plate. Since the motor uses high-frequency vibrations for drive, the motions are very smooth, which would be an advantage for precision motion at the mesoscale level.

so that the vibrational waves can be introduced with an electrical signal. The signal is applied to a structure called an interdigital transducer (IDT). This structure is two sets of interlocking fingers, as shown in Fig. 1.

The oscillating signal applied to the IDT creates traveling waves in the stator by piezoelectric action. These waves travel along the stator away from the IDT. The waves cause an elliptical particle motion on the surface of the stator, resulting in a lateral force against the slider, pushing it away from the IDT.

Typical dimensions for the stator are 20 mm to 30 mm, but one was 75 mm. The sliders move at speeds from 18 cm/s to 110 cm/s. The sliders were capable of exerting a lateral force of 3.5 N to 10 N.

Other types of ultrasonic motors include: traveling wave motors; inchworm motors (electrostatic, clamping, and asymmetric friction); and impact positioner motors.

SAW motors have several desirable features. They can make nanometer movements; they require no lubrication (useful in vacuum environments); and their vertical motion is only about 20 nm.

However, there are a number of undesirable features of SAW motors at this time. The slider and stator wear over time and have to be replaced. The high-frequency vibration, about 10 MHz, and the resulting vertical motion limit its use in precision engineering. The rotor movements are not completely deterministic — there is stiction at start-up, and the step size depends on force-clamping slider to stator, which means that the step size is also load dependent. The lateral and rotational motions must be constrained by mechanisms that would contribute to inaccuracies in the system. Finally, self-heating of the IDT can cause a resonant frequency shift and reduce efficiency.

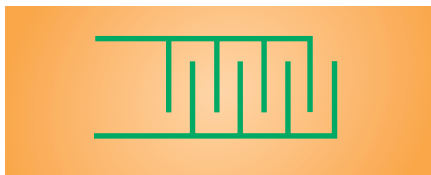


Figure 1. Interlocking fingers that make up the interdigital transducer in a SAW motor.

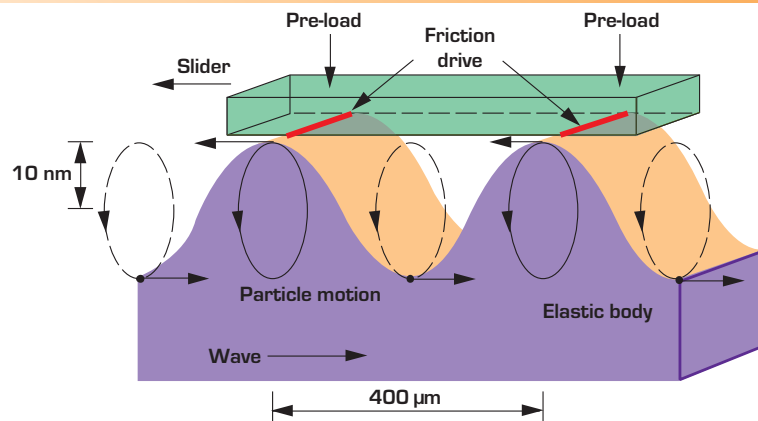


Figure 2. Conceptualization of SAW motor principles.

Fluid-film and air-film bearings have been used for machine spindles whenever precision motion requirements exceed the capabilities of traditional contact bearings (on the order of 1 μm). For example, in the 1970s, "T"-based lathe spindles used the contact (ball or roller) bearing technology. A quantum leap in spindle accuracy was achieved when these spindles were replaced with porous graphite air-bearing spindles, achieving <0.1 μm accuracy.

In the late 1970s and early 1980s, LLNL led in the field of high-precision diamond-turning machining, using porous graphite air-bearing spindles. Machines such as DTM #1, DTM #2, DTM #3, and LODTM all pushed the field of precision diamond turning to higher and higher levels of accuracy. Though 20 years old, these machines still operate at the limits of current machine accuracies.

LLNL is now designing the next-generation machine tool (see figure). Precision Optic Grinder and Lathe (POGAL) is the next machine that will push the limits of machine accuracy farther still. POGAL is required to have spindle accuracies of <50 nm in both axial and radial directions.

In addition to the precision requirements of POGAL, there is an increasing demand for larger parts requiring diamond turning that is reaching the load capacity of air-bearing spindles. Precision grinding of hard optics, a capability of POGAL, is also on the increase, requiring greater stiffness and damping from our machine spindles.

This all leads to the use of hydrostatic oil-film bearings. When compared to air bearings, oil hydrostatic bearings have higher stiffness, higher load capacity, and better damping characteristics. The problem is conventional pocketed oil-film-bearing spindles have not been able to

Ultra-Precision Machine Spindle Using Porous Ceramic Bearings

P. Geraghty, K. Carlisle, L. C. Hale

Air bearing spindles have typically been used for ultra-precision machine applications, due to the low asynchronous error motion and the high rotational accuracies achievable. Traditional oil-fluid-film bearings have not been able to match the accuracies of air bearings, but they have the advantages of higher stiffness and improved dampening capabilities. With the advent of new oil-fluid-film porous ceramic bearing materials, we may now be able to have the best of both worlds: the accuracy of an air bearing with the high stiffness and improved dampening capabilities of a traditional oil-fluid-film bearing.

match the accuracies achievable with air-bearing spindles, which is thought to be due to their high averaging effects.

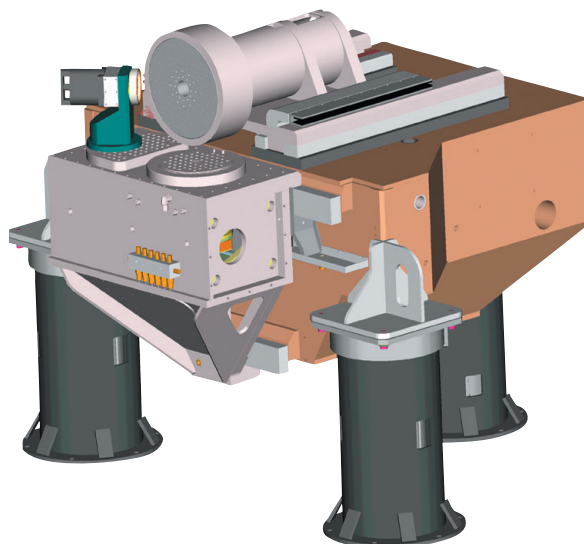
The materials science laboratory at Cranfield University, UK, has developed and commercialized the production of porous ceramic bearing material, which is now readily available. It is hoped that with this new ceramic bearing material, we may now be able to get the accuracy of an air bearing with the high stiffness and improved dampening capabilities of a traditional oil-fluid-film bearing.

As part of the initial phase of this project, we collaborated with staff at Cranfield Precision, UK, to design an ultra-precision machine spindle using this new material. This spindle has been designed to meet the requirements of POGAL.

This is a three-year project. The goals of the first year were to: 1) design a porous-ceramic-bearing spindle that meets the requirements of POGAL; 2) prepare a complete engineering package includ-

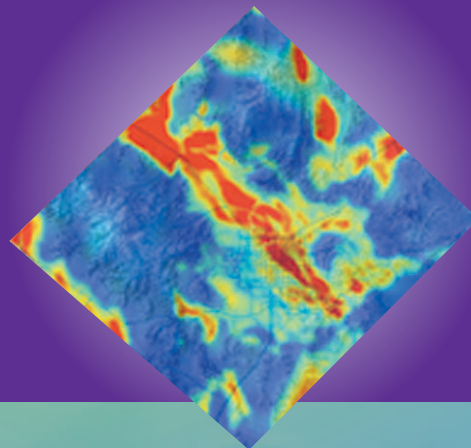
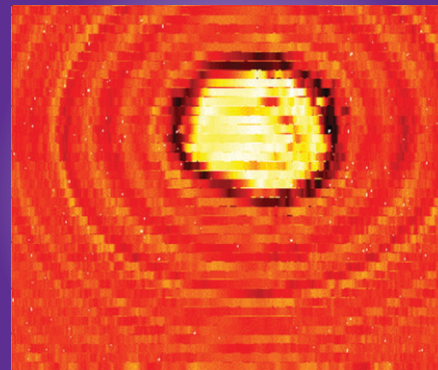
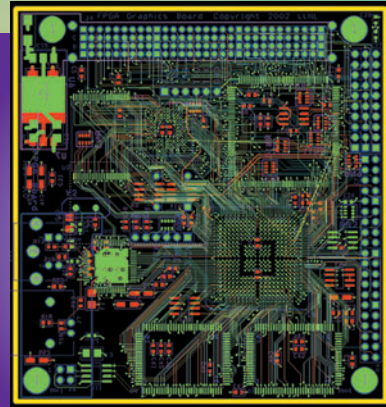
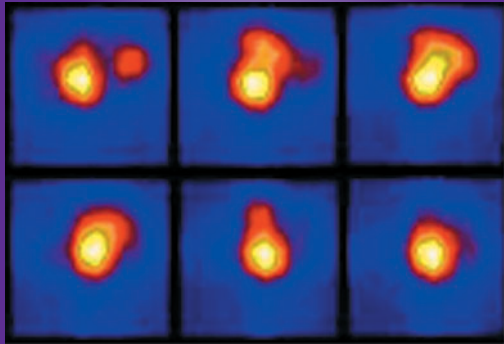
ing assembly drawings, detail drawings, tooling drawings, and engineering analysis; and 3) develop a mathematical model to predict the performance of the spindle. The goals of this second year were to: 1) fabricate, to a rough state, the ceramic bearing components; 2) fabricate most of the other spindle components; 3) acquire a drive motor needed for spindle testing; and 4) fabricate most of the testbed hardware.

We have achieved all seven goals to date and we are on track for completing this project next year.



Conceptual drawing of the new POGAL machine, the next-generation machine tool being designed at LLNL.

Center for Complex Distributed Systems



The flexibility and speed requirements for security and monitoring systems have been the driving parameters for our high-speed reconfigurable image processor based on the Field Programmable Gate Array (FPGA) [see Figs. 1 and 2].

Phase One of the project has produced an FPGA accelerator board that contains a one-million-gate array with a video analog-to-digital converter, large banks of on-board memory, and a peripheral component interconnect (PCI) bus interface to additional accelerator cards or CPUs.


Automated Sentinel

V. N. Kohlhepp, S. D. Freeman

As vision systems become increasingly prevalent for inspection, surveillance, and control, it is obvious that the capability of standard microprocessors and even special purpose digital image processors cannot keep up with the requirements for faster, higher-resolution imaging. To provide the capability that allows advanced image-processing systems to be built, a massively-parallel computational platform had to be available. This was the goal of the Automated Sentinel project.

Although custom digital image-processing systems involve extremely complex hardware, we have accelerated our second phase through the use of very high-level tools and simulators. The use of a parallel variant of the standard ANSI C programming language,

specifically targeted to gate arrays, has shortened schedules by a significant amount. We have therefore been able, in the span of three months, to produce a video image processor capable of real-time performance unmatched by even the fastest standard workstation.

As our software and image-processing libraries continue to grow, the power and speed of our approach to massive parallelization promises to provide the path to the next generation of flexible image-processing applications. 

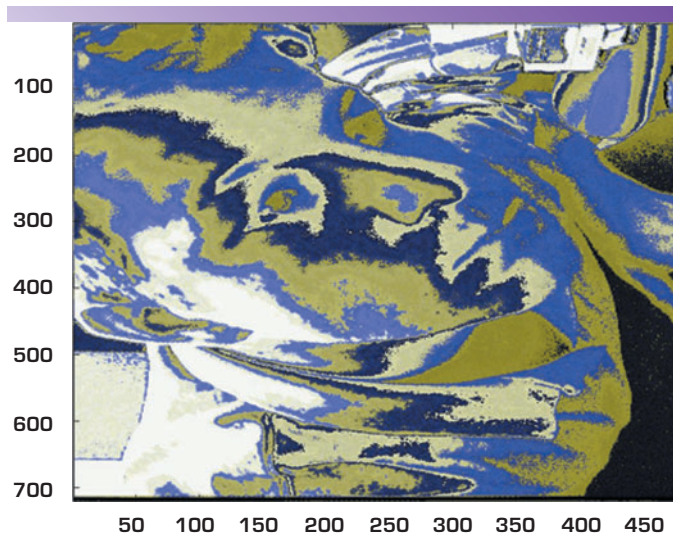


Figure 1. Illustration of FPGA providing new ways to process and display real-time information.

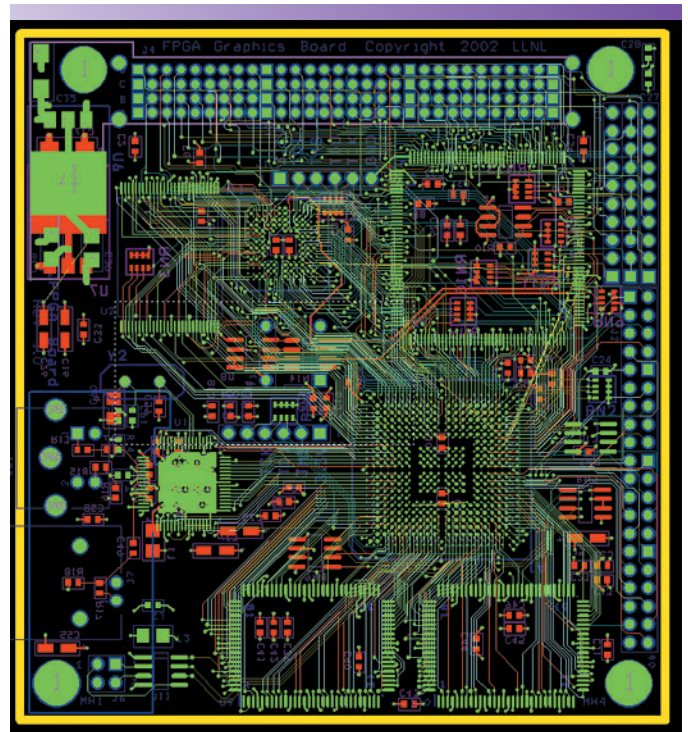


Figure 2. LLNL's reconfigurable video accelerator board.

A network consists of transmitting nodes (which maintain knowledge of position) and receiving nodes (which have unknown positions) distributed randomly in an area of approximately 100 m². Transmitters determine receiver positions through time-of-flight ranging and data communication.

The primary element in a ranging transaction is precise timing. Encoding UWB signals provides unique radio identity (ID), allowing ranging to take place as accurately as possible. As shown in Fig. 1 (a), a transmitter sends its code c_i to the receiver node, which replies with its own code. Upon receiving the reply, the transmitter extracts the receiver ID code and time-lapse information to calculate the range.

A transmitter maintains range distance information for each receiver node, and shares its current weighted least-squares estimate of distances, R^* , with other transmitters. An actual receiver position estimate can be generated by the transmitters with many ranges. The ranges from multiple transmitters can be combined in a closed-form least-squares position estimate. A graphical representation of this method is in Fig. 1 (b), where the R^* measurements from two transmitters are used to give receiver position. The minimum number of transmitters required for a unique receiver position is three. Two are shown in the figure, but a mirror triangle could be calculated placing the

Communication and Ranging for Node Localization

F. U. Dowla, C. A. Kent

With rapid developments in wireless sensor networks, there is an important need for transceiver position estimation independent of GPS. Range estimation from time-of-flight data is particularly suited for large bandwidth physical links, such as in ultra-wideband (UWB) communications. Assuming an encoded UWB or spread-spectrum physical layer, we generated algorithms and simulation tools to test transceiver position localization. Simulations were produced to determine system characteristics such as position error sensitivities to network geometry, to range estimation errors, and to number of sensor nodes.

receiver outside of the concentric circles; thus three transmitters eliminate ambiguity. The equations are solved simultaneously to minimize equation error in a least-squares fashion.

We investigated the following: What is the relationship between ranging accuracy and position estimation accuracy? Does the position estimate improve with additional transmitting nodes? Can a receiver that has been "located" act as a "pseudo-transmitter" to improve the position estimate of other receivers? Finally, what is the importance of network geometry?

To answer these questions, we applied a MATLAB GUI-based communication and simulation package that allows the user to generate either random or manually defined networks of virtual transmitters and receivers, and simulates the ranging transaction between nodes. The user can specify the error associated with the ranging

package maintains the necessary communications infrastructure, measurement filters, and information sharing algorithms that allow precise measurements. We then calculate position estimates, and record the error in our estimates.

We tested hundreds of random networks of various sizes (from a minimum of three nodes) while introducing uniformly distributed range distance error centered between ± 20 ft, and recorded the error in the receiver position estimate at every time step.

Figure 2 presents data collected from varying both range distance error and number of transmitters. From the correlation between the range and position error we can determine how position error can be kept below ± 10 ft. Preliminary field and simulation experiments indicate that four transmitters are sufficient for robust estimates. When range error rises above ± 100 ft, position error improves with an additional transmitter.

Our work has been successful not only in uncovering answers to our initial questions, but also in laying the foundations necessary to implement our algorithms using recently available UWB radio hardware. Algorithms in this project have been successfully implemented and tested on laptop computers for a related wireless testbed project.

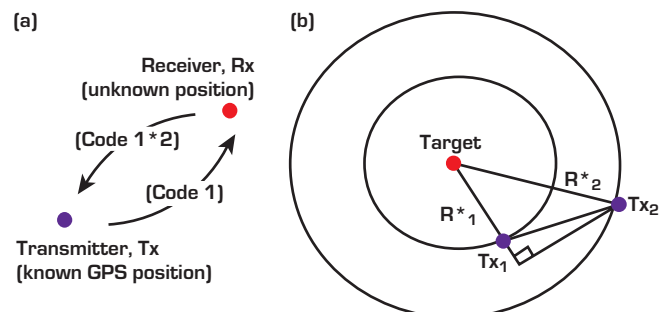


Figure 1. (a) Schematic of ranging transaction. (b) Graphical representation of the closed-form least-squares position estimation method.

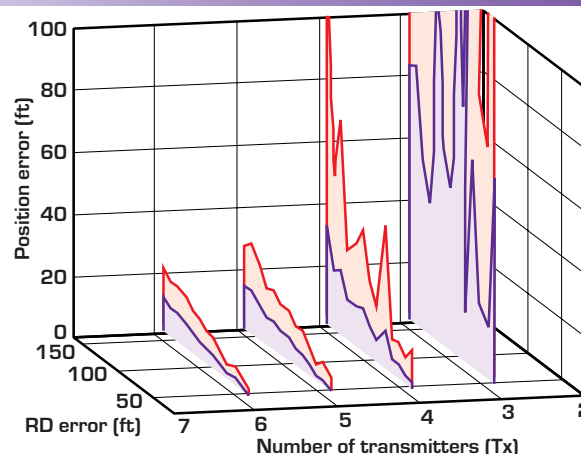


Figure 2. 3-D mean and standard deviation plot of position error as a function of N , the number of nodes, and RD , the range distance error.

In our first year we focused on an object-oriented software framework that allows the distribution of a control system's data processing across multiple CPUs and multiple computers.

The proposal for year two included the following objectives for the distributed control [DistCtrl]

(Fig. 1) framework: 1) making it platform-independent; 2) vectorizing the math processing routines; and 3) mapping processing functions to field-programmable gate arrays (FPGAs). The goals were proportionately scaled-down according to available funding.

When the second year of this project was proposed, the DistCtrl framework ran only on the 32-bit Microsoft Windows platform (Win32). While Win32 is ubiquitous and has very good tools, the target market and proprietary nature of the operating system precludes it from serious consideration in an embedded environment. (WindowsCE, on the other hand, is a Win32-based real-time OS well suited for embedded devices. Unfortunately it has some fundamental problems with applications of the sort DistCtrl targets, notably those requiring large amounts of memory.) UNIX-based OSs have the

Distributed Control System

L. M. Flath

Constructing processing-intensive control systems in the past usually involved writing custom software on proprietary computational hardware, namely digital signal processors (DSPs) and/or application-specific integrated circuits (ASICs). The idea behind this project was to produce an extensible hardware/software framework for the construction of control systems on commodity PCs, resulting in a dramatic reduction in the time and resource cost of such systems.

advantage that once a code base is compiled on one platform, it is relatively straightforward to port it to another. Linux, MacOS X, QNX, VxWorks, and many other operating systems all shared the same UNIX-layer of programming interfaces, even though their respective low-level kernels are completely different.

To this end, a migration path to move DistCtrl onto Linux via MacOS X was carried out. This choice allowed porting to the portable OS interface (POSIX) available on nearly all UNIX platforms. This process involved a fairly elaborate cleanup of year one's code base to permit the simultaneous compilation of the library on Windows, MacOS X, and Linux. As much as possible, platform-dependent code was moved to self-contained modules, the result being a much cleaner source tree.

Threading was changed to the use of POSIX threads (pthreads). Custom spinlocks were replaced by pthreads mutual exclusion (mutex) locks for greatly improved thread safety and performance.

Currently, the DistCtrl framework maintains its functionality on Windows,

is completely useable on MacOS X, and the small changes necessary for compilation on Linux are nearly complete. DistCtrl will thus run on all three major operating systems.

A second benefit of coding on the MacOS X platform is the ease with which vector processing may be incorporated into code. While writing code to the vector unit is essentially at the assembly-level (and thus not platform-independent), it can have an enormous impact on processing performance (see Fig. 2).

Our next task is to compile the code base to the new, extremely high-performance 64-bit platform. We hope that in the future, the DistCtrl framework can be incorporated into the design of many engineering projects, from adaptive optic control systems to real-time data processing pipelines and intelligent image processing cameras.

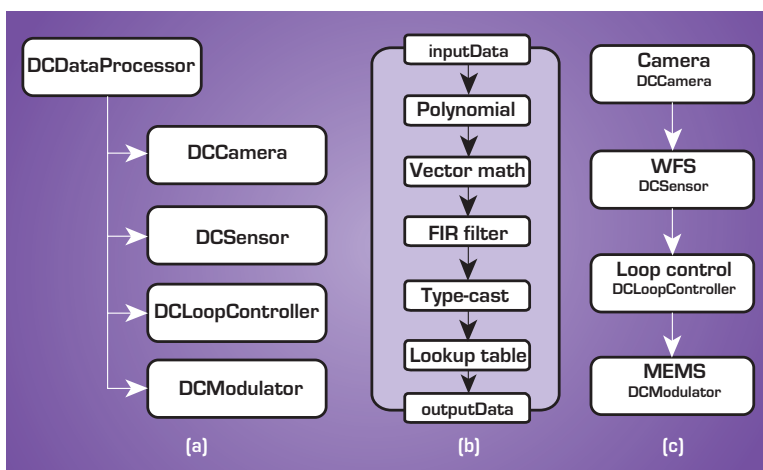


Figure 1. Distributed control framework. (a) Class hierarchy; (b) internal data processing of the root class DCDataProcessor; and (c) example control system.

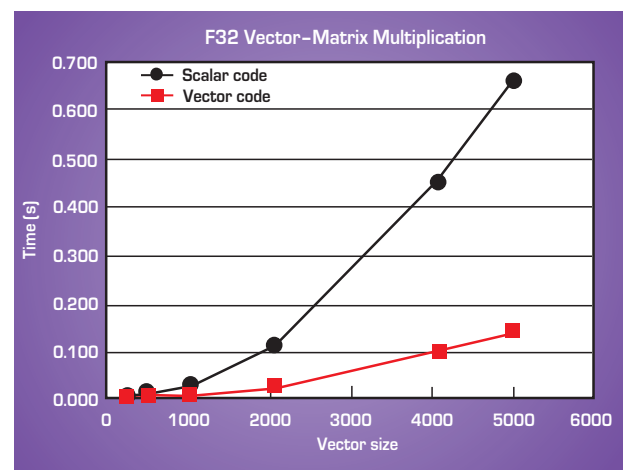


Figure 2. Example of increased performance of a vectorized math routine. This plot charts vector-matrix multiplication for various data sizes. It was performed on an 800-MHz G4 PowerPC under MacOS X 10.2.6.

With the availability of increasingly higher-resolution commercial satellite imagery, it is possible to conduct preliminary vulnerability assessments of large critical infrastructures such as the natural gas pipeline and electric grid networks. The historic problem with using multiple geo-spatial data sets has been solving error propagation and uncertainty inherent in data sets collected by different sources.

Using an existing database from Pacific Gas and Electric Company (PG&E), we have conducted vulnerability assessments of segments of the PG&E natural gas pipeline network, relying on satellite imagery and proprietary data on surface and subsurface PG&E infrastructure. We have coupled the pipeline data with other data sets of population and critical infrastructure. This allowed us to determine the critical infrastructure within the estimated impact zone.

Energy Infrastructure Vulnerability Assessment and Response


J. S. Stewart, A. M. Smith, S. Sengupta, L. E. Clarke;
D. Price (PG&E)

The U.S. energy infrastructure covers thousands of miles, ranging from uninhabited to densely populated areas in most network configurations. The size of these networks makes it difficult to protect from intentional attacks. Originally our plans did not account for terrorist attacks, and thus we are vulnerable in today's environment. Assessing vulnerabilities and security needs requires models that rely initially more on geo-spatial data sets and less on costly field assessments.

The inherent errors associated with merged data sets were also calculated. Our results are being compared to field studies conducted by PG&E to assess the reliability of our technique.

We have also built a simulation model of a segment of the PG&E network that allows us to estimate loss of

service and economic consequences with respect to attacks to nodes within the PG&E system. The simulation model is being calibrated to two pipeline disruptions due to natural phenomena. The simulation portion of this technology-based project offers insights on the relative importance of each segment of the system and helps identify areas that require high priority for system upgrades and protection.

In the second year of this project, we will integrate both the simulation, economic, and image-analysis methods to give us the ability to capture high-resolution imagery of the pipeline and to estimate the vulnerability to a network disruption, and its impact. The figure illustrates the project deliverable. 

Natural gas system	
Sample User Input	
Location of disruption	PG&E 20 San Jose
Estimated length of time for repairs	3 months
New pipeline infrastructure added	Pumping station at...
Sample Output	
Capacity loss	192 MCF
Substitute surface line	Subsurface
Population of end users	423,000
Economic loss per day	1,230,000
Cutoff valve location (miles)	4
Ownership	PG&E
Potential critical infrastructure near site	Hospital
Area type (rural, industrial, urban)	Urban
Cost of pipeline	1,045,000
Estimated time before supply shortage	84 hours
Estimated shortage	16128 MCF
NG power plants MWe	419

Sample vulnerability analysis.



As focal plane technology advances, it becomes increasingly practical to reduce the size and increase the portability of remote-sensing instruments. With miniaturization, the number of applications and usefulness of such instruments will increase. To achieve smaller and more portable instruments, supporting electronics hardware and computing elements must similarly decrease in scale, and power consumption, and increase in computing ability to meet new real-time processing needs.

As our technology-base project progressed, it became more and more apparent that specialized computing devices such as FPGAs and DSPs are the right technologies to further programs such as those involving imaging and hyperspectral remote sensing.

To determine the best-fit solution for any given application, it is necessary to both prioritize criteria and clearly define metrics for evaluating each solution's performance under each criterion. The following criteria are prioritized as follows:

1. Packaging
2. Power utilization
3. Cooling requirements
4. Design time as it applies to general signal processing and remote sensing.
5. Performance
6. Cost.

Without going through a prototype process, it is unclear whether an FPGA by itself will outperform a DSP for real-time signal processing. Given that the functionality of the FPGA is limited by chip size when compared to the DSP, which is limited more by the size and complexity of the program stored in PROM, larger FPGAs may be required to implement a full suite of signal-processing algorithms. It is likely, that given a careful layout of logic circuits, the FPGA would outperform the DSP in most cases.

Field-Programmable Gate Array Chip

E. D. Jones

This technology-base project compares and contrasts two embedded system technologies and evaluates the benefits of each for signal processing and, more specifically, for its applicability to remote sensing. An FPGA-only system, a DSP-only system, and an FPGA and DSP combination system are considered.

Since each FPGA implementation would contain algorithms specific to a particular instrument, new instruments would require redevelopment. But considering the significantly lower development cost of the DSP (in terms of both effort and simplicity, given the number of ready-made signal processing libraries) and factors such as lower cost and power dissipation, the DSP remains the most appealing solution for real-time signal processing.

To meet the packaging, power, and processing requirements, real-time processing (RTP) systems will need to be assembled using combinations of FPGAs and DSP processors rather than bulky, expensive, and less efficient general purpose computing devices.

To produce results rapidly with minimum post processing, remote-sensing instruments must increase the capacity and capability of onboard processing. Instruments that are more self-contained increase portability, range, and function for many of the Laboratory's customers.

Beyond remote sensing, LLNL's Engineering will gain experience and a

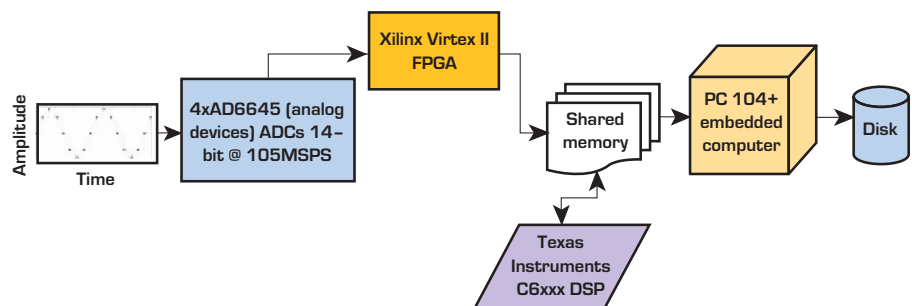
working prototype that can be applied to other situations where similar requirements are the primary concern, and where there is benefit in applying signal processing of analog signals. The block diagram shown in the figure shows a suggested system that would leverage the benefits of FPGA

and DSP technology while minimizing development cost.

The FPGA would control the A/D and timing chips that digitize the analog output signals from the focal plane array, and assemble the resulting data cube. That FPGA may also implement several primary processing algorithms such as non-uniformity correction (NUC), bad pixel detection and replacement, and radiometric calibration. The FPGA would then hand off the data cube to the real-time processing component via shared memory.

The RTP component would consist of a DSP board fitted with a floating-point unit. The DSP processor would generate the results for level 3 processing, including covariance, background estimation, principal components projections, and match filtering.

The final system controller will consist of a PC104 or similar technology, which would serve as an operator console and provide the necessary infrastructure to archive processed data to disk.



Block diagram of a real-time processing system using an FPGA and DSP.

Special Forces, DARPA, DOE, and the intelligence community have a need for the capability to “see” through walls and smoke. Law enforcement first responders, such as Special Weapons and Tactics (SWAT) teams, require a portable, affordable device that will provide them real-time, full motion images of a crime scene through exterior and interior building walls, and through smoke.

The ability to differentiate between perpetrators and victims, and to locate weapons is highly desirable. Ultrasound and ground penetrating radar (GPR) devices could be used to detect moving people behind certain types of indoor and outdoor walls; however, in general, some type of imaging system is needed to generate a 2- or 3-D map of the interior of a room to locate and discriminate multiple people, especially if they are not moving.

Radar Vision

K. Romero, G. E. Dallum, J. E. Hernandez, J. M. Zumstein

Through three years of funding, LLNL's Radar Vision Project has produced a prototype UWB electronically steerable array of radars capable of scanning an arbitrary volume in space in an arbitrary fashion.

GPR is one of the most promising technologies for imaging through walls and finding obstacles through smoke. Nonetheless, in order to get a good quality image useful for shape recognition, an ultra-wideband (UWB) scanning radar system or an array of radars, with suitable imaging algorithms, is needed to obtain a high-resolution Synthetic Aperture Radar (SAR) image of the scene.

The Radar Vision Project system consists of four parts. First, there is an FPGA-based controller board (Fig.1), which calculates and stores all the delays necessary to beam-form on both transmit and receive. Second, there is

an FPGA-based delay board which implements the delay for each transmitter/receiver channel. Third there are the actual micro-power impulse radar (MIR) transmitters and receivers. Finally, we have an automatic gain board, which compensates for attenuation through space on each received signal.

The system is capable of scanning 300 x 400 points in space at a rate of 1 frame/s; resolution in range is sub-centimeter, while in the transverse direction it depends on the aperture of the array. With an array aperture of 1 m, this gives about a 10-cm transverse resolution. A sample setup is illustrated in Fig. 2, with the corresponding raw radar image in Fig. 3.

Based on FY01-FY03 work, this project has provided the groundwork for generating interest from external sponsors.

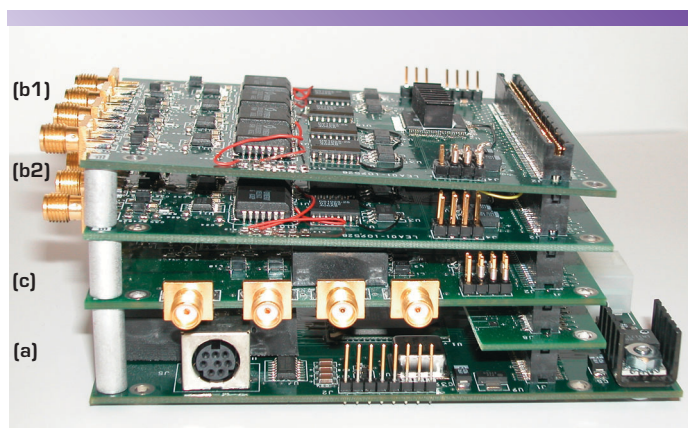


Figure 1. (a) Controller board; (b) delay boards (4 ch/board); (c) gain board (4-ch/board).

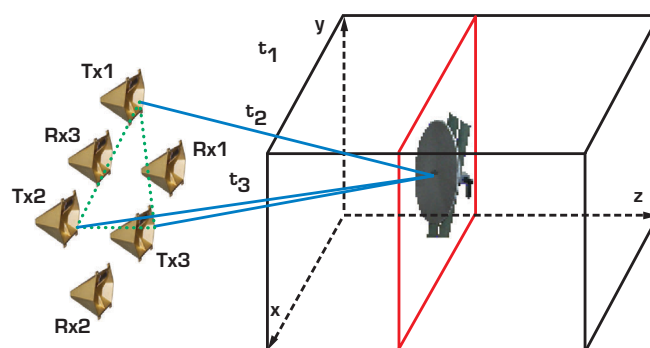


Figure 2. Setup to scan a 30-cm round metal plate, through air at 2 m.

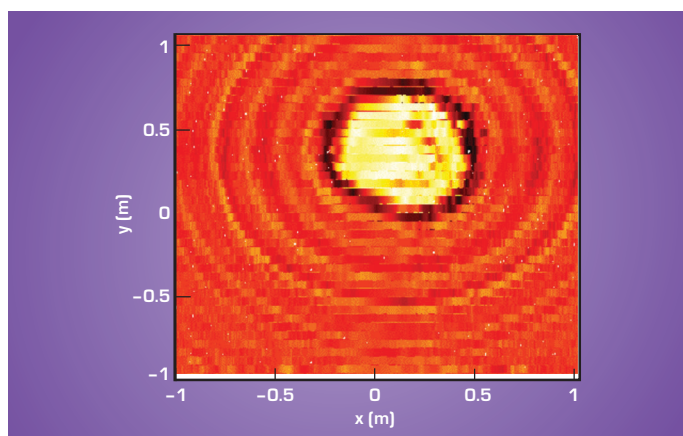


Figure 3. Composite sum of radar returns from 30-cm round metal plate.

Last year we successfully demonstrated a proof-of-principle high-resolution video-surveillance system that dramatically enhanced the resolution and contrast in surveillance images of people, vehicles, and other targets. The problem is that the existing system acquires and processes data far too slowly for most real-world applications. The target must remain still during the 2 to 3 min required for data acquisition, and then there is a wait, from 10 to 30 min or more, for a processed image.

The objective of this new project is to test a real-time implementation strategy for high-resolution speckle-imaging systems.

We began by evaluating technology options for both image acquisition and high-speed image processing. To eliminate the need for the target to be still for minutes, we purchased a video-rate CCD camera and a compatible frame-grabber. It is unnecessary to go much beyond video rates since speckle imaging requires some time (~10 to 20 ms) between frames for the atmosphere to decorrelate.

On the image processing side, although there are a number of avenues that could be pursued for speeding up the image processing, such as digital signal processing (DSP) boards or field programmable gate arrays (FPGAs), we decided to proceed with a multiprocessor, general purpose computer platform. This choice was made primarily to simplify the software implementation, which is quite complex, and to ensure compatibility between computing platforms.

Since taking delivery of the system components, much progress has been made on system integration, interfacing, and image processing software. The figure shows the system being tested outside. The camera and frame-grabber have been successfully integrated into the system and tested. The advertised frame-rate of 34 FPS proved to be true. The user interface allows for full control of the camera

Real-Time Speckle Imaging For Video Surveillance

C. Carrano, D. A. Silva

Atmospheric blurring, sensor platform motion, and optical aberrations reduce the resolution and contrast in surveillance images recorded over long (>0.5 km) atmospheric paths. The resolution loss can be an order of magnitude or more. By overcoming this loss and restoring resolutions to near the diffraction limit, it is possible to identify people from several kilometers, and vehicles from multiple tens of kilometers. This capability is potentially very important for the intelligence and DoD communities, as well as for law enforcement and security agencies.

parameters (e.g., exposure time, gain, offset, and region of interest selection), as well as a live image update for target viewing, alignment, and focusing. To obtain multiple images at full frame-rate requires only the push of a button, after which it is possible to view them, save them, or use them in subsequent image processing.

As projected in our deliverable schedule, our current image processing options include the ability to perform image stabilization. Stabilization, while useful on its own, is actually the first step

performed in speckle image processing. Good progress has also been made on unifying and converting the speckle image processing software into C. The original versions were implemented with a combination of new IDL routines and legacy Fortran code, which, while fine for prototyping, is not optimal for speed. Through this effort, we have already

experienced a tremendous increase in speed and simplification of the image processing steps. For example, to process 30, 1024 - x - 1024 pixel-sized images on a single 1.9-GHz processor now takes between 30 and 60 s, depending on the desired output resolution.

Next year we plan to parallelize the speckle processing software over the four processors, with expected processing times under 20 s for many cases, and perform field testing of the system with static targets. We will also begin to look at slowly moving targets.



Photograph of the real-time video-surveillance system being tested outdoors.

In regions where ground-motion-induced hazards are of concern, such as earthquakes in the San Francisco Bay Area, ground-motion-detection stations have been used to provide simulation input for building location and design. As urban areas grow, large regions, with a diversity of geological conditions, have no ground-motion records that can be used to simulate building response.

Because site response can change dramatically with geology, it is important to expand the knowledge base of ground-motion and building response to include areas where there is no historic data.

Several tools were developed earlier at LLNL that help address this lack of geographic coverage: the program E3D, a geophysics wave-propagation code, and a pilot application, consisting of a geophysics model of Southern Nevada, as well as the nonlinear structural response program, NONLINBLDG.

Regional Simulation of Ground Motion and Building Response

M. A. Gerhard

The goal of this project is a reduction to practice, based on previous LLNL efforts where the basic elements for ground-motion simulation and building response have been developed, producing a cutting-edge tool for building hazard assessment.

This technology-base project constructed a practical and user-friendly interface for expedient execution of the codes. E3D had already been modified to include spatial information, and the program NONLINBLD had been modified to perform parallel structural analyses using the ASCII computer systems.

We changed the name NONLINBLD to NEVADA and modified it to extract building inter-story drift values (relative horizontal displacement between building floors) as a measure of damage hazard. We compiled a library of legacy ground-motion inputs (hundreds of records) and a library of E3D results, each of which contains over 60,000 ground-motion records distributed

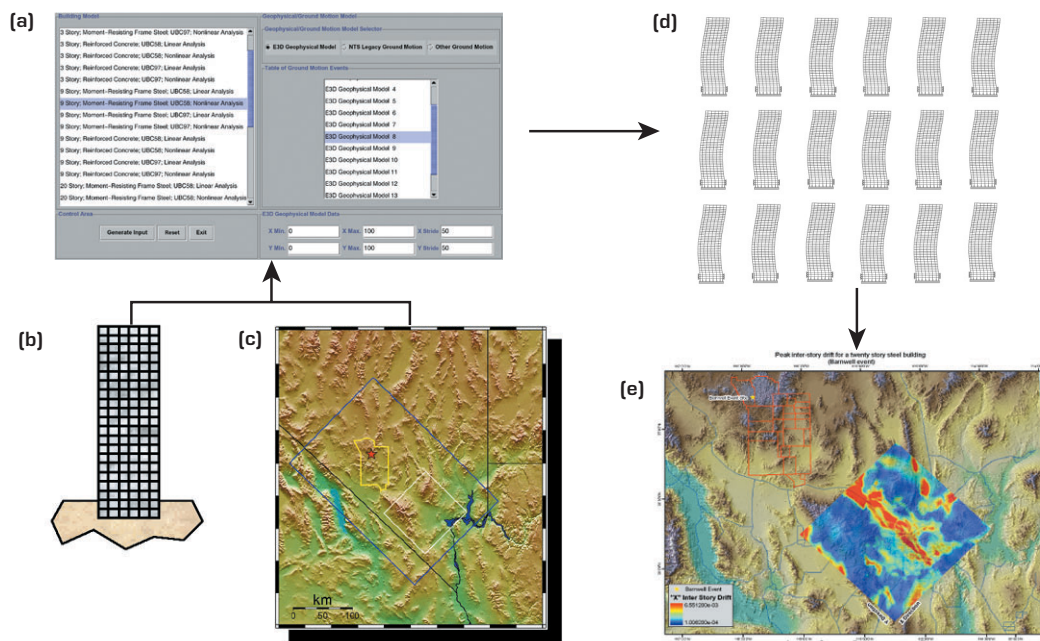
over 60,000 km². We also built a library of building models, including 3-, 9-, 20-, and 40-story structures.

A principal product of this technology base is a graphical user interface [GUI], (Fig. (a)), to manage the large data bases associated with these models. The GUI is used to select a building model

from the library (Fig. (b)); to select ground-motion inputs, either from an E3D analysis (Fig. (c)), or from the library of legacy records; and to prepare the necessary input files for the parallel structural analyses (Fig. (d)).

The user submits the analysis job on an ASCII computer system, and then runs a program that gathers the damage hazard values for each ground-motion location, allowing the generation of a spatial representation of the building response (Fig. (e)).

This technology-base project produced a new capability in the area of natural hazard analysis, such as earthquake analysis. It is also of particular interest to national security programs.



(a) Graphical User Interface showing selection of (b) building model, and (c) E3D regional model; (d) inputs for parallel analysis (hundreds to thousands); (e) map of the damage hazard values (inter-story drifts).

Most adaptive optics (AO) systems use sub-images of a point source to do wavefront sensing (WFS) to estimate the phase aberration, which is then corrected in real time. In the first year of this project we established the feasibility of using sub-images of an arbitrary scene instead. This method uses correlation between a sub-image and a reference (which can be another sub-image) to estimate the phase slope. It is termed scene-based wavefront sensing (SBWFS).

In FY03 we made several advances in understanding the applications of this technique. Our primary focus was applying this technique to remote imaging systems over short horizontal or slant paths. We also put our rigorous analytic predictions of algorithm performance to the test in a controlled experimental setup. We produced enhancements to algorithm performance in noisy situations or with moving objects, and discovered that some point-source AO systems have points that are more like scenes, enabling improved WFS performance with this algorithm.

We studied the remote imaging scenario of an 8-in. (20-cm) telescope with 8 sub-apertures across the pupil. This allows 2.5-cm lenslets, roughly comparable to the spatial scales of the atmospheric turbulence. Detailed incoherent imaging simulations of this scenario were carried out, using scenes acquired with a digital camera. These simulations show that 1) phase aberrations near the object warp image structure; and 2) phase aberrations close to the pupil simply shift the sub-images, allowing easy detection and phase reconstruction.

Figure 1 shows a WFS image and the actual phase aberration and reconstructed phase. Given the low number of sub-apertures, the reconstruction is close to a low-pass filter on the phase. Radiometric analysis of this scenario showed that adequate amounts of light will be present. This was confirmed with

Scene-Based Wavefront Sensing for Diverse Applications

L. A. Poyneer, K. N. LaFortune, B. J. Bauman, C. W. Chan

Scene-based wavefront sensing is a technique for using arbitrary images for wavefront sensing in adaptive optics. Four advances are discussed: the application of the technique to remote imaging along short paths; experimental verification in a testbed; algorithm enhancements to improve dynamic performance; and a valuable application to point-source AO systems.

initial field testing using a lenslet array on a 20-cm telescope. In bright sunlight along a 500-m path, the mean individual pixel SNR was 83 for a 2-ms exposure, and 45 for a 1-ms exposure of a highly reflective target.

The core SBWFS algorithm has performance dependent exactly on scene content and illumination type, and this performance is largely predictable from a single low-noise copy of the image.

We studied SBWFS in a testbed that featured adjustable scenes displayed on a high-resolution monitor and a MEMS mirror to add aberrations. This set-up confirmed the inverse-power-law scaling of error variance with SNR and predictions of scene performance based on content.

Though in any single time step all sub-images have the same scene content, temporal variations due to either platform

or target motion can decorrelate sub-images through time. Two approaches were taken to improving robustness. First, a fast algorithm that detects moving pixels was successfully applied. Based on short-term temporal variations in pixels, the algorithm identifies when scene content is changing. This method is robust down to the same

SNRs as SBWFS. Second, study was made of algorithm enhancements in low-SNR situations. Incorporation of low-pass filtering into the algorithm improves slope estimation performance at low SNRs.

The SBWFS algorithm works with arbitrary scenes, provided that the sub-image and reference are well correlated. Point sources can have significant structure variations due to high-order phase aberrations and background, which lead to incorrect estimates with traditional center-of-mass algorithms.

Shown in Fig. 2 is a series of WFS spots formed by the Solid State Heat Capacity Laser AO system. SBWFS has real potential to be a more robust WFS method in this case, because, using a well-formed spot reference, it correctly locates the central core of the spot, regardless of the other structure variations.

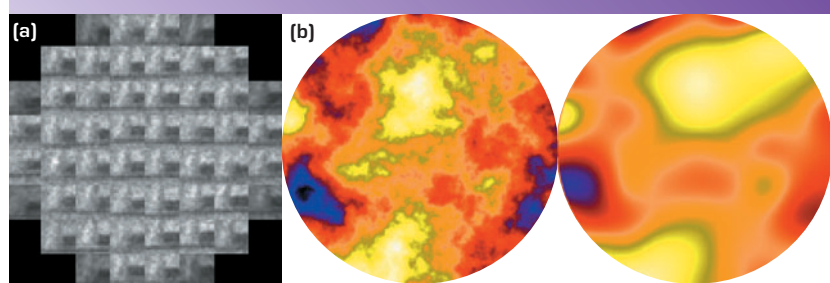


Figure 1. (a) WFS image. (b) Actual phase aberration and reconstructed phase.

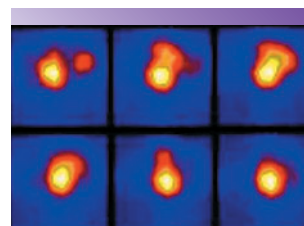


Figure 2. WFS spot from a single sub-aperture, six consecutive laser shots.

By incorporating measured data from a real structure, a computational simulation model can be modified or updated so that it captures the actual behavior of that structure. To this end, we have produced algorithms for the system parameter identification of very large-scale mechanical and structural systems. These algorithms, based on a Bayesian inference procedure using a Markov Chain Monte Carlo (MCMC) sampling process, solve nonlinear inverse problems (*i.e.*, determining the physical model that corresponds to the observed output).

The MCMC process is used to integrate vibration signature data into an initial-design finite-element model to produce an “as-built model” that corresponds to a specific structure and can simulate its characteristic behavior. Quantitative estimates of both individual parameters and system-wide states of the structure are determined. A key feature of this methodology is that it can be used to specify and locate changes, due to damage or aging, in the real system. This project is an outgrowth of LLNL’s Stochastic Engine (SE) project for simulating geophysical environments. We have successfully demonstrated that the general, computational mechanics code, NIKE3D, can be used as the forward model in the SE process.

In FY02, we began with a uniform, linearly elastic, fixed-free cantilever beam. The SE algorithms were applied to identify the configuration and determine up to two flaw locations on the beam in terms of its stiffness matrix. In “virtual experiments” (simulation data instead of measured data) using applied force (input) and static nodal displacement measurements (output), we investigated the following issues: 1) accuracy in sampling the posterior distribution; 2) robustness under degraded conditions, including noisy data, missing data, model misspecification and an incorrect prior distribution; 3) characteristic behavior under

Vibration-Signature-Based Modeling and Simulation

R. E. Glaser, C. L. Lee, W. G. Hanley

With the availability of increasingly powerful computer hardware and sophisticated simulation software, it is commonplace for engineers to perform the design and analysis of mechanical systems and structures using very large-scale computational models. The degree to which these models compare to the actual systems and structures they represent depends on inherent modeling assumptions. For example, uncertainty in material properties, actual geometric detail, or the nature of interconnects degrade the accuracy of numerical simulations.

state-space misspecification; and 4) sensitivity and accuracy related to spatial domain discretization. Two possible mesh sizes, 10 elements and 8 elements, were permitted.

In FY03, we generalized and expanded that work to make two improvements. The first is to allow up to four flaw locations. Sampling issues arise when more than 50% of the elements are flawed. Although a more complicated sampler would address those issues, we were satisfied that the algorithm had the

ability to handle any number of flaw locations. The second improvement was to allow for a more realistic, continuous, randomized change in element stiffness. This required the removal of the reversibility condition on the proposal Markov chain.

Results shown in Figs. 1 and 2 demonstrate the success of the new algorithm at locating and identifying flawed elements of the cantilever beam.

From a representative run, the pie chart shows 95.4% of the posterior probability consists of predictions that are completely correct in terms of mesh density, number of flaws, and location of flaws. The bar chart summarizes the distribution of the percentage error, in terms of stiffness, of the predicted flaws. The maximum error is less than 15%, with more than 70% of the samples yielding predictions having less than a 10% error rate.

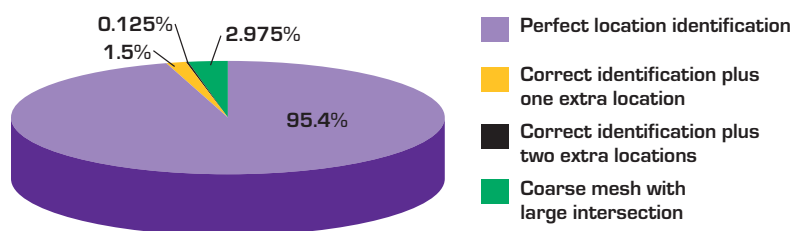


Figure 1. Identified flaw frequencies.

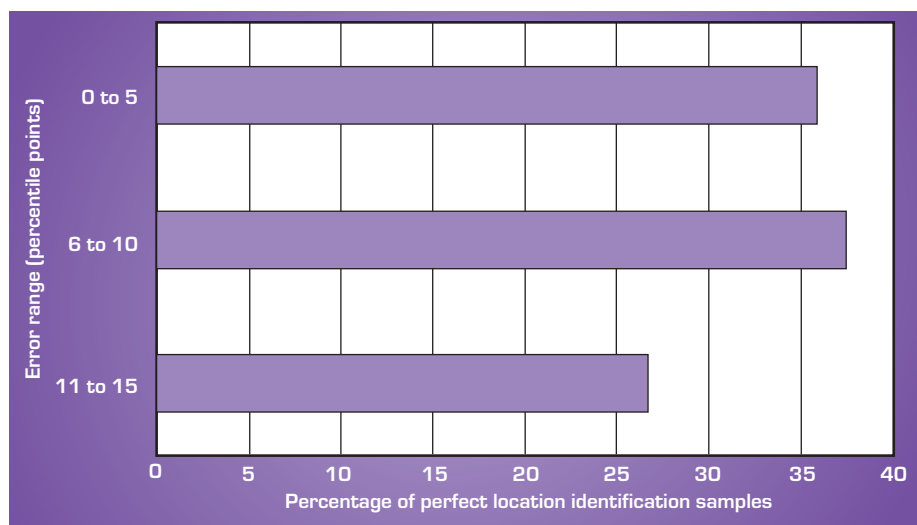


Figure 2. Analysis of average absolute stiffness error.

There is a concern that current collection systems are unable to detect ultra-wideband (UWB) systems. Further, UWB arrays could easily defeat narrowband collection. We are taking a new approach based on searching the 2-D space to defeat wideband arrays. We are studying how arrays can be used in conjunction with time-domain signal processing to implement data collection systems.

We have adopted a three-pronged approach to UWB communication waveform data collection. Two of them rely on waveform temporal vulnerability — its impulsive character in time, which was addressed last year, and its spectral signature, which is addressed this year. The third aspect addressed this year is the array focus spot size, which

Wideband Antenna Arrays for Electronic Countermeasure

A. Spiridon, F. U. Dowla

The focus of this project is antenna arrays for electronic countermeasure for the detection and interception of adversarial wideband communication and radar systems.

determines the spatial resolution of the emitters, and the speed at which the space is scanned.


To complete the vulnerability analysis the interplay of spatial and temporal decrements is briefly examined. In addition the vulnerability to interception of the UWB pulse waveform spectrum was evaluated. This provides a base for selecting the UWB communication signaling waveform, to improve its covertness.

Most of the effort this past year has been on analysis and computer numeric simulation of field signals emitted by

the arrays, properly augmented with experimental data to reflect accuracy of control of pulse shape and time. Key issues addressed in the effort are 1) identification of the architectures of arrays, including topology, and 2) analysis of bounds

on beam focus spot, defined by 3-dB off-peak energy point.

We have also collected a limited amount of data on multipath, and on the background interference, to assess their impact on data collection.

In FY03 we completed three independent characterizations of the beam focus spot size: 1) numeric simulation; 2) closed form equations, and 3) experimental validation. The results from all three methods agree, as illustrated in Figs. 1 and 2. The spectral signature of waveforms was also completed. 

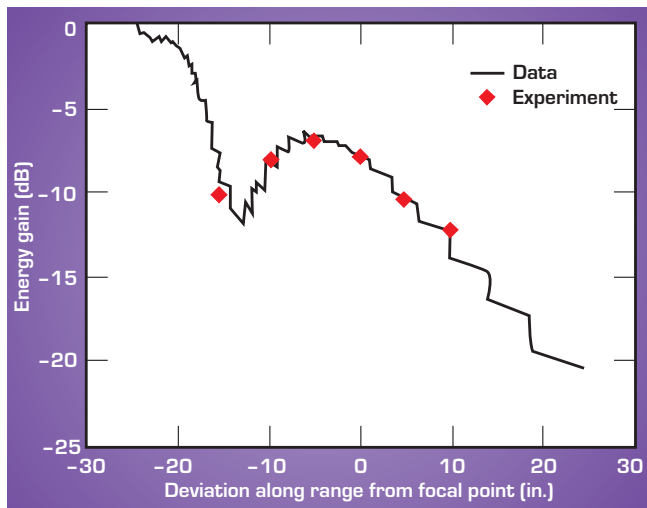


Figure 1. Experimental validation of equations for prediction of spot size.

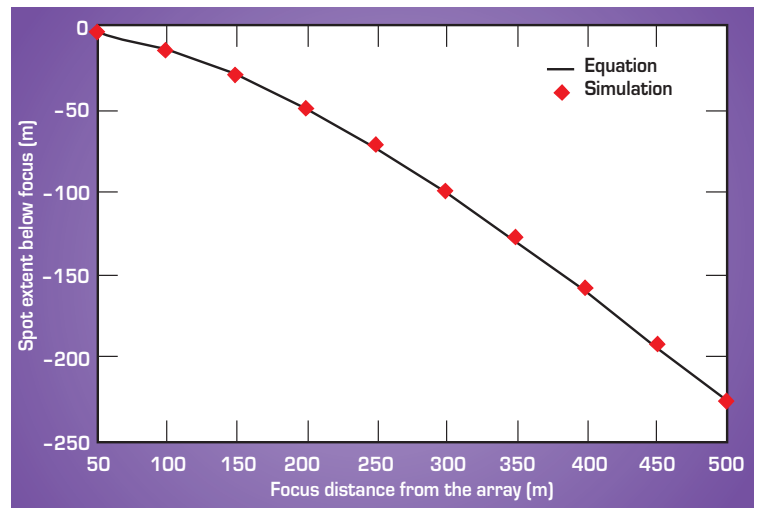
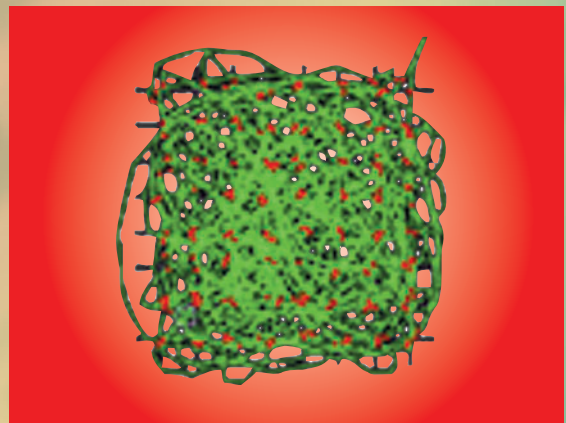
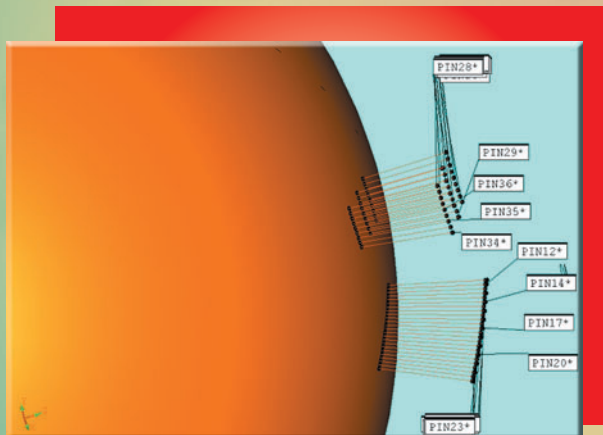
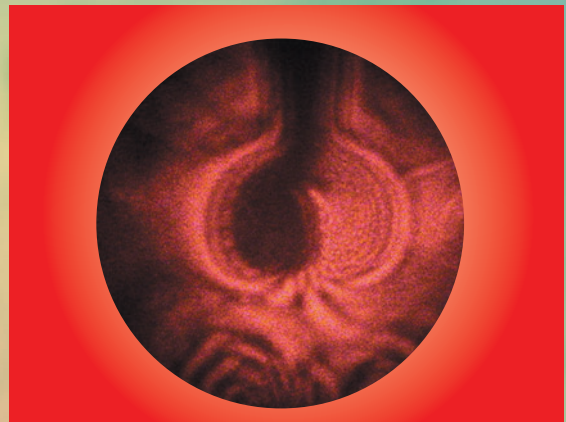
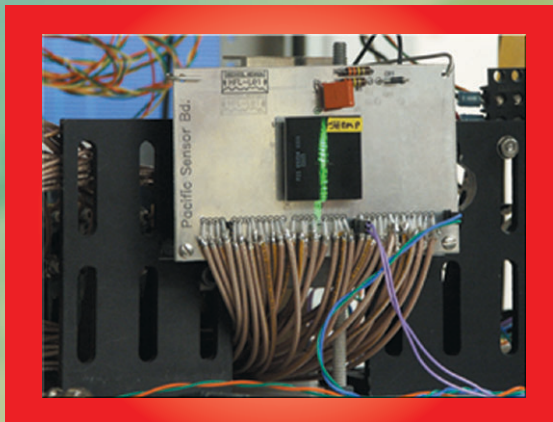


Figure 2. Simulation validation of UWB spot size.

Other Technologies



The original plan for this project was to perform the dynamic fracture experiments using LLNL's 2.5-in. gas-gun facility. However, since it will be some time before the gun is made available, we have made use of a high-speed forging system for conducting the tests. This forging ram is currently used to perform Split Hopkinson Pressure Bar (SHPB) experiments and, after some simple modifications to the perpetrator, can provide "projectile" (ram) velocities sufficient to conduct dynamic fracture tests at the low and intermediate range. In relation to the gas gun, the forging system is a slightly safer means of initiating dynamic fracture, since the ram is not a free projectile that must be captured.

Much of our effort this past year has been devoted to the necessary engineering safety controls and modifications to the facility. For our experiments we are using a coherent 6-W CW argon laser, which requires 480-V, 3-phase power and a high-flow-rate water cooling line.

Dynamic Fracture Mechanics Experiments

S. J. DeTeresa, C. K. Syn, G. J. Larsen

The goal of this project is to bring state-of-the-art experimental capabilities to LLNL for full-field, real-time studies of dynamic fracture, to be used in support of Laboratory needs for advanced computer simulations of material behavior. This capability will provide measurement of dynamic fracture toughness, crack velocity, and fracture mode transitions.

A photo of the laser interferometric imaging system is shown in Fig. 1. The advantage of the enclosed beamline is the portability of the laser imaging system for use with other types of dynamic fracture experiments in other facilities.

The imaging system was completed this year by procuring and bench-testing a high-voltage pulser and digital delay/generator to drive the Pockels cell for synchronous illumination of the fracture event. We also built several mounts for optics, beam expander, and gratings to fit the laser imaging system in the enclosure.

Our original goal was to purchase a modern high-speed framing camera to capture images, but the opportunity for capital equipment funds never materialized.

Instead we evaluated two existing older technology cameras and decided to work with the one dedicated to SHPB testing. This camera required an upgrade to the rotor's synchronous pulse output. We also improved our ability to produce high-speed images by obtaining approval for our own film developing process.


To align the beamline and optimize the timing of the high-speed imaging, we built a portable, static-loading fixture for fracture specimens. This fixture is used to capture a static interference pattern during set-up of the imaging system, thereby avoiding the need for many fracture specimens. Specimen preparation techniques were also completed. A fixture for conducting fatigue pre-cracking was constructed and several steel specimens were pre-cracked. We also have worked on polishing techniques for these pre-cracked specimens, which achieve the mirror finish required for imaging the interference patterns on an opaque material. An example of a static pattern on a steel specimen is shown in Fig. 2. 



Figure 1. Coherent 6-W laser interferometric system with beam-line enclosure (top panels removed for photo).

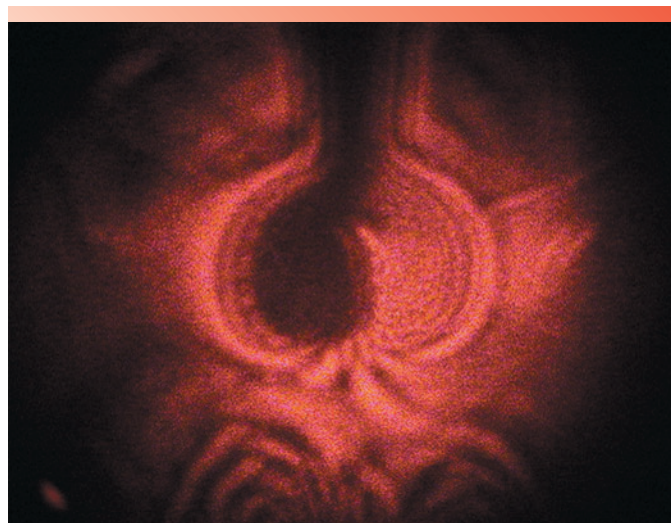


Figure 2. Interference fringes at crack tip for statically-loaded, pre-cracked steel fracture specimen.

Our goal is to produce a printed circuit board (PCB) that meets the needs of the W87 JTA wireless telemetry system, but also can be used as a general board for DSP, signal generation, and ADC recording.

There are two major components of the wireless transmitter: 1) the digital modulator, and 2) the RF front end. Figure 1 is the simplified block diagram of the PCB fabricated and assembled for this project.

The digital modulator motherboard (MB) is a 12-layer, mixed-signal 12-in.-x-13-in. impedance-controlled PCB that includes one 575-pin, 2-million-gate field-programmable ball-grid array (BGA) that can operate at a logic speed of 400 MHz; one 560-pin, 1-million-gate field-programmable BGA for diagnostics; serial interface; large memory buffers; a 1-Gsps DAC; a low-cost 320-Msps DAC; a 400-Msps DAC; a very high-speed

High-Speed Digital Transmitter

B. N. Tran, H. Pao, R. J. Kane

There is a need for a low-cost and power-efficient high-speed wireless transmitter, upward of 100 Mbps data transfer rate. Our goal is to apply our patented, Digital IF QAM Modulation system, using parallel processing, which uses off-the-shelf FPGAs, to demonstrate the functionality of a wireless transmitter at 200 Mbps.

synthesizer, up to 900 MHz; and a high-speed ADC interface.

The digital modulator MB takes the sensor's serial data bit stream, converts it to parallel data, maps the parallel data to QAM [quadrature amplitude modulation] format, and modulates the data, which are then sent to the very high-speed DAC or an analog device DAC for conversion. The analog data is then fed to the RF front end for further filtering, amplification, and carrier up-conversion to 2.2 GHz, prior to transmission at the antenna.

The RF front end is a single stage up-conversion that can provide a gain of

about 50 dB. It is a 3-in.-x-5-in. impedance-controlled PCB that includes a 10-MHz to 2.2-GHz synthesizer, a mixer, filter, and various amplifiers. It is simplified to one stage since the digital modulator MB takes care of the IF modulation. Figure 2 shows the digital modulator PCB and RF PCB. The RF front-end module is mounted on the digital modulator PCB.

The RF front-end output data is recorded in Fig. 3. The input data is from a signal generator at 74 MHz 64-QAM modulation. The output frequency is measured as 2.244 GHz, with very clear eyes, constellation, and about 3.5% error vector magnitude. The measurements confirm that the RF front end meets our performance goal.

The next challenge is to fully integrate the digital modulator MB and RF front end and test the high-speed transmitter running at 200 Mbps in a practical environment.

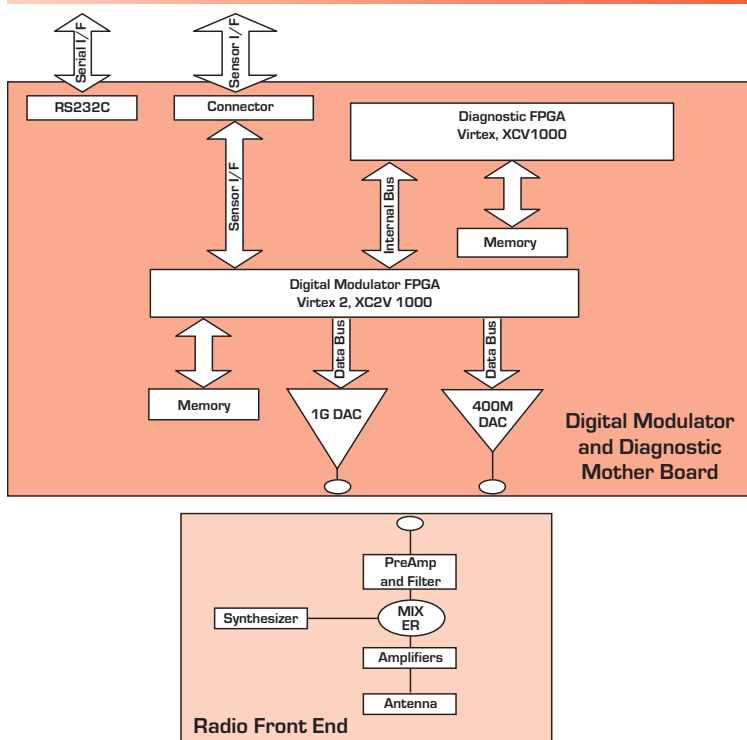


Figure 1. High-speed transmitter device.



Figure 2. Digital modulator and RF PCBs.

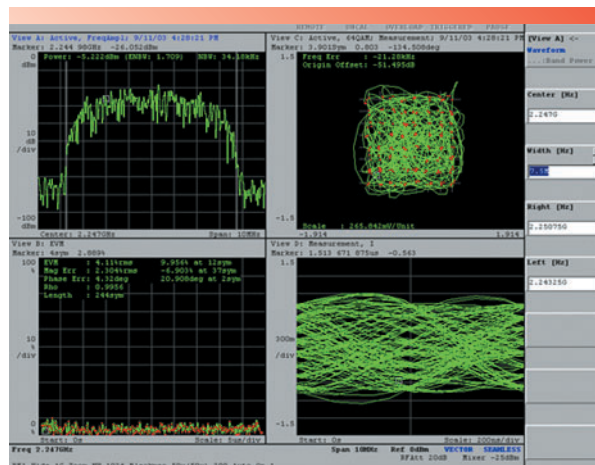


Figure 3. 64 QAM RF data output at 2.244 GHz carrier frequency.

MBI is essential to a modern manufacturing organization. It is a process that leverages solid modeling technology to replace 2-D detailed drawings. Fast, accurate, and cost-effective inspection is required to verify the manufacturing process. MBI technology is mature, but inspection tasks are still heavily dependent upon manual data input and an obsolete CAD/CAM system.

We have established PC-DMISTM as the preferred coordinate measuring machine [CMM] operating system. PC-DMISTM is certified, ensuring that the mathematical algorithms used adhere to known standards. PC-DMISTM provides direct and seamless integration with Pro/E models, eliminating translation and maintaining the

Model-Based Inspection

P. E. Ahre, C. C. Garrett

The Model-Based Inspection (MBI) project has built on the capabilities of LLNL's Model-Based Manufacturing project, by integrating the inspection of completed parts into the process. MBI produces higher quality results at less cost, through reduced human interpretation, data entry, and improved technology. MBI also provides a service to our customers by reducing their need to produce time-consuming detail drawings of their parts. The final product is the capability to accurately and effectively inspect precision parts using Pro/E models in a paperless, model-based environment.

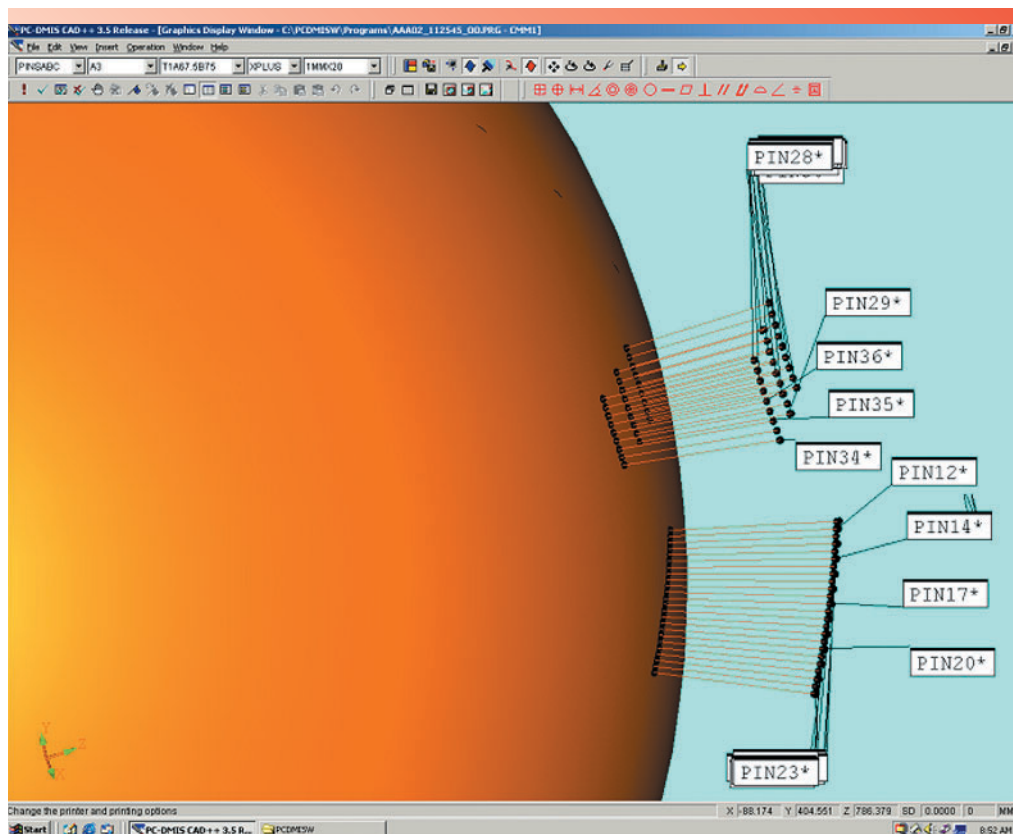
original design intent throughout the measuring process. PC-DMISTM has the versatility and comprehensive programming capability required for an R&D environment.

LLNL inspectors have been trained by the PC-DMISTM vendor, and will continue to enhance skills, inspection techniques, and procedures through practical application, to ensure the quality of the MBI process.

Our MBI system consists of an active CMM, a PC-DMISTM license, and two LLNL networked controller PCs. PC-DMISTM provides a serial license key allowing installation on multiple computers. A networked controller is essential for efficient file/model transfer, allowing download capability from the Engineering Records Center, FTP sites, and online databases. To provide complete LLNL customer support, classified and unclassified capability is required. A practical application of an imported model is displayed in the figure.

This technology-base MBI project also supported, in part, an effort to provide improved capabilities with our CAD/CAM inspection programming.

In FY04 we will begin implementation on programmatic work.



Imported model as viewed from PC-DMISTM.

Our approach, illustrated in Fig. 1, tracks the flight vehicle using the differences between the arrival times of the telemetry signal at pairs of receivers whose locations are known. This method, known as time-difference-of-arrival (TDOA), has been used, traditionally, to locate stationary transmitters. It is passive, and exploits only the external signal structure, not the information encoded within the signal. To first order, the accuracy of the TDOA method depends on the signal bandwidth, the received signal-to-noise ratios, and the geographic distribution of the receivers. References to the work on which our approach is based will be provided by the authors on request.

The TDOA approach requires no modification to the existing on-board instrumentation or telemetry hardware. Because only time-difference measurements are used in the processing, it is not necessary to add an absolute time code to the telemetry signal. Consequently, there is no need to deploy a precision clock onboard the vehicle. Also, since we do not require direct measurements of azimuth and elevation angles, the receiving antennas need be only sophisticated enough to receive the telemetry signal with an acceptable signal-to-noise ratio.

In the basic formulation, we estimate a discrete sequence of spatial coordinates $[x_i, y_i, z_i]$ for the flight vehicle along its trajectory. Each position determination is based on one set of TDOA measurements from N ground-based receivers. There are two processing steps. First, the received signals are associated in pairs and processed to determine a set of TDOA measurements. One set of TDOA measurements consists of the differences in arrival times between the signals in each pair. There are

$$\binom{N}{2} = \frac{N!}{2!(N-2)!} = \frac{N(N-1)}{2}$$

Passive Tracking of Flight Vehicles Using Telemetry-Signal External

M. R. Portnoff, R. J. Kane

Missile flight tests are routinely monitored using networks of tracking radars. However, there is now a desire to supplement these radars with a complementary technology. This project explores the use of passive geolocation techniques to track the flight vehicle by exploiting the reception of its telemetry at a set of ground-based receivers. Initially, we would use the telemetry signal in its current form. If assessed to be beneficial, optimized "synchronization bursts" could be added to the telemetry in the future.

such measurements, from which a subset of at most $N-1$ measurements are independent.

The second step is to solve for the flight-vehicle coordinates $[x_i, y_i, z_i]$, given the i^{th} set of TDOA measurements. Since N receivers produce a set of $N-1$ independent TDOA measurements, a minimum of $N = 4$ receivers are needed to determine the three unknown coordinates $[x_i, y_i, z_i]$. Measurements from more than four receivers, or for the case of noisy signals, redundant dependent measurements, can be incorporated using a least-squares formulation. The flight-vehicle location is determined by minimizing the mean-squared error between the measured arrival-time differences and the arrival-time differences computed from the estimated location. The resulting equations are nonlinear and can be solved iteratively. Although the iterative solution is computationally complex, the

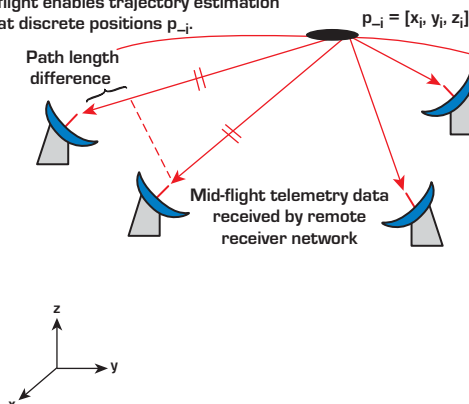
real difficulty is that the solution often converges to a local minimum (far from the true location) unless we start the iteration with a very good initial guess for the location.

It is possible to introduce an additional variable and reformulate the minimization equations in a way that allows them to be solved in closed form as two systems of linear equations plus one scalar quadratic equation in the

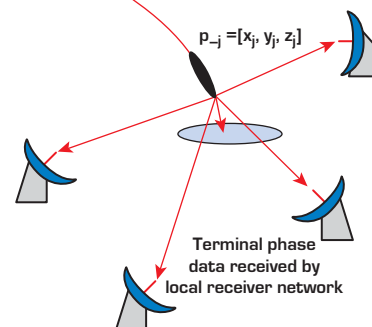
new variable. More importantly, physical considerations determine which root of the quadratic equation corresponds to the correct position estimate. Thus, the problem of our solution converging to a local minimum is avoided. From a strict mathematical viewpoint, this closed-form solution minimizes an "equation error" rather than the true "model error." In practice, this distinction may not be significant. If necessary, however, the closed-form solution could be used as an initial guess for the iterative solution that minimizes the model error.

During the first year of this project, we concluded our analysis and tested our TDOA solution on simulated data. We plan to collect real data and demonstrate our approach on them on future flight tests. In the near term we can use signals of convenience, aircraft or mobile-radio transmissions, and then apply the method to systems surveillance tests.

Reception of telemetry during mid flight enables trajectory estimation at discrete positions p_{-i} .



Reception of high bandwidth terminal-phase data transmission supports increased accuracy due to reduced range and increased signal bandwidth.



Geolocation of missile flight vehicle using TDOA.

X-MIDAS, the basis of this telemetry processing capability is a signal processing and hardware control application that runs in a UNIX/LINUX environment using a command-line input approach.

Two goals were in mind when choosing this approach: 1) use an approach known to be capable of the required signal processing; and 2) create a skill base in the software processing of radio signals.

In FY03 the computer hardware was assembled. It is a PC-based system running RedHat LINUX 7.x and the X-MIDAS application. Data was acquired using a digitizer card in the PC to exercise software and start demodulation implementation. A general communications receiver with a 20-kHz demodulated bandwidth output was used to select the desired radio frequency signals. Signals with well-known structures were acquired; these included the amplitude-modulated digital time code from WWV, narrowband binary phase-shift-keyed (BPSK) and frequency-shift-keyed (FSK). These modulations are common amateur radio signals in the 14-MHz and 144-MHz bands.

RF Telemetry Processing Using Software-Defined Radio Approaches

R. J. Kane

This project has demonstrated the use of a software package called X-MIDAS, which could be integrated into a "software radio" for telemetry data acquisition and processing.

The X-MIDAS software was used to perform transformations on the signals acquired from the receiver. Noise present in the RF channel was removed using bandpass FIR filtering. Different algorithms were required for the final demodulation of the three different signals. The WWV time code signal is a pulse-width-modulated signal that allowed a simple envelope detection process to be used. The FSK signal was demodulated using two different methods: filter slope detection, and filtering.

In the first instance a low-pass filter was designed with its transition band including the FSK signal band. Passing the data through this filter results in an output signal where the lower FSK frequency is at a point in the transition band with less attenuation, and the data is passed with little attenuation.

Conversely, the higher FSK frequency is attenuated more, and it has a lower signal level at the output of the filter. This process is referred to as "slope detection."

A higher performance approach is to use a zero-crossing detector and to measure the time period between crossings. This approach allowed the

frequency shift and corresponding data bit to be determined by the time period measurement. Optimal demodulators exist but were beyond the scope of the effort at that time.

BPSK signals were the modulation format of greatest interest. This modulation is commonly used where robust communications are required. The BPSK signals processed using X-MIDAS were narrowband and with low data rates, but since the data acquired were not processed in real time the original rate is not an issue.

Processing of the BPSK signals used quadrature down-conversion and FIR filtering of the in-phase and quadrature-phase outputs. The resultant signal allowed the data within the signal to be detected by examining the 180° phase shifts corresponding to binary data stream transmitted.



Devising a practical solid-state alternative to a streak camera has been enabled by new technologies including inexpensive, multichannel, high-gain, solid-state detectors, and inexpensive, high-performance digital recorders. In this final year of a technology-base project, a fully integrated streak camera surrogate system was demonstrated successfully.

The Digital Fabry-Perot (DFP) system is a second-generation prototype, and demonstrates all of the characteristics required for a diagnostic appropriate for fielding as part of a hydrodynamic experiment.

Our device will provide up to 64 spatial channels, temporal resolution of 10 ns, and a record length of 10 μ s. The building of this device was motivated by cost, durability, and simplicity.

The experimental arrangement for the DFP included an explosive bridge wire driving a foil with high acceleration. A high-voltage pulse from a capacitive discharge unit (CDU) explodes a bridge wire, which typically comprises the first stage of an HE detonator. In our case, there is no HE, but we need a reflective surface that accelerates with characteristics similar to an HE-driven event. While the

System Architecture for High-Speed Transient Diagnostics

G. P. Le Sage, B. N. Tran; E. P. Daykin, G. Perryman, C. Perez, R. Eichholz (Bechtel Nevada)

A new, all-solid-state data acquisition system has been built and tested that can replace the streak camera in Fabry-Perot (FP) velocimetry systems. By providing an inexpensive, robust alternative to the streak camera, the new system will allow increased channel count for FP velocimetry experiments, and will become part of a compact FP system envisioned to fit entirely within a rack-mounted chassis.

foil does not move as far as an HE-driven object, and the transient record is only a few microseconds, the Doppler-shifted light has similar characteristics to an actual hydro experiment.

For the FP velocimetry system, the solid-state streak camera equivalent device also involves some compromises. Since velocity data is derived from the location of interference fringes, the required dynamic range required is very low. Basically, the fringe is either at a given location or it is not. Ultimately, a 1-bit digital system can directly record the FP fringe data. The low dynamic range is not ideal, but it is a reasonable compromise for recording a single velocity object.

The first prototype system was based on a commercial photomultiplier tube (PMT) with a linear array of 32 anodes. The PMT outputs were quantized [threshold detection] and passed to an array of 32 digitizer channels controlled

by a PC. The 32 separate digital records are processed and recombined to produce the image shown in Fig. 1.

The second-generation DFP system replaced the multichannel PMT with Avalanche Photodiode [APD] arrays. Each array had 16 channels; four arrays were used in parallel.

The APD was followed by a differential amplifier stage, a bias level adjustment stage, and a discriminator circuit. The discriminator output is a two-state system, and the output of this device directly drives the digital recording system. Analog oscilloscopes were not used to record output data for the second-generation DFP system. In this way, the second-generation DFP is a prototype of a field-ready diagnostic. The FP interference fringes recorded by one 16-channel array are shown in Fig. 2.

The key challenge for the continuation of this project is the fielding of an integrated instrument on an actual hydro experiment, and demonstration that the collected data matches the quality of a streak camera.

The next stage of the DFP system is engineering and optimization. With planned changes, the system should be more robust and easy to use, making it appropriate as a field diagnostic for hydrodynamic testing.

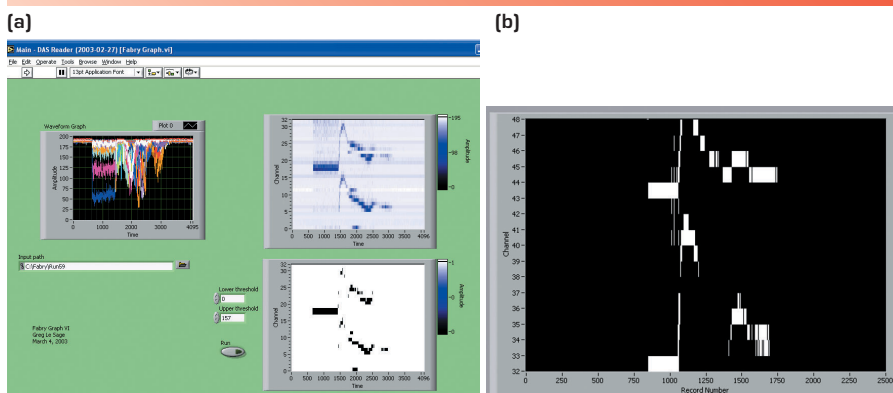


Figure 1. Fabry-Perot fringes recorded by prototype systems. (a) First prototype: analog recording of PMT. (b) Second prototype: direct digital recording.

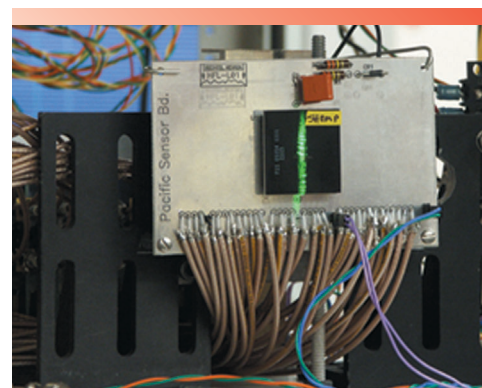
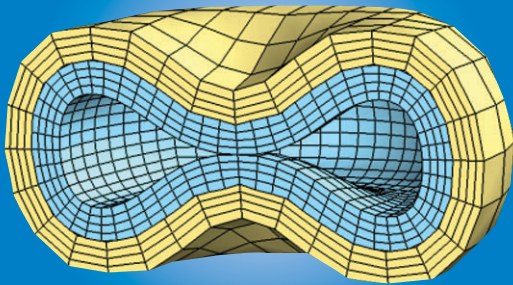


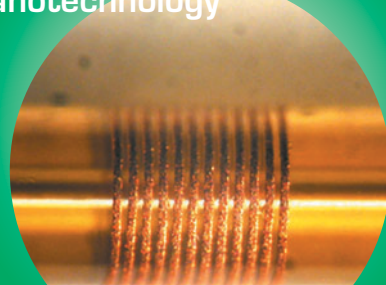
Figure 2. Laser illumination of APD.

Author Index

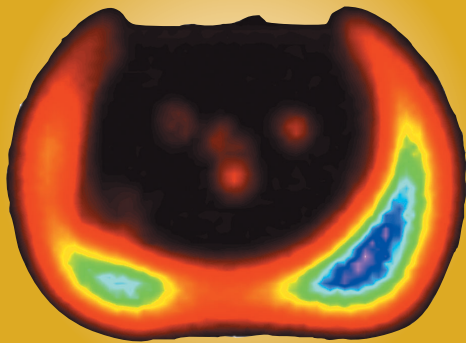
Computational Engineering



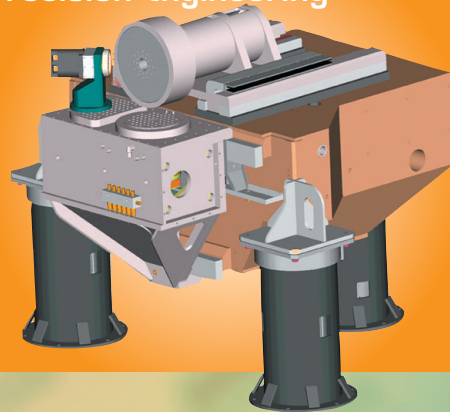
Microtechnology and Nanotechnology



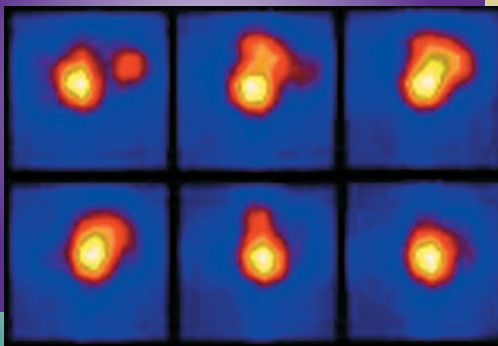
Nondestructive Characterization



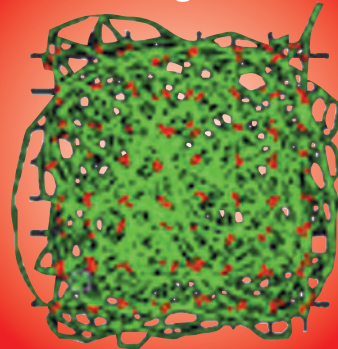
Precision Engineering



Complex Distributed Systems



Other Technologies



Author Index

Ahre, P. E.	69	Hernandez, J. E.	58
Akkerman, K. D.	21	Hibbard, R. L.	37
Bauman, B. J.	61	Hopkins, D. J.	45, 46, 48
Benson, S. E.	41	Hsieh, H.	14
Bernhardt, A. F.	31	Huber, R. D.	39
Bettencourt, K. A.	22	Hunter, S. L.	49
Bond, T. C.	21	Javedani, J. B.	6, 7
Bono, M. J.	37	Jones, E. D.	57
Brocius, W. F.	47	Kallman, J. S.	21
Brown, Jr., C. G.	7	Kane, R. J.	68, 70, 71
Burke, G. J.	6	Kent, C. A.	54
Burke, M. W.	36	Kinney, J. H.	40
Carlisle, K.	49, 50	Klingmann, J. L.	47
Carrano, C.	59	Kohlhepp, V. N.	53
Chambers, D. H.	5, 35	Kokko, E. J.	35
Champagne, N. J.	15	Kotovskiy, J.	23
Chan, C. W.	61	Krulevitch, P.	29
Chinn, D. J.	35, 38, 39	LaFortune, K. N.	61
Ciarlo, D. R.	32	Larsen, G. J.	67
Clarke, L. E.	56	Larsen, S. C.	5
Cooper, G. A.	24	Lavietes, T.	26
Crawford, J. J.	22	Lee, C. L.	4, 62
Dallum, G. E.	58	Lehman, S. K.	5
Davidson, J. C.	29	Le Sage, G. P.	72
Daykin, E. P.	72	Lin, J. I.	10
DeTeresa, S. J.	35, 67	Logan, C. M.	38
Dolan, K. W.	40	Loomis, M. D.	8
Dowla, F. U.	54, 63	Loosmore, G. A.	14
Eichholz, R.	72	Lui, K.	32
Evans, L. B.	31	Maghribi, M.	29
Fisher, K. A.	5	Malba, V.	31
Flath, L. M.	55	Martz, H. E.	35, 37
Freeman, S. D.	53	McCall, S. K.	28
Garrett, C. C.	69	McConaghy, C. F.	26
Geraghty, P.	45, 50	McElfresh, M. W.	28
Gerhard, M. A.	60	Meyer, G. A.	26
Glascoe, L. G.	14	Miles, R. R.	22
Glaser, R. E.	62	Miller, W. O.	36
Goel, S.	4	Morse, J. D.	11, 32
Groves, S. E.	28	Muyco, J. J.	24
Hale, L. C.	50	Ness, K. D.	30
Hamilton, J.	29	Ong, M. M.	7
Hanley, W. G.	62	Ortega, J. M.	9
Harvey, C. D.	31	Pao, H.	68
Haupt, D.	40	Perez, C.	72
Havstad, M. A.	11, 16	Perkins, N. C.	4

Perryman, G.	72
Petersen, H. E.	32
Pierce, E. M.	12
Pocha, M. D.	26
Portnoff, M. R.	70
Poyneer, L. A.	61
Price, D.	56
Puso, M. A.	3
Raley, N. F.	24
Romero, K.	58
Rusnak, B.	13
Salari, K.	9, 17
Schneberk, D. J.	40
Sengupta, S.	56
Sharpe, R. M.	8, 35
Silva, D. A.	59
Smith, A. M.	56
Smith, T.	40
Sopchak, D. A.	27
Speck, D. E.	12

Sperry, V. R.	24
Spiridon, A.	63
Steich, D.	6
Stewart, J. S.	56
Stolz, C. J.	39
Stowell, M. L.	15
Swierkowski, S. P.	23
Syn, C. K.	67
Thomas, G. H.	5, 36, 41
Tran, B. N.	68, 72
Vogtlin, G. E.	7
Waters, A. M.	37
Weinert, G. F.	48
Weinzapfel, C. L.	39
Weisgraber, T. H.	25
Wheeler, E. K.	30
Wolfe, J. D.	26
Wulff, T. A.	48
Zumstein, J. M.	58
Zywicz, E.	10

Manuscript Date April 2004
Distribution Category UC-42

This report has been reproduced directly from the best available copy.

Available for a processing fee to U.S. Department of Energy
and its contractors in paper from
U.S. Department of Energy
Office of Scientific and Technical Information
P.O. Box 62
Oak Ridge, TN 37831-0062
Telephone: (865) 576-8401
Facsimile: (865) 576-5728
E-mail: reports@adonis.osti.gov

Available for sale to the public from
U.S. Department of Commerce
National Technical Information Service
5285 Port Royal Road
Springfield, VA 22161
Telephone: (800) 553-6847
Facsimile: (703) 605-6900
E-mail: orders@ntis.fedworld.gov
Online ordering: <http://www.ntis.gov/products/>

Or

Lawrence Livermore National Laboratory
Technical Information Department's Digital Library
<http://www.llnl.gov/library/>

This document was prepared as an account of work sponsored by an agency of the United States Government. Neither the United States Government nor the University of California nor any of their employees, makes any warranty, express or implied, or assumes any legal liability or responsibility for the accuracy, completeness, or usefulness of any information, apparatus, product, or process disclosed, or represents that its use would not infringe privately owned rights. Reference herein to any specific commercial products, process, or service by trade name, trademark, manufacturer, or otherwise, does not necessarily constitute or imply its endorsement, recommendation, or favoring by the United States Government or the University of California. The views and opinions of authors expressed herein do not necessarily state or reflect those of the United States Government or the University of California, and shall not be used for advertising or product endorsement purposes.

This work was performed under the auspices of the U.S. Department of Energy by the University of California, Lawrence Livermore National Laboratory under Contract W-7405-Eng-48.
ENG-03-0095-AD



Lawrence Livermore National Laboratory
University of California
P.O. Box 808, L-151
Livermore, California 94551



http://www_eng.llnl.gov/